URBAN WIND ENERGY POTENTIAL IN THE NETHERLANDS - AN EXPLORATORY STUDY

Abdolrahim Rezaeiha[1], Hamid Montazeri[1,2], Bert Blocken[1,2]

[1] Building Physics and Services, Department of the Built Environment, Eindhoven University of Technology, P.O. Box 513, 5600 MB Eindhoven, The Netherlands

[2] Building Physics Section, Department of Civil Engineering, KU Leuven, Kasteelpark Arenberg 40 – Bus 2447, 3001 Leuven, Belgium

In opdracht van RVO op verzoek van de Topsector Energie, TKI Urban Energy

Projectnummer: TSE1704011

Date: 17 June 2018

SUMMARY

The integration of wind energy systems in the urban environment has often been advocated because it represents a yet unexploited potential, because wind energy would then be produced close to where it is needed and because urban wind energy is considered complementary to solar energy and both could thus be combined. The most often mentioned disadvantages are that small wind turbines are less efficient, less economically viable and that mean wind speed in the urban environment is generally lower and turbulence higher than outside the urban environment, either offshore or onshore.

A number of choices were made in this exploratory study to provide a first assessment of the potential for urban wind energy in the Netherlands. The first choice was to consider only vertical axis wind turbines (VAWTs) of the Darrieus type. The second choice was the type of integration. There are three categories of possibilities: (1) siting stand-alone wind turbines in urban locations; (2) retrofitting wind turbines onto existing buildings; and (3) full integration of wind turbines together with architectural form. The performance of category 1 systems has been reported to be very site-specific. A number of interesting category 3 systems has been contemplated but not included in the assessment in this report due to the additional construction costs involved and the limited size of the wind turbines that can be integrated in these systems. However, they deserve further research. Therefore this report focused only on Category 2, the most straightforward solution, i.e. to mount Darrieus VAWTs on the roof on masts that are high enough so that the rotors are situated above the areas of separated flow above the roofs.

For the assessment of the wind energy potential, we considered 85 Dutch cities and only buildings with a height equal to or above 35 m. The annual statistical mean wind speed distribution was obtained by Weibull distributions. Only the wind speed at roof height was used. It is a first-order approximation and of course, for actual implementation on a specific building, a more detailed wind potential assessment by CFD or by a wind tunnel study should be provided. Evidently, installations in the high wind speed area in the Netherlands will yield much higher energy output than in the medium or low wind speed area. The selected turbine was a high-performance VAWT with high power coefficients and high-efficiency (> 97%) direct-drive brushless permanent magnet generator (PMG). It was a 2-bladed turbine with diameter 1 m, height 5 m, NACA0018 blade and operating in variable speed.

12 VAWTs were installed per roof. The total number of VAWTs was 18,154, yielding a total Annual Energy Production (AEP) of about 170 GWh. The associated (safely) estimated costs, including rotor, tower, electrical components, fixation, grid connection, planning etc. were 310.24 million €, yielding a Levelized Cost of Energy (LCoE) of 90.96 €/MWh (~0.091 €/kWh). This cost is reasonable but the number of turbines is very high, requiring an excessive installation and maintenance campaign. These 18,154 small VAWTs on the roofs of high-rise buildings would yield a similar AEP as 28 large 2.5 – 3 MW onshore horizontal axis wind turbines (HAWTs) and could cover the yearly electricity demand of about 42,500 average households.

Technological developments that are needed to exploit this urban wind energy potential in the Netherlands first and foremost include the realization of highly-efficient and reliable Darrieus VAWTs in large numbers and at low costs. For slender and light-weight VAWTs as analyzed here, the horizontal loads on the building are very small compared to the overall wind loads on high-rise buildings. Noise and structural vibrations should not constitute major challenges if standard vibration dampers are installed. The realization of this full potential of urban wind energy and LCOE could take 15 years but entails considerable challenges such as a detailed aerodynamic assessment per building. This and other disadvantages such as the very large number of wind turbines needed and the relatively low AEP even when 18,154 turbines are applied in the whole country, are expected to render the realization of the full urban wind energy potential in the Netherlands insufficiently attractive. Instead, individual and project-based integration of wind energy systems in iconic building projects can be considered, given the low LCoE, however not without overcoming the challenges and problems mentioned in this report.

SAMENVATTING

De integratie van windenergiesystemen in de gebouwde omgeving kan interessant zijn omdat het gaat om een vooralsnog niet benut potentieel, omdat windenergie dan geproduceerd wordt op de plek waar deze wordt gebruikt, en omdat windenergie complementair is aan zonneënergie en beiden dus gecombineerd kunnen worden. Vaak vermelde nadelen zijn dat kleine windturbines weinig efficiënt zijn, minder economisch rendabel, en dat de gemiddelde windsnelheid in de gebouwde omgeving lager is en de turbulentie hoger dan buiten de gebouwde omgeving, zowel offshore als onshore.

In deze verkennende studie zijn een aantal keuzes gemaakt om een eerste schatting te voorzien van het potentieel voor windenergie in de gebouwde omgeving in Nederland. De eerste keuze is om enkel verticale-as-windturbines (VAWTs) te beschouwen. De tweede keuze betreft de aard van de integratie. Er zijn drie categorieën: (1) alleenstaande windturbines in de gebouwde omgeving; (2) windturbines toevoegen aan bestaande gebouwen; en (3) volledige integratie in het ontwerp van het gebouw. Het rendement van categorie 1 blijkt zeer sitespecifiek. In categorie 3 zijn er een aantal interessante systemen ontwikkeld, maar deze worden niet beschouwd in dit rapport wegens de bijkomende constructiekosten en de beperkte omvang van de windturbines die er in ondergebracht kunnen worden. Desalniettemin verdienen deze systemen verder onderzoek. Dit rapport beperkt zich tot categorie 2, met name de meest voor de hand liggende oplossing: het plaatsen van Darrieus-VAWTs op het dak bovenop masten die hoog genoeg zijn zodat de rotoren zich boven de zones van stromingsseparatie en –recirculatie op het dak bevinden.

Voor de schatting van het windenergiepotentieel worden 85 Nederlandse steden beschouwd en enkel gebouwen met een hoogte gelijk aan of hoger dan 35 m. De jaarlijkse statistiek van de gemiddelde windsnelheid volgt uit Weibullfuncties op basis van de data van de KNMI-weerstations. Enkel de windsnelheid op dakhoogte wordt beschouwd. Dit is een eerste-orde-benadering en voor een effectieve implementatie op een specifiek gebouw is uiteraard een gedetailleerde analyse nodig door een CFD- of een windtunnelonderzoek. Logischerwijze leveren installaties in het sterke windgebied in Nederland een veel hogere energieopbrengst dan die in het mid- of lage windgebied. De geselecteerde turbine is een VAWT met hoge powercoëfficiënten en hoge-efficiëntie (> 97%) direct-drive permanente magneetgenerator (PMG). Het is een 2-bladige turbine met 1 m diameter, 5 m hoogte, NACA0018-blad en deze opereert met variabele snelheid.

Per dak worden er 12 VAWTs geïnstalleerd. Het totaal aantal VAWTs bedraagt dan 18,154 en deze leveren naar schatting een totale *Annual Energy Production* (AEP) van ongeveer 170 GWh. De daarmee gepaard gaande ruime schatting van de kosten, inclusief rotoren, masten, elektrische componenten, bevestiging, connectie met het elektriciteitsnetwerk, planning enz. zijn 310 miljoen €. Dit geeft een *Levelized Cost of Energy* (LCoE) van 91 €/MWh (~0.091 €/kWh). Dit is een redelijke kost maar het aantal windturbines is erg hoog, wat een excessieve installatie- en onderhoudscampagne vereist. Ter vergelijking, deze 18,154 kleine VAWTs geven ongeveer dezelfde AEP als 28 grote 2.5 – 3 MW onshore horizontale-as-windturbines (HAWTs), genoeg voor het jaarlijkse elektriciteitsgebruik van ongeveer 42,500 reguliere huishoudens.

De technologische ontwikkelingen nodig om dit potentieel te exploiteren zijn eerst en vooral de realisatie van zeer efficiënte en betrouwbare Darrieus-VAWTs, in grote hoeveelheden en aan lage kosten. Voor de slanke en lichtgewicht turbines in deze studies, zijn de horizontale belastingen op het gebouw zeer klein vergeleken met de totale windbelasting op het gebouw. Geluid en structurele trillingen zijn geen onoverkomelijke uitdagingen mits gebruik van standaardtrillingsdempers. De realisatie van dit totale potentieel en LCOE zou 15 jaar kunnen vragen, maar vereist wel het aanpakken van aanzienlijke uitdagingen waaronder ook de gedetailleerde aerodynamische analyse van elk individueel gebouw. Deze en andere nadelen zoals het zeer grote aantal kleine turbines en de relatief lage AEP zelfs bij al die 18,154 turbines toegepast in het hele land, werken ontradend om dit totale potentieel effectief te gaan realiseren. Desalniettemin kan voor individuele projecten wel de integratie van windenergiesystemen beschouwd worden, gezien de lage LCoE, echter rekening houdend met de uitdagingen en problemen vermeld in dit rapport.

REPORT

Since 2012, the energy policy in the Netherlands has been focused on specific technologies. These include wind energy, where the focus up to now has been on offshore wind. Within RVO and TKI Urban Energy, the question has arisen to what extent Urban Wind Energy should become a topic within the Urban Energy Innovation Programme. Therefore, RVO has requested the present authors to analyze the potential for wind energy harvesting on top of high-rise buildings in urban areas. Specifically, a series of key questions was provided, each of which are answered in this report. More detailed information is provided in the appendices.

Question A: Which solutions are currently commercially available and which are in development to harvest wind energy on high-rise buildings?

Two different levels of solutions are considered: (1) solutions in terms of types of wind turbines and (2) solutions in terms of positioning around, in or on top of high-rise buildings.

Among the small wind turbines a distinction is made between horizontal-axis wind turbines (HAWTs) and vertical-axis wind turbines (VAWTs). Currently small HAWTs, backed up by decades of research on large-scale HAWTs, are the dominant type in the small wind turbine market with 74% of the total share (Fig. 1).

Figure 1. Left: Share of different wind turbine types in the world market (Small Wind World Report 2017). Middle: Horizontal axis wind turbine by Tuge Energia and vertical axis wind turbine (Darrieus type) by Windspire. Right: Vertical axis wind turbine (Savonius turbine)

However, the growing interest for VAWT optimization, which is due to their many advantages for wind energy harvesting in the urban environment, will render them a better candidate for the urban environment and could significantly increase their share in the market. The growing interest for VAWTs can be attributed to several advantages compared to HAWTs, such as (Ferreira and Schreurich 2014, Borg and Collu 2015, Rezaeiha et al. 2017a, 207b, 2018a, Chen et al. 2017):

- Omni-directional capability: no yaw system is needed. This characteristic of VAWTs is very important for the urban environment where the wind direction exhibits larger and more frequent variations.
- Low noise: due to operating at lower tip speed ratios and smaller diameters, the blade tip speed is lower, which leads to lower levels of aerodynamic noise.
- Low manufacturing cost: due to simple blade profiles with no taper and twist as well as simplicity in the control system, i.e. no pitch and yaw control system.
- Low installation and maintenance costs: due to having the generator on the ground.
- Scalability: the turbine height-to-diameter ratio can scale up with minimal effect on performance.

- Better robustness and reliability
- Very small shadow flickering
- No danger to birds due to typically low installation height
- Visually more attractive
- Multifaceted installation tower, e.g. telecom towers

Within the group of VAWTs, preference is generally given to the Darrieus-type of wind turbines as opposed to the Savonius type (Fig. 1), as the latter is generally characterized by very low power coefficients.

Research by the present authors has shown that there is currently a strong lack of economical, highly efficient and reliable VAWTs. Recent concerted efforts towards the development of a new, efficient and reliable VAWT have been performed in the framework of the European Horizon2020 ITN project AEOLUS4FUTURE (Rezaeiha et al. 2017b, c, d, 2018a, b) but more research and actual prototype development and testing is needed.

A distinction is made between three categories of possibilities for integration of wind energy systems into urban environments: (1) siting stand-alone wind turbines in urban locations; (2) retrofitting wind turbines onto existing buildings; and (3) full integration of wind turbines together with architectural form. Category 2 and 3 are often referred to as "building-integrated wind turbines". Solutions in category 1 are generally conventional HAWTs, intended to be mounted on top of masts in fairly open areas around buildings. The performance of these systems has been reported to be very site-specific (e.g. Peacock et al. 2008) and in many cases the proximity to buildings has decreased the performance (e.g. Mithraratne 2009). This category is therefore not considered further in the present report. Category 2 includes traditional or newly developed wind turbines that can be fitted onto either existing buildings or new buildings, without the need for specially modifying the building form. Category 3 on the other hand consists of modified building forms for full integration of wind turbines. This report focuses on Category 2 and 3. Specific solutions in these categories are explained further below.

1. **Wind turbines on masts on top of high-rise buildings**
   The most straightforward solution is to place wind turbines on mast on top of high-rise buildings. The masts should be high enough so that the wind turbine is situated outside the area of separated flow above the roof for all possible wind directions, i.e. in the actual amplified wind speed area that is present above the area of separated flow. If these systems are placed on the roof of buildings without special modification of the building form, they belong to Category 2 mentioned above.

2. **Roof-integrated wind turbines**
   A variety of roof-integrated systems has been devised that all belong to Category 3. These systems consist of a special roof configuration in which one or more VAWTs can be embedded. Not all of them will be mentioned here, in the interest of brevity just one example is selected, which is the Powerdak 1.0 concept developed by Bronsema (2005, 2010, 2013). The philosophy of the Powerdak 1.0 (Fig. 2) is to exploit the Venturi effect to increase the wind speed in the narrowest part of the roof where a VAWT is located. However, one should carefully balance the increase of wind speed or flow rate by the contraction on the one hand, and the increase of flow resistance by this contraction itself and by possible vertical guiding vanes (van Hooff et al. 2011, Blocken et al. 2011, van Hooff et al. 2012). A common error made in the evaluation of this type of configurations is that the ratio between the wind speed at the narrowest section of the contraction and the wind speed at the inlet of the contraction is used to calculate the wind energy potential based on meteorological data linked to the wind speed at the inlet. However, due to the large flow resistance that is induced by these roof configurations, the wind speed at the inlet of the roof will already be much lower than the meteorological wind speed at that height. This misconception can easily lead to unrealistic expectations that cannot be realized in practice. This is clearly shown in Fig. 3 that shows the amplification of wind speed in a horizontal and vertical plane through the roof construction. The amplification is defined as the ratio of the local wind speed to the wind speed at roof height without

building present. As such, the first two configurations in Fig. 3 seem to yield no increase at all in the narrowest part of the contraction, as the amplification factor is equal to one. The reason is that these roof constructions present such a large obstruction to the wind in terms of flow resistance that the wind speed at the inlet of the roof construction is reduced by up to a factor 10 or more. The subsequent real Venturi effect that only occurs in the closed channels between the inlet of the contraction and the narrowest part of the contraction does yield an increase in wind speed, but apparently just enough to compensate the earlier reduction, yielding a net zero benefit. However, the Powerdak 1.0 design without vertical guiding vanes does yield a substantial increase in wind speed, up to a factor 1.35. Note that the first two roof configurations only provide space for a single VAWT at the position of the highest amplification factor, while the configuration without vertical guiding vanes provides space for placing several VAWTs.

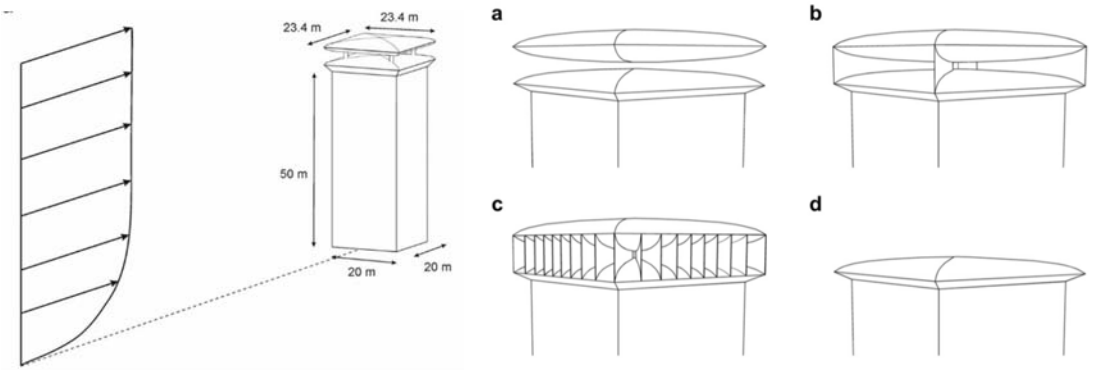

Figure 2. Analyzed configurations for roof-integrated wind turbine systems (van Hooff et al. 2011). Configuration (a) without vertical guiding vanes is the Powerdak 1.0 concept by Bronsema.

Three important disadvantages of this type of roof-integrated wind turbine systems are: (1) the added costs for the special roof construction; (2) the increased flow resistance through the roof due to the contraction itself including potential guiding vanes, which reduce the wind speed and the power output; and (3) the limited space and height to add multiple and especially higher wind turbines. For these reasons, Bronsema has abandoned the original concept of the Powerdak (Powerdak 1.0) and has moved towards the concepts of the Powerdak 2.0 and later 3.0 (Fig. 4), that include the installation of wind turbines on existing roofs, however, with rounded roof edges to avoid large areas of separated flow over the roof (Bronsema 2017). Research has shown that this concept shows a very good performance while allowing higher VAWTs to be installed (Blocken 2016c, d). The Powerdak 3.0 concept requires less materials and costs. It has not been considered in this report but it should be part of further cost-benefit analysis and can become an integral part of Urban Wind Energy solutions.

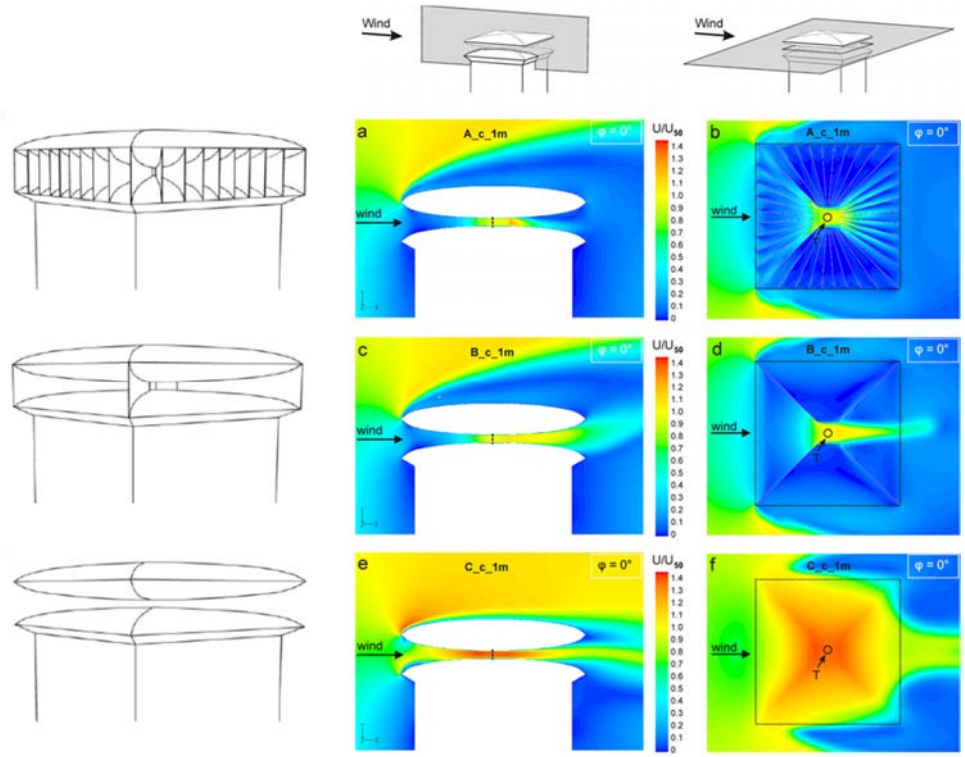

Figure 3. Wind speed amplification for different roof-integrated wind turbine configurations including the Powerdak 1.0 (van Hooff et al. 2011).

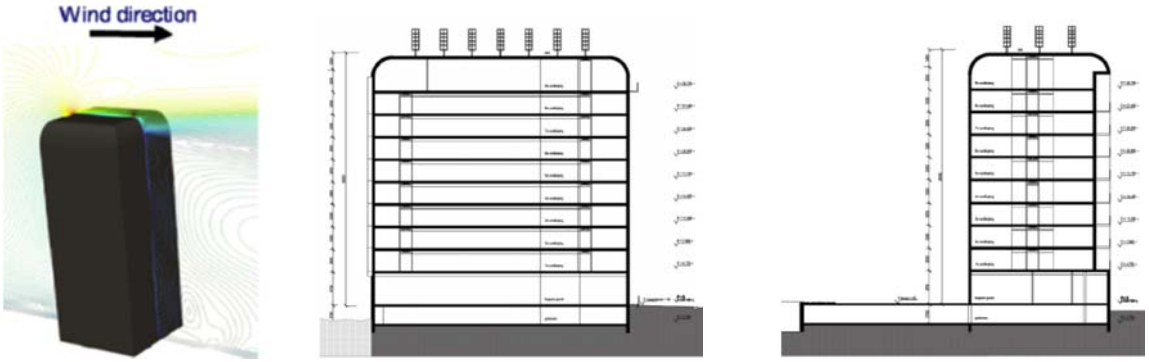

Figure 4. Left: Sketch of high-rise building with implementation of Powerdak 3.0. Middle and right: Line drawing of Breeze hotel with Powerdak 3.0 (not implemented as such in reality due to current lack of efficient and reliable VAWTs). (Blocken 2016c, Bronsema 2017)

3. **Façade-integrated wind turbines (corners)**
Façade-integrated wind turbines are inspired by the amplified wind speed that can occur around building corners. Nevertheless, when integrated in the corner itself, they can be partly situated in the areas of separated flow or the area of flow stagnation when oriented to the approaching wind. For the other wind directions, they will almost always be situated in the area of separated flow or in the building wake. In addition, often Savonius turbines are used, that are generally characterized by very low power coefficients. Because of these reasons, façade-integrated wind turbines have not been considered in this report.

Figure 5. Parking garage: Greenway Self-Park, 60 W Kinzie St, Chicago, USA (https://www.friedmanproperties.com/portfolio/greenway-self-park)

4. **Façade-integrated wind turbines (open floors or ducts through buildings)**
From the study of pedestrian-level wind (PLW) conditions around buildings, it is known that PLW speed can increase substantially in passages through buildings at ground level (Wiren 1975). This increase in wind speed results from pressure short-circuiting between the overpressure area at the windward façade and the underpressure area at the leeward façade. Similarly, through-passages can be made at larger height above the ground, where the increased wind speed can be used for wind energy harvesting (Fig. 6). Alanis Ruiz (2016) studied various relevant parameters for such an integration including building dimensions, wind direction, through-passage diameter and the curvature of the through-passage edges. Especially the latter parameter was shown to be important (Fig. 7). Similar to the Powerdak 3.0 concept, rounded edges can be used to avoid flow separation and to yield a higher and more uniform wind speed in the through-passage and this measure appears to be very beneficial and effective. A sufficient curvature can yield an amplification of mean wind speed up to a factor 1.9, which is substantial and higher as has been achieved in the Powerdak 1.0 concept. Nevertheless, the very substantial intervention required to the original building structure renders the integration of wind turbines in through-passages a less likely alternative for wide implementation. Therefore, although it could be considered for a few specific pilot projects, it has not been considered in the present report to determine the wind energy potential in the Netherlands.

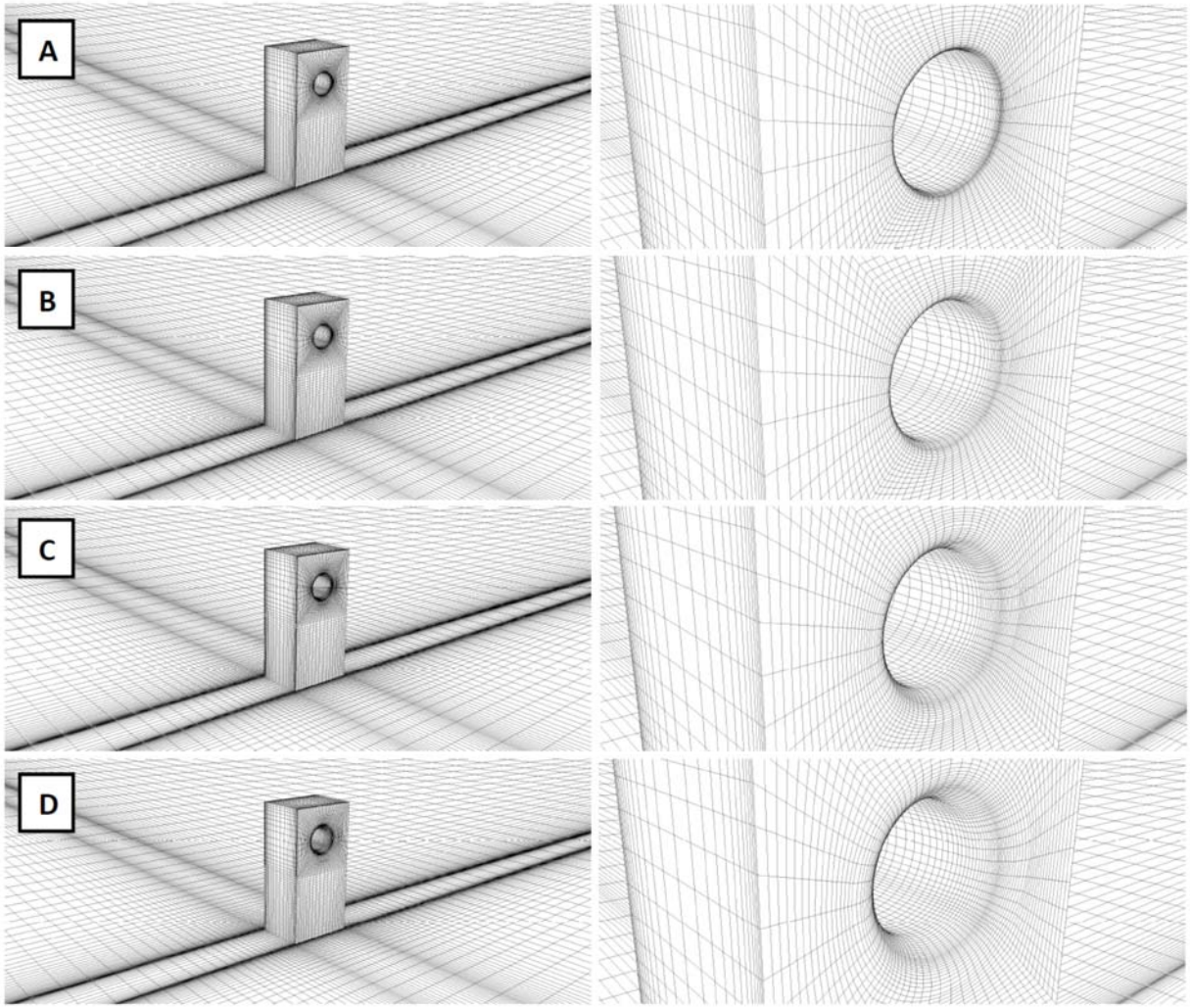

Figure 6. Computational grids for the four different fillet radius configurations: ***A)*** *Case 2-1 with fillet radius r=(1/20)*D=0.7 m;* ***B)*** *Case 2-2 with fillet radius r=(1/10)*D=1.4 m;* ***C)*** *Case 2-3 with fillet radius r=(1/5)*D=2.8 m; and* ***D)*** *Case 2-4 with fillet radius r=(1/3)*D=4.66 m (Alanis Ruiz 2016).*

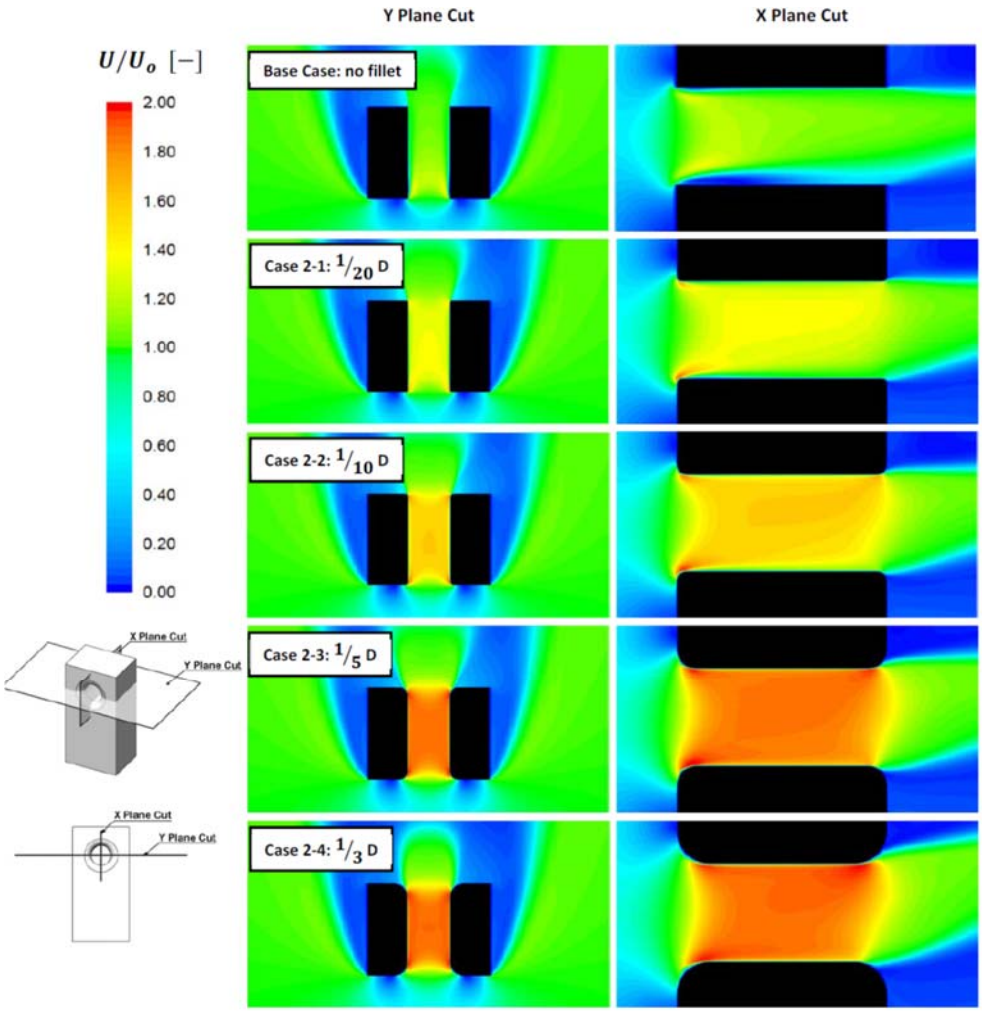

Figure 7. Contours of local wind speed amplification for building configurations with different through-passage fillet radii at 0° angle of attack (Alanis Ruiz 2016).

5. Tubular structures with integrated wind turbines

Another alternative is the integration of HAWTs in tubular structures. One of the most recent of these systems carries the name "In-Velox" (Fig. 8). Similar to the roof systems, the philosophy of these systems is to exploit the Venturi effect to increase the wind speed in the tube or channel where generally a HAWT is located in the narrowest section. However, similar to roof-integrated wind turbines, one should carefully balance the increase of wind speed or flow rate through the tube on the one hand, and the increase of flow resistance by the tubular structure itself. A common error made in the evaluation of this type of systems is that the ratio between the wind speed at the narrowest section of the tube and the wind speed at the inlet of the tube is used to calculate the wind energy potential based on meteorological data. However, due to the large flow resistance, the wind speed at the inlet of the tube will already be much lower than the meteorological wind speed. This misconception can easily lead to unrealistic expectations that cannot be realized in practice. Tubular structures with integrated turbines have not yet seen the same level of detailed and peer-reviewed scientific investigation as roof-integrated turbine systems and therefore further research is necessary to determine their real potential. Nevertheless, given the current lack of precise estimates of the real potential and the associated costs, this system is not included in this report to calculate the wind energy potential of the Netherlands.

Figure 8. Left: Invelox wind energy system in curved channel. (https://financialtribune.com/articles/energy/45861/iran-to-employ-efficient-invelox-wind-turbines). Right: Invelox wind energy system in a straight channel. (https://www.deingenieur.nl/artikel/proef-met-windtoeter)

As mentioned earlier, research by the present authors has shown that there is currently a strong lack of commercially available, economical, highly efficient and reliable VAWTs. Recent concerted efforts towards the development of a new, efficient and reliable VAWT have been performed in the framework of the European Horizon2020 ITN project AEOLUS4FUTURE (Rezaeiha et al. 2017b, c, d, 2018a, b) but more research and actual prototype development and testing is needed. The turbine characteristics resulting from this project have been used in the estimates of the urban wind energy potential in this report. Note that the Powerdak 3.0 concept has not been assumed in the present report but that it provides possibilities to increase the wind energy potential in the Netherlands further, however at the expense of increased costs for the establishment of the rounded roof edges.

The following conclusion is provided as the answer to question A: For wind energy on high-rise buildings, the most straightforward solution is to mount Darrieus-type VAWTs on the roof on masts that are high enough so that the rotors are situated above the areas of separated flow above the roofs. This will yield high masts and could be visually displeasing. Therefore, the Powerdak 3.0 concept by Bronsema can be used to reduce the areas of separated flow so the wind turbines can be mounted much lower. This yields extra costs for the rounded edges to be added to the roof but cost reduction due to lower masts. Savonius VAWTs are not interesting because of too low power coefficients. HAWTs are interesting only when the yaw feature is not needed, i.e. when implemented in façade through-passages or tubular systems. Roof-integrated systems of the type Powerdak 1.0 have been investigated in detail and abandoned by inventor Bronsema in favor of the Powerdak 3.0. Façade integrated systems (at corners) have low efficiency and should not be pursued. Façade integrated systems (through-passages) and tubular structures might yield wind speed amplifications of about a factor 2 but are cost expensive.

Question B: What are typical system efficiencies in terms of electricity production, and what are the typical costs of these systems in terms of Watt and/or LCOE (EUR/kWh)?

The full calculation is provided in the appendices. A summary is given here. First, the overall distribution of building heights across the Netherlands was provided. 85 cities were considered and only buildings with a height equal to or above 35 m were used. The annual wind speed distribution was obtained by application of Weibull distributions. The amplification of the mean wind speed above the roof of the building was not taken into account. Only the mean wind speed at roof height has been used. This is to compensate for uncertainties in the analysis as the mean wind speed amplification factor on the building roof is a local parameter depending on the building dimensions, the arrangement of the surrounding buildings, the wind direction, etc. It is a first-order approximation and of course, for actual implementation, a more detailed wind potential assessment by CFD or by a wind tunnel study should be provided. The selected turbine was a turbine that has been analyzed in detail by using high-fidelity CFD simulations extensively validated with experimental data (Rezaeiha et al. 2017a, b, c, 2018a, b). The selected turbine employs a high-efficiency (> 97%) direct-drive brushless permanent magnet generator (PMG) where due to the very limited generator

losses (< 3%), these are not considered in the power curves. The characteristics of this turbine are given in Table 1. Note that future research will probably allow designing wind turbines that perform even better but that the performance of this turbine is sufficient to provide a good indication of the wind energy potential in the Netherlands.

Table 1. Geometrical and operational characteristics of the selected turbine.

Parameter	**Value**
Type	Vertical axis wind turbine (VAWT) H-type Darrieus (lift-based)
Scale	Small-scale urban
Operation	Variable-speed
Number of blades, n	2
Diameter, d [m]	1
Height, h [m]	5
Swept area, A [m^2]	5
Turbine aspect ratio, h/d	5
Airfoil	NACA0018
Airfoil chord, c [m]	0.15
Solidity, σ	0.30
Blade aspect ratio, h/c	33.33
Shaft diameter [m]	0.04
Tip speed ratio, λ	2.5 (fixed)
Rotational speed, Ω [rad/s]	12.5 – 125
Cut-in wind speed [m/s]	2
Cut-out wind speed [m/s]	24
Noise level [dBA]	20 - 40
Lifetime	25 years
Generator type	Direct-drive brushless permenant magnet generator (PMG)
Estimated generator efficiency	> 97% (Dabiri 2011, 2014)

The performance of this turbine is shown in Fig. 9 and the wind turbine arrangement on the flat roof of the high-rise buildings in Fig. 10. Research has shown that closely packed counter-rotating VAWTs will benefit from the adjacent turbine vortex system (Dabiri 2011) and, therefore, can have a substantially higher power coefficient. Based on this, as shown in Fig. 10, an arrangement of 12 counter-rotating VAWTs installed on the roof corners are proposed per building. This is an average assumption as estimation of the optimum number of wind turbines per roof should be made by CFD or wind tunnel analysis including cost benefit analysis. Therefore, on average 12 turbines with the selected arrangement are considered to be installed per building. It is assumed that adjacent turbines do not decrease each other's performance and that each turbine is fully exposed to the wind. This positive assumption is compensated by other negative assumptions such as no amplification of the mean wind speed above the roof etc. In general, the AEP (Annual Electricity Production) is calculated based on the following additional assumptions:

- It is possible to install the small wind turbines on all the high-rise buildings in the 85 cities that are considered.
- The extracted wind profiles from 'rvo.nl' for each city, shown in the full report, are representative of the mean wind speed conditions in the whole city.
- The employed shape factor, k = 1.75, is representative of the mean wind speed distribution for the urban conditions in the studied cities.
- The turbulence impact on the turbine power curve, shown in Fig. 9, is neglected.

- The generator losses, estimated to be less than 3%, are not considered in the turbine power calculations.
- The mutual impact of the adjacent turbines on each other's performance is not considered.
- The turbine performance is assumed to remain constant during the lifetime and any performance degradation, due to the collection of dirt on the blades or other reasons, is not considered.
- The maintenance is supposed to be arranged during the time where the wind speed is below the cut-in velocity, therefore, the turbine is not operational.

The total AEP obtained by the calculations is 170.523 GWh.

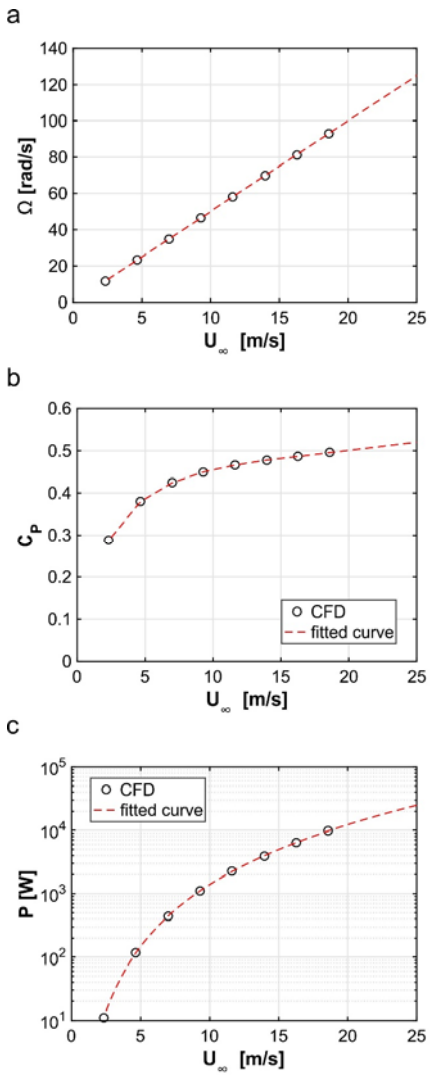

Figure 9. (a) Turbine rotational velocity, (b) power coefficient and (c) power curve (in log-scale) of the selected turbine versus wind speed.

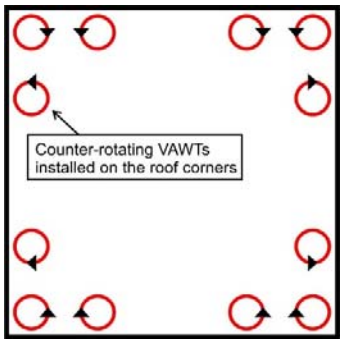

Figure 10. Schematic illustrating the selected arrangement of 12 counter-rotating vertical axis wind turbines installed near the roof corners of a building. Each pair of adjacent turbines is counter-rotating.

The installed cost of a wind power project is dominated by the upfront capital cost for the wind turbines (including foundation, towers and installation) which can account for as much as 84% of the total installed cost. The capital costs of a wind power project can be broken down into the following major categories:

- The turbine cost: Including rotor, tower and electrical components;
- Foundation/fixation: Including construction costs for site preparation and the foundations/fixations for the towers and structural damper;
- Grid connection costs: This can include transformers and sub-stations, as well as the connection to the local distribution or transmission network;
- Planning and project costs: These can represent a significant proportion of total costs; and
- Other capital costs: These can include the construction work on the building roof if necessary, control systems, etc.

The breakdown in total costs for a typical land-based wind turbine system is shown in Tables 2a and b. These values can vary depending on the location site, the project, and the wind turbines used, which by themselves can account for between 64% and 84% of total installed costs. Similarly grid connection costs can vary between 9% and 14%, construction and civil works from 4% to 16%, while other capital costs typically range between 4% and 10%.

The turbine unit price for a large order quantity of 20,000 turbines in total is estimated to be approximately 5,000 € (low-cost estimate) and 10,000 € (safe estimate). The low-cost estimate is based on the current price of similar commercial turbines in the market. For instance, the Darrieus H-type 'Royall Power' turbine with a height of 9.1 m and a diameter of 1.4 m (swept area of 12.74 m^2) at a unit order quantity is priced at 6,999 $[1]. Note that the selected turbine has smaller dimensions with a height of 5 m and a diameter of 1 m (swept area of 5 m^2) and the order quantity would be very high, i.e. 18,154.

However, this constitutes the most beneficial situation in terms of costs, where all turbines would be ordered in one large order, which is rather unlikely. Therefore, also a safe estimate is made of 10,000 € per turbine. In this safe estimate, also all other costs are doubled.

Table 2a. Low-cost estimate: Breakdown in total costs for urban wind energy with characteristics discussed in Sections 14-16 in the appendices.

Upfront capital cost	Turbine	Wind turbine (rotor, tower and generator)	90.78 million € (18,156 turbines with a unit price of 5000 €)	67.3%

[1] http://www.shoproyall.com/750w-Wind-Turbine-System_p_331.html

	Balance of systems	Electrical infrastructure	13.89 million €	10.3%
		Assembly and installation	4.04 million €	3.0%
		Site access and staging	4.31 million €	3.2%
		Foundation	5.53 million €	4.1%
		Engineering management	1.75 million €	1.3%
		Development	1.48 million €	1.1%
	Financial	Construction finance	4.99 million €	3.7%
		Contingency	8.09 million €	6.0%
	SUM		134.89 million €	100%
Lifetime O&M costs			20.23 million €	15% of upfront capital cost
Total project cost			155.12 million €	

Table 2b. Safe estimate: Breakdown in total costs for urban wind energy with characteristics discussed in Sections 14-16 in the appendices.

Upfront capital cost	Turbine	Wind turbine (rotor, tower and generator)	181.56 million € (18,156 turbines with a unit price of 10,000 €)	67.3%
	Balance of systems	Electrical infrastructure	27.78 million €	10.3%
		Assembly and installation	8.08 million €	3.0%
		Site access and staging	8.62 million €	3.2%
		Foundation	11.06 million €	4.1%
		Engineering management	3.50 million €	1.3%
		Development	2.96 million €	1.1%
	Financial	Construction finance	9.98 million €	3.7%
		Contingency	16.18 million €	6.0%
	SUM		269.78 million €	100%
Lifetime O&M costs			40.46 million €	15% of upfront capital cost
Total project cost			310.24 million €	

LCOE, or levelized cost of energy, see equation below, is a term which describes the cost of the power produced over a period of time, typically the warrantied life of the system. The calculations presented here does not take into account any tax benefit, discounted feed-in tariff or interest rate. To further dig into the details, a dedicated extensive cost analysis is required. The values are presented in Tables 3a and 3b.

$$LCOE = \frac{Lifetime\ cost\ of\ the\ project}{Lifetime\ energy\ production}$$

Table 3a. Economically beneficial estimate. Details of the levelized cost of energy.

Turbine lifetime	**25 years**
Lifetime energy production	**4263.075 GWh (25 × 170.523 GWh)**
Safety factor	**1.25**
Lifetime cost of the project	**1.25 × 155.12 million € = 193.9 million €**
Levelized cost of energy (LCOE)	**45.48 €/MWh (~ 0.045 €/kWh)**

Table 3b. Safe estimate. Details of the levelized cost of energy.

Turbine lifetime	**25 years**
Lifetime energy production	**4263.075 GWh (25 × 170.523 GWh)**
Safety factor	**1.25**
Lifetime cost of the project	**1.25 × 310.24 million € = 387.8 million €**
Levelized cost of energy (LCOE)	**90.96 €/MWh (~ 0.091 €/kWh)**

Evidently, several assumptions have been made in this calculation, both positive and negative, which should provide a reasonable first-order approximation of LCOE. Before actual implementation, a detailed AEP and cost analysis should be performed for every building where wind turbines will be installed.

Question C: Which technological developments are needed to exploit these systems optimally in the Netherlands? Indicate what modifications are necessary to existing buildings to achieve a solution of sufficient efficiency and without negative effects on buildings and inhabitants/users.
First and foremost, technological developments should focus on the realization of economical, highly-efficient and reliable Darrieus VAWTs based on high-fidelity CFD simulations, wind-tunnel tests and optimization algorithms. This especially includes the proper matching of rotor and generator characteristics aligned with the local wind statistics. These turbines could be installed on masts on the roof of buildings. The masts should be high enough so that the rotors are situated outside the areas of separated flow for all wind directions. However, this might become visually less attractive. Therefore, further analysis of the Powerdak 3.0 concept by Bronsema is suggested, to arrive at an economical and efficient "curvature" of the roof edges as to avoid massive flow separation by which the rotors can be installed much lower. Because the wind turbines selected are slender, light-weight (175 – 225 kg per wind turbine) and only 12 per roof are provided, based on discussion with noise and vibration specialists, it is assumed that noise and structural vibrations do not constitute major challenges if standard vibration dampers are installed. However noise and vibrations should be an integral part of future research projects. The noise level of the selected turbine, within the operational range of wind speed, is predicted to be 20 - 40 dBA. The prediction is based on the actual values of the available commercial Darrieus H-type VAWTs described in Section 8 of the appendices. The most important issues for structural vibrations are listed in Section 17.2 in the appendices.

Question D: What boundary conditions concerning building technology and building use should be taken into account, considering for example loads, vibrations and sound?
These boundary conditions can be quite complicated and challenging when considering wind turbines integrated in special roof constructions, in ducts in facades, or in tubular systems on roofs. However, for VAWTs installed on roofs, the turbines suggested are slender and light-weight. The horizontal load (thrust force) by a single wind turbine on the roof is estimated to be 24.5 N at 4 m/s and 882 N at 24 m/s. These

loads are minor loads compared to the overall wind loads on high-rise buildings. Similar estimates should be made for the optimal configurations of the Powerdak 3.0 construction. For vibrations and sound, see answer to question C.

Question E: What is the potential of urban wind energy systems on high-rise buildings in the Netherlands in the time frame of 10 – 15 years, and what are the feasible costs in terms of investments per Watt and/or LCOE (Eur/kWh)? What are the most important boundary conditions to optimally exploit this potential?
Only considering high-rise buildings and the standard option of wind turbines on top of masts on the roofs of these buildings, the potential in annual harvested wind energy is about 170 GWh. The LCOE at the low-cost option is 0.045 €/kWh while it is 0.091 €/kWh for the safe estimate. The expectation of the authors is that the full potential outlined above can be realized within 15 years, on condition that first funding is provided to a few excellent research consortia to deal with the above-mentioned challenges (5 years including prototype testing), after which one should proceed with detailed wind potential assessment for the existing building stock including newly planned high-rise buildings, cost assessment and manufacturing. The most important boundary conditions are establishing excellent research consortia with strong and complementary partners within the Netherlands and beyond, the realization of an economical, efficient and reliable Darrieus VAWT, the aerodynamically and economically optimal design of the Powerdak 3.0, establishing construction consortia, establishing a funding structure for manufacturing/construction and the realization of a dedicated maintenance program.

Question F: In what aspects do the Dutch organizations have a unique position in this area? Give an indication where unique knowledge is situated.
As a very knowledge-intensive country in general and with regards to urban aerodynamics and wind energy in particular, the Netherlands have a unique position towards the successful implementation of wind energy in the urban environment. The following universities and university research groups have specific expertise in wind energy. Note that this is a non-exhaustive list of active groups that is provided below in alphabetical order of institute name:

- Delft University of Technology, Department of Aerospace Engineering, Section Wind Energy (G.J.W. van Bussel e.a.)
- Delft University of Technology, Wind Energy Institute (DUWIND)
- ECN part of TNO (contact W. Boogaard)
- Eindhoven University of Technology, Department of the Built Environment (B. Blocken, M. Hornikx, e.a.)
- Eindhoven University of Technology, Department of Electrical Engineering (J.G. Slootweg e.a.)
- Eindhoven University of Technology, Department of Mathematics and Computer Science (B. Koren e.a.)
- Eindhoven University of Technology, Equipment Prototype Center (E.C.A. Dekkers e.a.)
- University of Twente, Engineering Technology (R. Akkerman, H.W.M. Hoeijmakers e.a.)

Urban wind energy assessment: van Bussel, Blocken e.a.
Aerodynamic analysis of rotor designs: van Bussel, Blocken e.a.
Integration in electrical grid: Slootweg e.a.
Prototype development: Dekkers e.a.
Wind turbine interaction: Koren e.a.
Noise and vibration: Hornikx e.a.
Economical analysis: Boogaard e.a.

In addition, a wide range of manufacturing and consultancy companies with specific expertise in wind turbines and/or components for wind turbines exist. However, prior to setting up any project, care must be

taken to discriminate between those companies with actual strong expertise and others with less or no relevant expertise. Extreme care should be applied in building consortia with partners that have excellent expertise and past performance in all relevant subfields of (urban) wind energy realization.

Further opportunities

There are more opportunities than considered in this report alone. This report only considers locations on buildings. Other options however are integration or mounting on bridges, promenades, over rivers, on remote sensing masts, telecom base stations, motorways, railways, etc.

APPENDIX

1 Definition of small wind turbine (SWT):

The size of the wind turbines is typically defined based on the rated capacity in kW. For small wind turbines, different definitions are available based on the country and the organization. Table 1 shows an overview of different definitions for small wind turbines.

Table 1. Different definitions for small wind turbines.

	Department/ Association	Turbine Classification	Rated Capacity in kW	Additional Remarks
International	International Electrotechnical Commission	Small Wind Turbines	≤ 50	IEC 61400-2 defines SWTs as having a rotor swept area of less than 200 m2, rated power of approximately 50 kW, voltage below 1000 V AC or 1500 V DC
Canada	Natural Resources Canada (NRCan) Canadian Wind Energy Association (CanWEA)	Mini Wind Turbine	0.3 – 1.0	Adopted in the Survey of the Small Wind by Marbek Resource Consultants
		Small Wind Turbine	1 - 30	
China	Renewable Energy & Energy Efficiency Partnership (REEEP)	Small Wind Turbine	< 75	Adopted in the recent National Policy, Strategy and Roadmap Study for China Small Wind Power Industry Development
Germany	Bundesverband WindEnergie (BWE)	Small Wind Turbine	< 100	Adopted in the recent BWE-Marktübersicht spezial – Kleinwindanlagen
UK	RenewableUK	Micro wind Turbine	0 – 1.5	0,5 - 5 m Height / Up to 1000 kWh Annual Energy Production
		Small wind Turbine	1.5 – 15	2 - 50 m Height / Up to 50,000 kWh Annual Energy Production

		Small-medium Wind Turbine	15 -100	50 - 250 m Height / Up to 200,000 kWh Annual Production
	Microgeneration Certification Scheme (MCS)			Only turbines smaller than 50 kW qualify for the MCS feed-in tariff programme in UK
USA	American Wind Energy Association (AWEA)	Small Wind Turbine	< 100	Adopted in the most recent AWEA Small Wind Report 2010 and the AWEA Small Wind Turbine Global Market Study

2 Growth in the installed small wind turbines:

The prediction of the world market from 2009 to 2020 for the installed capacity of small wind turbines is shown in Fig. 1 (Small Wind World Report 2017). The wind energy capacity factor is the average power generated, divided by the rated peak power. Let's take a 5 MW wind turbine. If it produces power at an average of two MW, then its capacity factor is 40% (2÷5 = 0.40, i.e. 40%). The worldwide growth for the installed small wind turbines is shown in Fig. 2.

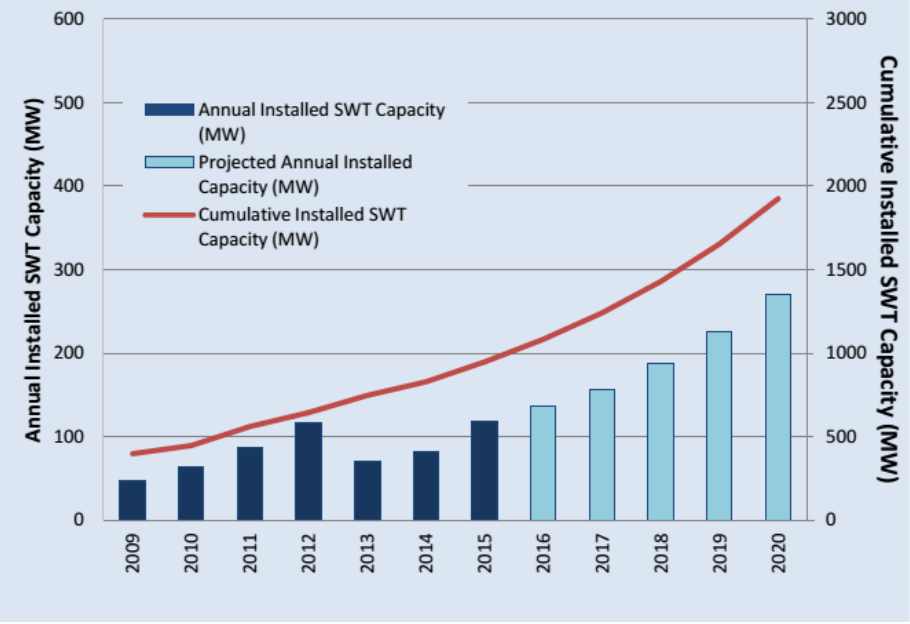

Figure 1. World market forecast from 2009 to 2020 for the installed capacity of small wind turbines [1].

Figure 2. Growth of the installed small wind turbines worldwide (Small Wind World Report 2017).

3 Share of small wind turbine market by country:

The total cumulative number of units and capacity of the installed small wind turbines based on the country is shown in Fig. 3 and 4, respectively. Share of the countries in the total installed small wind turbines is shown in Fig. 5.

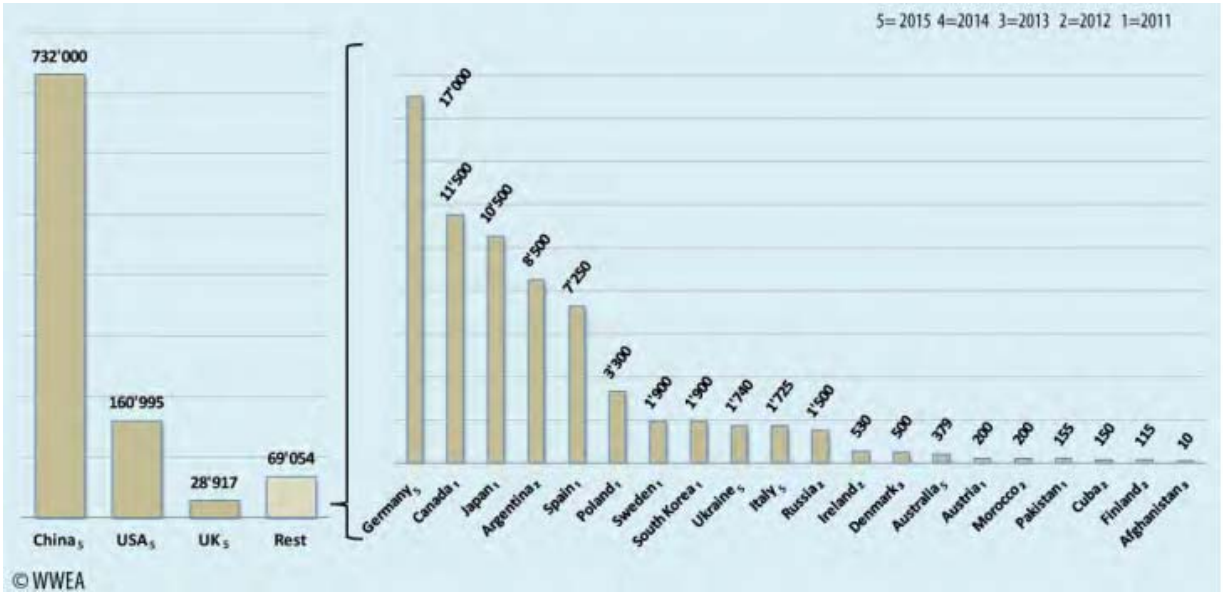

Figure 3. Total cumulative installed small wind turbines by country (Small Wind World Report 2017).

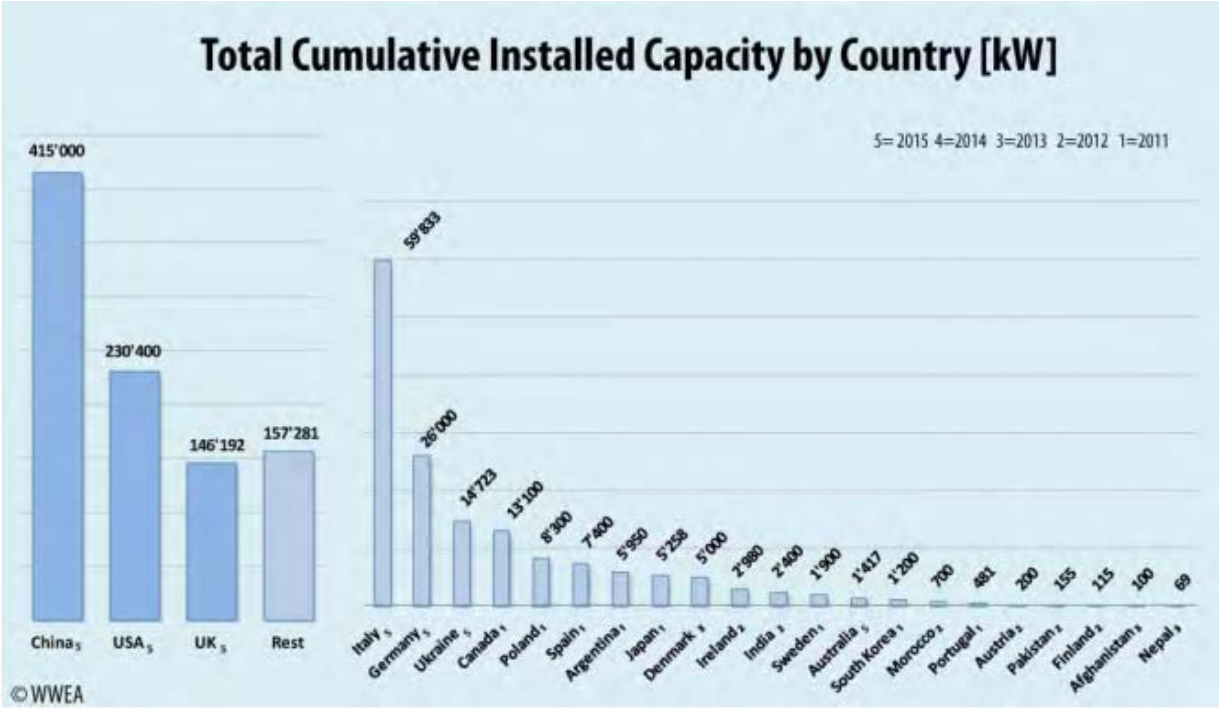

Figure 4. Total cumulative installed capacity of small wind turbines by country (Small Wind World Report 2017).

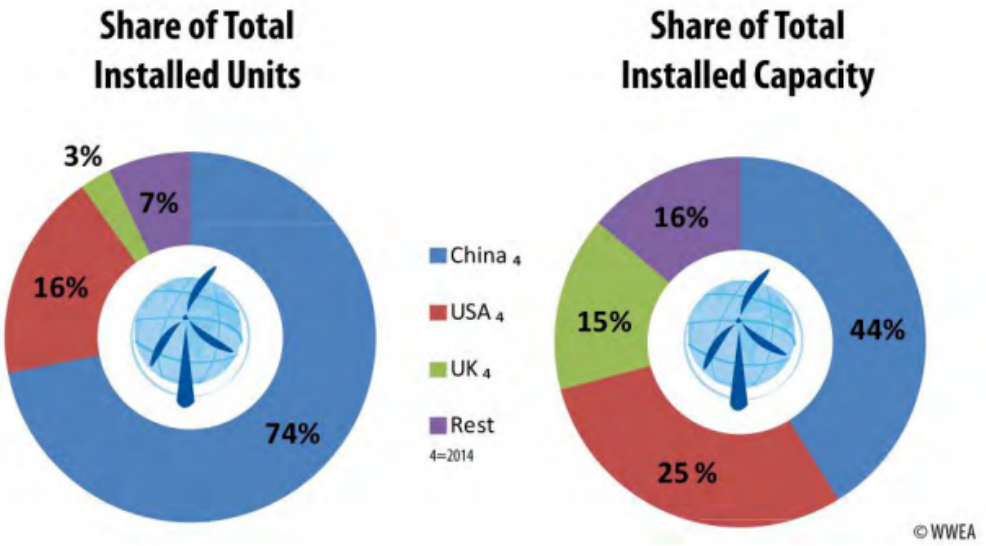

Figure 5. Share of the installed small wind turbines by country (Small Wind World Report 2017).

4 Small wind turbine applications:

The common applications for small wind turbines, based on the small wind world report (2017), are listed below:

- Residential: roof-top, stand-alone, pastures, farms and remote villages, on-grid and off-grid solutions
- Commercial and industrial: roof-top, stand-alone, e.g. parking place and lighting, fishery and recreational boats, portable systems for leisure, hybrid systems, pumping, desalination and purification systems, on-grid and off-grid solutions
- Regional: urbanity, streets, bridges, promenades, rivers, on-grid and off-grid solutions
- National: remote sensing masts, telecom base stations, motorways, railways, marine turbine system, tidal power stations, rivers, regional concepts to save grid expansion, on-grid and off-grid solutions

5 Share of different types of wind turbines:

Wind energy is a very promising renewable energy resource towards abandoning fossil fuels. Recently, while the upscaling of horizontal axis wind turbines (HAWTs) and the consequent fatigue problems are hot research topics (Leishman 2002, Islam et al. 2013, Rezaeiha et al. 2017b), vertical axis wind turbines (VAWTs) have received growing interest for off-shore applications (Borg et al. 2014, Paulsen et al. 2014, Bedon et al. 2017) and in the built environment where they have the potential to be installed on the roof, in the façade or between the buildings (Aslam Bhutta et al. 2012, Toja-Silva et al. 2013, Tummala et la. 2016, Yang et al. 2016, Rezaeiha et al. 2017b). Wind turbines can also be integrated in ventilation ducts (Park et al. 2016) and wind catchers (Rezaeian et al. 2017). Currently small HAWTs, backed up with decades of research on large-scale HAWTs, are the dominant type in the small wind turbine market with 74% of the total share (Figure 6). However, the growing interest for VAWT optimization, which is due to their many advantages for wind energy harvesting in the urban environment, would soon present them as an ideal candidate for the urban environment and could significantly increase their share in the market. The growing interest for VAWTs can be attributed to several advantages compared with HAWTs, such as (Ferreira and Schreurich 2014, Borg and Collu 2015, Rezaeiha et al. 2017a, 207b, 2018a, Chen et al. 2017):

- Omni-directional capability: no yaw system is needed. This characteristic of VAWT is very important for the urban environment where the wind direction frequently changes.
- Low noise: due to operating at lower tip speed ratios and smaller diameters, the blade tip speed is lower, which leads to lower levels of aerodynamic noise.
- Low manufacturing cost: due to simple blade profiles with no taper and twist as well as simplicity in the control system, i.e. no pitch and yaw control system.
- Low installation and maintenance costs: due to having the generator on the ground.
- Scalability: the turbine height-to-diameter ratio can scale up with minimal effect on performance
- Robustness and reliability
- Very small shadow flickering
- No danger to birds due to typically low installation height
- Visually attractive
- Multifaceted installation tower, e.g. telecom towers

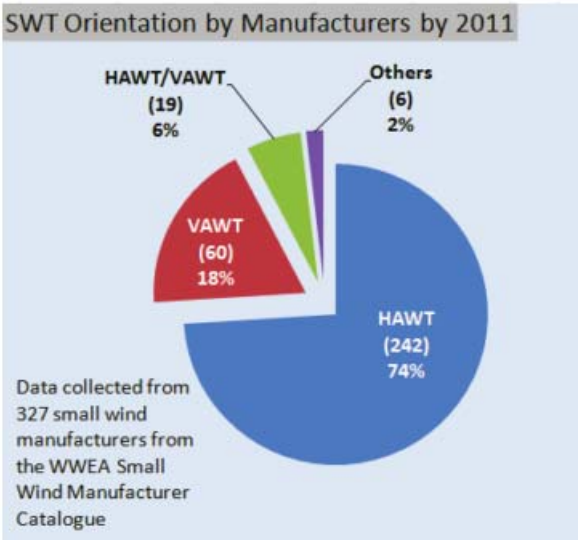

Figure 6. Share of different small wind turbine types in the world market (Small Wind World Report 2017).

6 Commercial small HAWTs:

In this section, an overview of commercial small HAWTs with maximum capacity of 10 kW, which is the range considered to be suitable for urban applications, is presented.

6.1 Bergey Windpower:

- Country: USA
- Website: www.bergey.com
- Operating data:
  - Rated power: 1.0-10.0 kW
  - Cut-in wind speed: 2.5 m/s
  - Rated wind speed: 11 m/s
  - Cut-out wind speed: None
  - Survival wind speed: 54 m/s
  - Rated noise level: N/A
- Rotor
  - Type: 3-bladed upwind
  - Pitch-controlled: No
  - Rotor diameter: 2.5-7.0 m
  - Area: 4.9-38.5 m²
  - Generator: Permanent Magnet Generator (PMG)
  - Direct drive: Yes
- Tower
  - Type: Jacket
  - Height including rotor: N/A

6.2 ZKEnergy Technology:

- Country: China
- Website: http://www.zkenergy.com
- Operating data:
  - Rated power: 0.1-5.0 kW
  - Cut-in wind speed: 3 m/s
  - Rated wind speed: 8-10 m/s
  - Cut-out wind speed: 14-18 m/s
  - Survival wind speed: 25-50 m/s
  - Rated noise level: ≤ 65 dB
- Rotor
  - Type: 3-bladed upwind
  - Pitch-controlled: No
  - Rotor diameter: 1.4-5.5 m
  - Area: 1.5-23.8 m²
  - Generator: Permanent Magnet Generator (PMG)
  - Direct drive: Yes
- Tower
  - Type: Monopile
  - Height including rotor: N/A

6.3 Zhejiang Huaying Wind:

- Country: China
- Website: http://www.huayingwindpower.com
- Operating data:
  - Rated power: 0.3-5.0 kW
  - Cut-in wind speed: 3 m/s
  - Rated wind speed: 8-10 m/s
  - Cut-out wind speed: 25 m/s
  - Survival wind speed: 40-50 m/s
  - Rated noise level: N/A
- Rotor
  - Type: 3-bladed upwind
  - Pitch-controlled: No
  - Rotor diameter: 2.2-5.0 m
  - Area: 3.8-19.6 m²
  - Generator: Permanent Magnet Generator (PMG)
  - Direct drive: Yes
- Tower
  - Type: Monopile
  - Height including rotor: 6-9 m

6.4 Gresa Group:

- Country: Ukraine
- Website: http://www.ggc.com.ua
- Operating data:
  - Rated power: 0.8-4.0 kW
  - Cut-in wind speed: 2.5 m/s
  - Rated wind speed: 8 m/s
  - Cut-out wind speed: N/A
  - Survival wind speed: 50 m/s
  - Rated noise level: N/A
- Rotor
  - Type: 3-bladed upwind
  - Pitch-controlled: No

    - Rotor diameter: 3.1-6.7 m
    - Area: 7.5-35.2 m²
    - Generator: Permanent Magnet Generator (PMG)
    - Direct drive: Yes
- Tower
    - Type: Jacket
    - Height excluding rotor: 17-27 m

6.5 Tuge Energia:

- Country: Estonia
- Website: http://www.tuge.ee
- Operating data:
    - Rated power: 2-10 kW
    - Cut-in wind speed: N/A
    - Rated wind speed: 11 m/s
    - Cut-out wind speed: 16-25 m/s
    - Survival wind speed: N/A
    - Rated noise level: < 45dB
- Rotor
    - Type: 3-bladed upwind
    - Pitch-controlled: No
    - Rotor diameter: 4-10.2 m
    - Area: 12.6-81.7 m²
    - Generator: Permanent Magnet Generator (PMG)
    - Direct drive: Yes
- Tower
    - Type: Monopile
    - Height excluding rotor: 10-22 m

6.6 Superwind:

- Country: Germany
- Website: http://www.superwind.com
- Operating data:
  - Rated power: 0.35-1.25 kW
  - Cut-in wind speed: 3.5 m/s
  - Rated wind speed: 11.5-12.5 m/s
  - Cut-out wind speed: N/A
  - Survival wind speed: N/A
  - Rated noise level: N/A
- Rotor
  - Type: 3-bladed upwind
  - Pitch-controlled: Only for 1.25 kW model
  - Rotor diameter: 1.2-2.4 m
  - Area: 1.2-4.5 m²
  - Generator: Permanent Magnet Generator (PMG)
  - Direct drive: Yes
- Tower
  - Type: Monopile
  - Height including rotor: N/A

6.7 Kingspan Wind:

- Country: UK
- Website: http://www.kingspanwind.com
- Operating data:
  - Rated power: 2.5-6 kW
  - Cut-in wind speed: 2.5 m/s
  - Rated wind speed: N/A
  - Cut-out wind speed: None
  - Survival wind speed: N/W
  - Rated noise level: N/A
- Rotor
  - Type: 3-bladed downwind
  - Pitch-controlled: No
  - Rotor diameter: 3.9-5.6 m
  - Area: 11.9-24.6 m²
  - Generator: Permanent Magnet Generator (PMG)
  - Direct drive: Yes
- Tower
  - Type: Monopile
  - Height including rotor: 4-20 m

6.8 HY Energy:

- Country: China
- Website: http://www.hyenergy.com.cn
- Operating data:
  - Rated power: 0.4-3.0 kW
  - Cut-in wind speed: 2.5 m/s
  - Rated wind speed: 12 m/s
  - Cut-out wind speed: N/A
  - Survival wind speed: 50 m/s
  - Rated noise level: N/A
- Rotor
  - Type: 5-bladed upwind
  - Pitch-controlled: No
  - Rotor diameter: 1.55-3.0 m
  - Area: 1.9-7.1 m²
  - Generator: Permanent Magnet Generator (PMG)
  - Direct drive: Yes
- Tower
  - Type: Monopile
  - Height including rotor: N/A

6.9 Ghrepower:

- Country: Multi-national
- Website: http://www.ghrepower.com
- Operating data:
  - Rated power: 5.0-10.0 kW
  - Cut-in wind speed: 3 m/s
  - Rated wind speed: 10 m/s
  - Cut-out wind speed: 25 m/s
  - Survival wind speed: 59 m/s
  - Rated noise level: < 60 dBA
- Rotor
  - Type: 3-bladed upwind
  - Pitch-controlled: No
  - Rotor diameter: 5-7.8 m
  - Area: 19.6-47.8 m²
  - Generator: Permanent Magnet Generator (PMG)
  - Direct drive: Yes
- Tower
  - Type: Monopile
  - Height including rotor: 9-14 m

7 Commercial small Darrieus-type (lift-based) VAWTs:

In this section, an overview of commercial small Darrieus-type (lift-based) VAWTs with maximum capacity of 10 kW, which is the range considered suitable for the urban applications, is presented.

7.1 Envergate:

- Country: Switzerland
- Website: www.envergate.com

7.1.1 QUINTA20

- Operating data:
  - Installed capacity: 20 kVA (12 kW)
  - Cut-in wind speed: 2.5 m/s
  - Cut-out wind speed: 22 m/s
  - Noise emission in normal operation: 38 - 43 dB
  - CE / certification: according to IEC 61400-2:2006 / MCS (in progress)
- Rotor
  - Rotor height: 6 m
  - Rotor diameter: 5 m
  - Area: 30 m²
  - Blade material: 100% CFK
  - Pitch control: Electronically regulated
  - Generator: Permanent Magnet Generator (PMG), 20 kVA
- Tower
  - Type: Steel (corrosion protected), concrete
  - Height of standard tower / including rotor: 15 m / 19.5 m
- Foundation
  - Surface area: 4.7 m x 4.7 m x 1.1 m
  - Pictures of roof-mounted and telecom-mounted foundations

7.1.2 QUINTA99

- Operating data:
  - Installed capacity: 99 kVA (60 kW)
  - Cut-in wind speed: 3.0 m/s
  - Cut-out wind speed: 22 m/s
  - Noise emission in normal operation: 38 - 43 dB
  - CE / certification: according to IEC 61400-2:2006
- Rotor
  - Rotor height: 12 m
  - Rotor diameter: 10 m
  - Area: 120 m²
  - Blade material: 100% Carbon fiber
  - Pitch control: Electronically regulated
  - Generator: Permanent Magnet Generator (PMG), 99 kVA
- Tower
  - Type: Steel (corrosion protected), concrete
  - Height of standard tower / including rotor: 24 m / 33 m
- Foundation
  - Surface area: 7.5 m x 7.5 m x 2.0 m

7.2 Royall power:

- Country: USA
- Website: http://www.royallpower.com/

7.2.1 Royall 750 W

- Rated maximum output: 750 W
- Annual output: 2650 kWh @ average 5.6 m/s wind speed
- Cut-in wind speed: 3.6 m/s
- Cut-out wind speed: 15.6 m/s
- Survival wind speed: 49 m/s
- Blades: 3 blades in one tier total 3 blades
- Rotor diameter: 1.37 m
- Height: 9.1 m
- Weight: 351 kg
- Construction: All metal, special powder coatings
- Price: 6,995.00 $

7.2.2 Royall 2 kW

- Rated maximum output: 2000 watts
- Annual output: 4250 kWh @ average 5.6 m/s wind speed
- Cut-in wind speed: 3.6 m/s
- Cut-out wind speed: 18.7 m/s
- Survival wind speed: 49 m/s
- Blades: 3 blades in one tier total 3 blades
- Rotor diameter: 1.58 m
- Height: 9.1 m
- Weight: 442 kg
- Construction: all metal, special powder coatings
- Price: 15,900.00 $
- Can be installed both on-grid and off-grid

7.2.3 Royall 3kW

- Rated maximum output: 3000 watts
- Annual output: 7460 kWh @ average 5.6 m/s wind speed
- Cut-in wind speed: 4.47 m/s
- Cut-out wind speed: 18.7 m/s

- Survival wind speed: 49 m/s
- Blades: 3 blades in one tier total 3 blades
- Rotor diameter: 1.67 m
- Height: 9.1 m
- Weight: 567 kg
- Construction: all metal, special powder coatings
- Price: 25,499.00 $
- Can be installed both on-grid and off-grid

7.2.4 Royall 5kW

- Rated maximum output: 5100 watts
- Annual output: 9400 kWh @ average 5.6 m/s wind speed
- Cut-in wind speed: 4.47 m/s
- Cut-out wind speed: 15.6 m/s
- Survival wind speed: 49 m/s
- Blades: 3 blades in one tier total 3 blades
- Rotor diameter: 2.14 m
- Height: 9.75 m
- Weight: 658 kg
- Construction: all metal, special powder coatings
- Price: 32,899.00 $
- Can be installed both on-grid and off-grid

7.3 Quiet revolution - QR6:

- Country: UK
- Website: http://www.quietrevolution.com
- Operating data:
    - Rated power: 7.5 kW
    - Cut-in wind speed: 4.5 m/s
    - Cut-out wind speed: 25 m/s
    - Survival wind speed: 52.5 m/s
    - Rotor speed: 100 – 260 RPM
    - Minimum recommended annual mean wind speed: 5.0 m/s
- Rotor
    - Rotor height: 5.5 m
    - Rotor diameter: 3.1 m
    - Area: 16 m²
    - Blade material: Carbon fiber
    - Generator: Permanent Magnet Generator (PMG)
- Tower
    - Type: galvanised steel
    - Roof-mounted: 6 m
    - Ground-mounted: 15 and 18 m

7.4 V-AIR wind technologies:

- Country: USA
- Website: www.ugei.com and http://visionairwind.com

7.4.1 Vision Air 3

- Operating data:
  - Rated power: 1.0 kW
  - Cut-in wind speed: 3.5 m/s
  - Rated wind speed: 11 m/s
  - Max. power wind speed: 14 m/s
  - Cut-out wind speed: 20 m/s
  - Survival wind speed: 50 m/s
  - Rated RPM: 200
  - Rated noise level: 41 dBA
  - Certification: CE / ISO 9001 / UL 1004 / CSA C22.2
- Rotor
  - Rotor height: 3.2 m
  - Rotor diameter: 1.8 m
  - Area: 5.76 m²
  - Blade material: Fiber glass
  - Generator: Permanent Magnet Generator (PMG)
  - Weight: 274 kg

7.4.2 Vision Air 5

- Operating data:
  - Rated power: 2.5 kW
  - Cut-in wind speed: 3.5 m/s
  - Rated wind speed: 11 m/s
  - Max. power wind speed: 14 m/s

    - Cut-out wind speed: 20 m/s
    - Survival wind speed: 50 m/s
    - Rated RPM: 130
    - Rated noise level: 38 dBA
    - Certification: CE / ISO 9001 / UL 1004 / CSA C22.2 / IEC 61400-11 & 12
- Rotor
    - Rotor height:: 5.2 m
    - Rotor diameter: 3.2 m
    - Area: 16.6 m²
    - Blade material: Fiber glass
    - Generator: Permanent Magnet Generator (PMG)
    - Weight: 756 kg

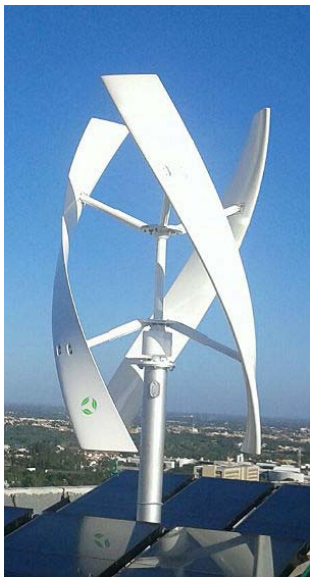

7.5 Angel wind energy - Windspire:

- Country: USA
- Website: www.angelwindenergy.com/windspireoverview.html
- Operating data:
    - Rated power: 1.2 kW
    - Cut-in wind speed: 4.0 m/s
    - Rated wind speed: 11.2 m/s
    - Max. power wind speed: 14 m/s
    - Survival wind speed: 45 m/s
    - Max RPM: 500
    - Peak tip speed ratio: 2.8
    - Rated noise level: 20 dBA at 12 m/s
- Rotor
    - Rotor height: 6.1 m
    - Rotor diameter: 1.2 m
    - Area: 7.43 m²
    - Blade material: aircraft grade extruded aluminum
    - Generator: Permanent Magnet Generator (PMG)

    - Weight: 273 kg
- Tower
    - Type: recycled high grade steel with corrosion-resistant industrial grade coating
    - Height including rotor: 9.1 m
- Foundation
    - Material: poured concrete
    - Surface area: diameter 0.6 m, depth: 1.8 m

7.6 Ropatec:

- Country: Italy
- Website: http://www.ropatec.it
- Operating data:
    - Rated power: 10 kW
    - Cut-in wind speed: 4.5 m/s
    - Rated wind speed: N/A
    - Cut-out wind speed: 25 m/s
    - Survival wind speed: N/A
    - Rated noise level: 40 dB
- Rotor
    - Type: 3-bladed
    - Rotor diameter: 7 m
    - Rotor height: 5.7 m
    - Area: 39.9 m²
    - Blade material: Fiberglass
    - Generator: Permanent Magnet Generator (PMG)

    - Direct drive: Yes
- Tower
    - Type: Jacket
    - Height excluding (including) rotor: 12 (18) m

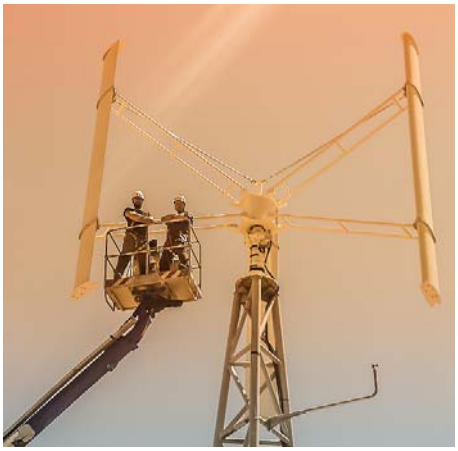

7.7 Dibu Wind:

- Country: Germany
- Website: http://www.dibu-energie.de
- Rated power: 2.0 kW
- Rotor
    - Type: 5-bladed
    - Rotor diameter: 2 m
    - Rotor height: 2.5 m
    - Area: 5 m²
    - Generator: Permanent Magnet Generator (PMG)
    - Direct drive: Yes
- Tower
    - Type: monopile
    - Height excluding rotor: 4.5 m

8 Commercial small Savonius-type (drag-based) VAWTs:

In this section, an overview of commercial small Savonius-type (drag-based) VAWTs with maximum capacity of 10 kW, which is the range considered to be most suitable for urban applications, is presented.

8.1 Silent revolution

- Country: Germany
- Website: http://silentrevolution.com
- Operating data:
  - Rated power: 10 kW
  - Cut-in wind speed: 3.0 m/s
  - Rated wind speed: 16 m/s
  - Cut-out wind speed: 25 m/s
  - Survival wind speed: 52 m/s
  - Rated noise level: Very low
  - Certification: 61400ff. (Prototype certificate 23.02.2017)
- Rotor
  - Two rotors on one tower
  - Rotor height: 10 m
  - Rotor diameter: 1 m
  - Area: 20 m²
  - Blade material: Aluminum
  - Generator: Permanent Magnet Generator (PMG)
  - Self-starting
  - Space for advertisement: 28 m2
- Tower
  - Type: Steel with corrosion-resistant coating
  - Height including rotor: 20 m
- Foundation
  - Material: Poured concrete
  - Surface area: Diameter 0.6 m, depth: 1.8 m

8.2 KLiUX energies

- Country: Spain
- Website: www.kliux.com
- Operating data:
  - Rated power: 1.8 kW
  - Cut-in wind speed: 3.0 m/s
  - Max RPM: 106
  - Noise level: 32.6 dBA at 10 m/s
  - Lifetime: 25 years
  - Certification: ISO 9001 and 14001, CE, IEC 61400-2/-11/-12 (the last one is in progress)
- Rotor
  - Rotor height: 3.1 m
  - Rotor diameter: 2.36 m
  - Area: 7.3 m²
  - Blade material: Expanded polyurethane
  - Generator: Permanent Magnet Generator (PMG)
  - Self-starting
  - Wight: 375 kg
- Tower
  - Type: Steel with corrosion-resistant coating
  - Height including rotor: 9.15 m
- Foundation
  - Material: Poured concrete
  - Surface area: Diameter 0.6 m, depth: 1.8 m

8.3 City wind mills

- Country: UK, USA, Switzerland
- Website: www.city-windmills.com
- Rated power: 0.5, 1.0, 2.0 kW
- More information not available

8.4 Turbina Energy AG

- Country: Germany
- Website: www.turbina.de
- Rated power: 00.25, 0.5, 1.0, 4.0 kW
- More information not available

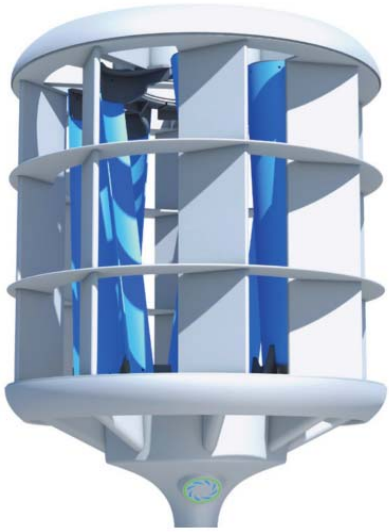

9 Building height in the Netherlands

In this section, the distribution of building height across the Netherlands is presented where the data are obtained from the database: skyscraperpage.com. In this analysis, the low-rise buildings, height smaller than 35 m are not considered, therefore, the analysis considers medium-rise and high-rise buildings, height between 35 m to 100 m, and skyscrapers, height above 100 m, across 85 cities in the Netherlands.

An overall distribution of building height across the Netherlands is presented in Table 2 and Fig. 7. Fig. 8 illustrates the distribution of building height for four largest cities in the Netherlands, namely Amsterdam, Rotterdam, The Hague and Utrecht. Distribution of building height for 13 major cities in the Netherlands is

presented in Table 3 and Fig. 9. These cities are selected as they include the largest number of buildings with height above 35 m. The average building height for major cities in the Netherlands in shown in Fig. 10. The database for building height across 85 cities in the Netherlands is shown in Table 4.

Table 2. Overall distribution of building height across the Netherlands.

Type	Buildings height [m]	Number of Buildings	Percentage [%]
High-rise building	35-40	752	30.04
	40-50	988	39.47
	50-60	378	15.1
	60-70	150	5.99
	70-80	111	4.43
	80-90	43	1.72
	90-100	27	1.08
Skyscraper	100-110	26	1.04
	110-120	3	0.12
	120-130	6	0.24
	130-140	4	0.16
	140-150	7	0.28
	150-160	5	0.2
	160-170	2	0.08
	170-180	0	0
	180-190	1	0.04
	Total	2503	

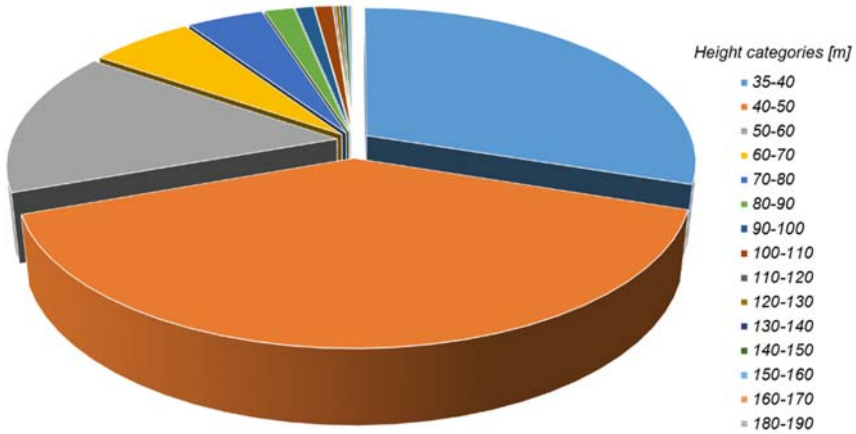

Figure 7. Pie chart showing the distribution of the building height in the Netherlands.

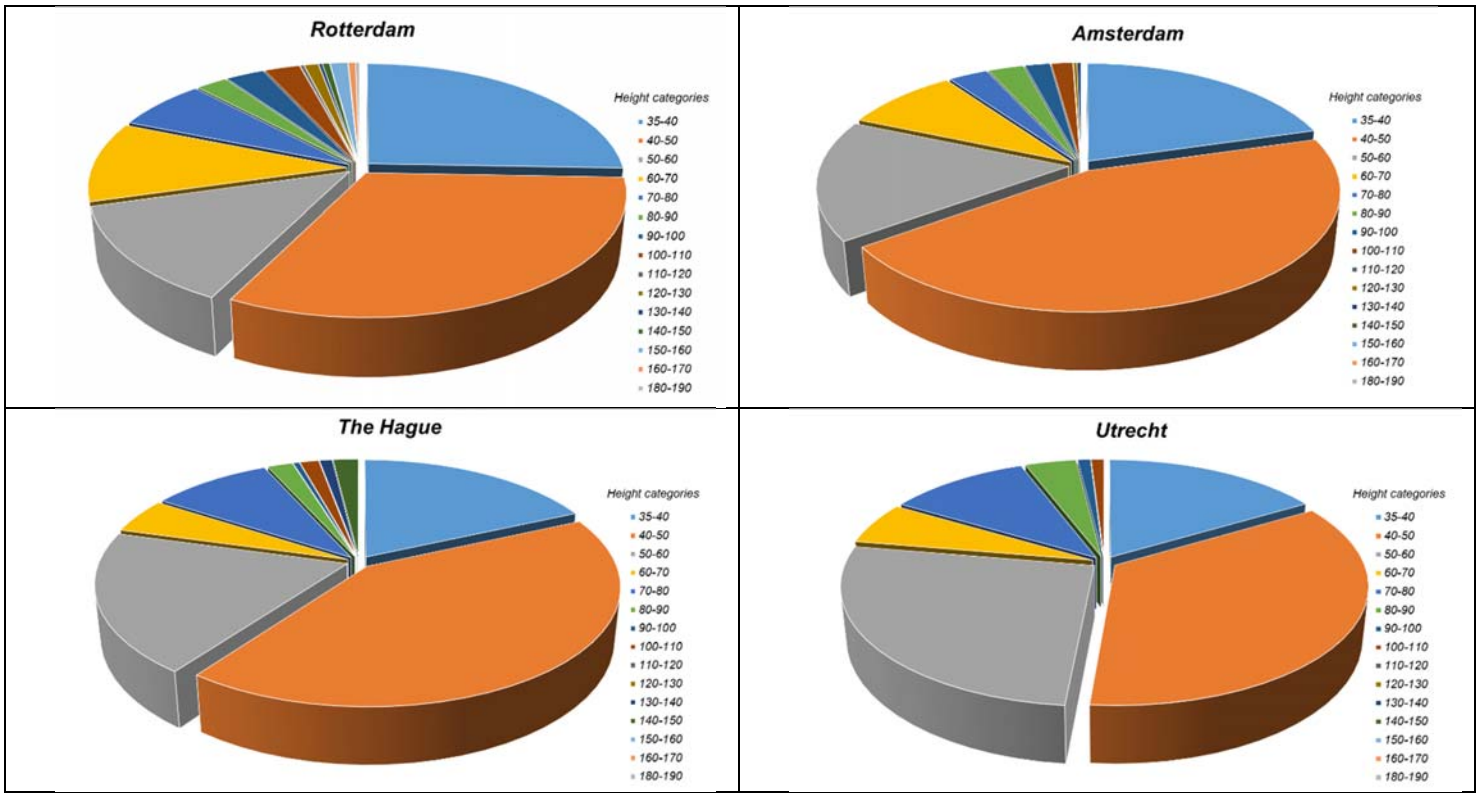

Figure 8. Pie chart illustrating the distribution of building height for the four largest cities in the Netherlands.

Table 3. Distribution of building height for major cities in the Netherlands.

Height [m]	Rotterdam	Amsterdam	The Hague	Utrecht	Eindhoven	Groningen	Delft	Amstelveen	Zoetermeer	Rijswijk	Tilburg	Nijmegen
35-40	98	75	38	17	25	11	19	14	6	21	11	21
40-50	122	163	87	36	30	30	20	33	27	17	21	18
50-60	50	60	40	27	18	12	11	6	6	5	11	5
60-70	41	32	10	6	5	2	0	0	10	3	2	0
70-80	26	11	19	11	5	6	1	0	2	1	1	1
80-90	9	10	4	4	1	1	2	0	0	3	0	2
90-100	11	7	1	1	2	1	1	0	0	0	1	0
100-110	10	6	3	1	2	0	0	0	0	1	1	0
110-120	1	0	0	0	0	0	0	0	0	0	0	0
120-130	4	1	0	0	0	0	0	0	0	0	0	0
130-140	1	1	2	0	0	0	0	0	0	0	0	0
140-150	2	0	4	0	0	0	0	0	0	0	1	0
150-160	5	0	0	0	0	0	0	0	0	0	0	0
160-170	2	0	0	0	0	0	0	0	0	0	0	0

180-190	1	0	0	0	0	0	0	0	0	0	0	0

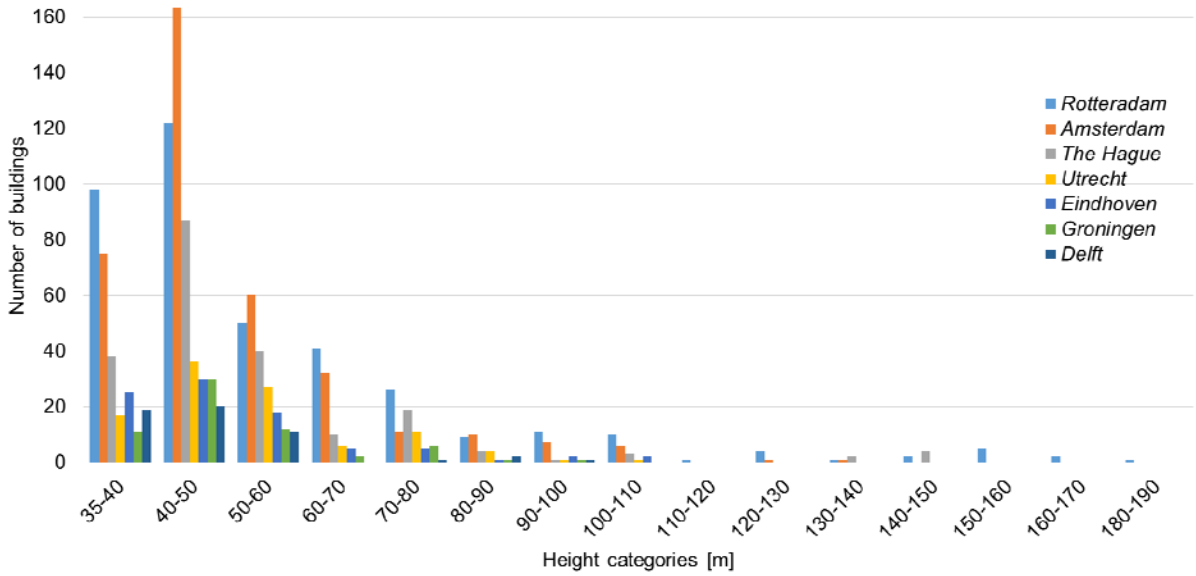

Figure 9. Number of buildings with different heights for major cities in the Netherlands.

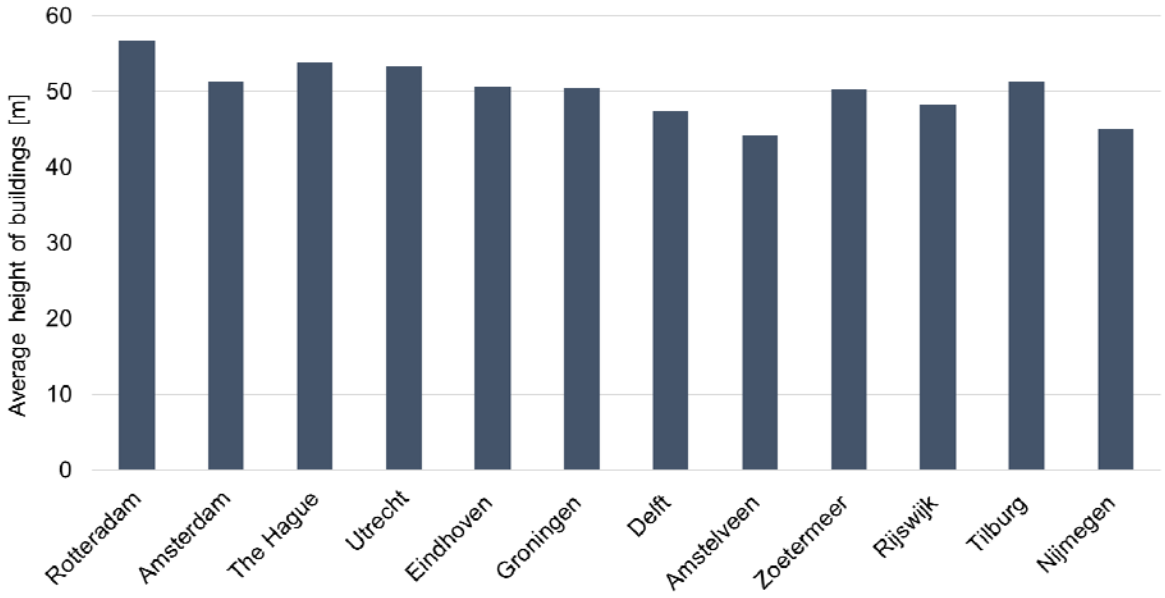

Figure 1. Average building height for major cities in the Netherlands.

Table 4. Database for building height for 85 cities in the Netherlands.

Height [m]	35-40	40-50	50-60	60-70	70-80	80-90	90-100	100-110	110-120	120-130	130-140	140-150	150-160	160-170	170-180	180-190
Rotterdam	98	122	50	41	26	9	11	10	1	4	1	2	5	2	0	1
Amsterdam	75	163	60	32	11	10	7	6	0	1	1	0	0	0	0	0
The Hague	38	87	40	10	19	4	1	3	0	0	2	4	0	0	0	0
Utrecht	17	36	27	6	11	4	1	1	0	0	0	0	0	0	0	0
Eindhoven	25	30	18	5	5	1	2	2	0	0	0	0	0	0	0	0
Groningen	11	30	12	2	6	1	1	0	0	0	0	0	0	0	0	0
Delft	19	20	11	0	1	2	1	0	0	0	0	0	0	0	0	0
Amstelveen	14	33	6	0	0	0	0	0	0	0	0	0	0	0	0	0
Zoetermeer	6	27	6	10	2	0	0	0	0	0	0	0	0	0	0	0
Rijswijk	21	17	5	3	1	3	0	1	0	0	0	0	0	0	0	0
Tilburg	11	21	11	2	1	0	1	1	0	0	0	1	0	0	0	0
Nijmegen	21	18	5	0	1	2	0	0	0	0	0	0	0	0	0	0
Haarlem	19	15	2	1	0	0	0	0	0	0	0	0	0	0	0	0
Capelle aan den IJssel	11	14	4	3	1	1	0	0	0	0	0	0	0	0	0	0
Schiedam	15	13	3	2	0	0	0	0	0	0	0	0	0	0	0	0
Vlaardingen	11	19	1	1	1	0	0	0	0	0	0	0	0	0	0	0
Arnhem	12	9	4	2	5	0	0	0	0	0	0	0	0	0	0	0
Leiden	5	16	11	4	1	0	0	0	0	0	0	0	0	0	0	0
Breda	13	12	3	3	1	0	0	0	0	0	0	0	0	0	0	0
Enschede	11	14	6	0	0	0	0	1	0	0	0	0	0	0	0	0
Heerlen	13	8	6	2	0	0	0	0	0	0	0	0	0	0	0	0
Amersfoort	11	11	6	2	0	0	0	0	0	0	0	0	0	0	0	0
Apeldoorn	11	8	6	3	1	0	0	0	0	0	0	0	0	0	0	0
Leeuwarden	8	14	4	0	1	0	0	0	1	0	0	0	0	0	0	0
s-Hertogenbosch	5	18	2	0	1	0	0	1	0	0	0	0	0	0	0	0
Purmerend	14	10	0	1	0	0	0	0	0	0	0	0	0	0	0	0
Zaanstad	7	11	4	2	1	0	0	0	0	0	0	0	0	0	0	0
Zwolle	13	10	0	1	2	0	1	0	0	0	0	0	0	0	0	0
Almere	6	10	6	0	2	3	0	0	0	1	0	0	0	0	0	0
Haarlemmermeer	9	13	1	0	3	1	0	0	0	0	0	0	0	0	0	0
Diemen	13	2	5	0	0	0	0	0	0	0	0	0	0	0	0	0
Dordrecht	5	10	3	1	0	0	0	0	0	0	0	0	0	0	0	0
Spijkenisse	7	3	5	1	2	0	1	0	1	0	0	0	0	0	0	0
Roermond	10	7	0	1	0	0	0	0	0	0	0	0	0	0	0	0
Leidschendam	2	9	4	2	0	0	0	0	0	0	0	0	0	0	0	0
Deventer	14	1	1	0	0	0	0	0	0	0	0	0	0	0	0	0
Vlissingen	7	4	4	0	0	1	0	0	0	0	0	0	0	0	0	0
Venlo	9	4	0	1	1	0	0	0	0	0	0	0	0	0	0	0
Wageningen	5	3	5	1	0	0	0	0	0	0	0	0	0	0	0	0
Maastricht	2	8	3	0	0	0	0	0	0	0	0	0	0	0	0	0
Veenendaal	9	4	0	0	0	0	0	0	0	0	0	0	0	0	0	0
Alphen aan den Rijn	12	1	0	0	0	0	0	0	0	0	0	0	0	0	0	0

Nieuwegein	5	6	1	0	0	0	0	0	0	0	0	0	0	0	0	0
Sittard-Geleen	9	2	1	0	0	0	0	0	0	0	0	0	0	0	0	0
Maassluis	3	5	2	1	0	0	0	0	0	0	0	0	0	0	0	0
Ridderkerk	0	3	7	0	1	0	0	0	0	0	0	0	0	0	0	0
Assen	6	2	1	1	0	0	0	0	0	0	0	0	0	0	0	0
Emmen	6	3	1	0	0	0	0	0	0	0	0	0	0	0	0	0
Terneuzen	3	6	0	0	1	0	0	0	0	0	0	0	0	0	0	0
Ede	6	2	0	0	0	0	0	0	0	0	0	0	0	0	0	0
Gouda	1	6	1	0	0	0	0	0	0	0	0	0	0	0	0	0
Hengelo	5	3	0	0	0	0	0	0	0	0	0	0	0	0	0	0
Hilversum	3	4	0	0	0	0	0	0	0	0	0	0	0	0	0	0
Rheden	4	3	0	0	0	0	0	0	0	0	0	0	0	0	0	0
Zwijndrecht	4	1	0	1	1	0	0	0	0	0	0	0	0	0	0	0
Almelo	2	2	2	0	0	0	0	0	0	0	0	0	0	0	0	0
Heerenveen	1	5	0	0	0	0	0	0	0	0	0	0	0	0	0	0
Krimpen aan den IJssel	1	1	4	0	0	0	0	0	0	0	0	0	0	0	0	0
Lelystad	5	1	0	0	0	0	0	0	0	0	0	0	0	0	0	0
Roosendaal	2	3	1	0	0	0	0	0	0	0	0	0	0	0	0	0
Smallingerland	0	6	0	0	0	0	0	0	0	0	0	0	0	0	0	0
Velsen	0	6	0	0	0	0	0	0	0	0	0	0	0	0	0	0
Alkmaar	4	0	1	0	0	0	0	0	0	0	0	0	0	0	0	0
Bergen op Zoom	2	3	0	0	0	0	0	0	0	0	0	0	0	0	0	0
Leiderdorp	0	6	0	0	0	0	0	0	0	0	0	0	0	0	0	0
Stichtse Vecht	4	0	1	0	0	0	0	0	0	0	0	0	0	0	0	0
Zeist	2	2	1	0	0	0	0	0	0	0	0	0	0	0	0	0
De Bilt	4	0	0	0	0	0	0	0	0	0	0	0	0	0	0	0
Delfzijl	3	1	0	0	0	0	0	0	0	0	0	0	0	0	0	0
Geldrop-Mierlo	1	2	0	0	0	0	0	0	0	0	0	0	0	0	0	0
Kampen	4	0	0	0	0	0	0	0	0	0	0	0	0	0	0	0
Papendrecht	3	1	0	0	0	0	0	0	0	0	0	0	0	0	0	0
Barendrecht	1	1	0	1	0	0	0	0	0	0	0	0	0	0	0	0
Brunssum	1	2	0	0	0	0	0	0	0	0	0	0	0	0	0	0
Den Helder	0	3	0	0	0	0	0	0	0	0	0	0	0	0	0	0
Goes	3	0	0	0	0	0	0	0	0	0	0	0	0	0	0	0
Gorinchem	1	0	2	0	0	0	0	0	0	0	0	0	0	0	0	0
Helmond	0	3	0	0	0	0	0	0	0	0	0	0	0	0	0	0
Houten	1	1	0	1	0	0	0	0	0	0	0	0	0	0	0	0
Katwijk	0	3	0	0	0	0	0	0	0	0	0	0	0	0	0	0
Sluis	2	1	0	0	0	0	0	0	0	0	0	0	0	0	0	0
Stadskanaal	0	2	2	0	0	0	0	0	0	0	0	0	0	0	0	0
Vaals	3	0	0	0	0	0	0	0	0	0	0	0	0	0	0	0
Veldhoven	1	1	0	0	0	1	0	0	0	0	0	0	0	0	0	0
Zandvoort	1	1	0	0	1	0	0	0	0	0	0	0	0	0	0	0

10 Mean wind speed in the Netherlands

In this section, the distribution of mean wind speed across the Netherlands is presented. Based on the 10-year averaged mean wind speed, the Netherlands is divided into the following four regions (Fig. 11):

1) Zone 1 - very high wind speed region: where the mean wind speed at 100 m is higher than 8 m/s.
2) Zone 2 - high wind speed region: where the mean wind speed at 100 m is between 7.5 and 8 m/s.
3) Zone 3 - medium wind speed region: where the mean wind speed at 100 m is between 7 and 7.5 m/s.
4) Zone 4 - low wind speed: where the mean wind speed at 100 m is lower than 7 m/s.

The mean wind speed at different heights for the 13 major cities in the Netherlands are shown in Table 5 and the wind profiles are plotted in Fig. 12. As mentioned in Section 10, these cities are selected because they include the largest number of buildings higher than 35 m.

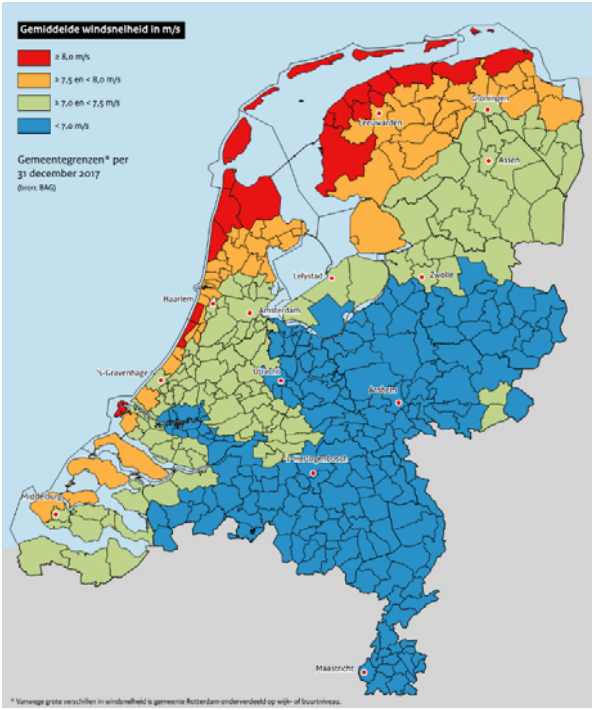

Figure 2. Mean wind speed distribution at 100 m height averaged over 10 years (2004-2013) across the Netherlands (source: KNMI, CBS and RVO.nl).

Table 5. mean wind speed at different heights for the major cities in the Netherlands (data from 'rvo.nl').

	Mean wind speed [m/s]											
Height [m]	**Rotterdam**	**Amsterdam**	**The Hague**	**Utrecht**	**Eindhoven**	**Groningen**	**Delft**	**Amstelveen**	**Zoetermeer**	**Rijswijk**	**Tilburg**	**Nijmegen**
40	7.86	6.15	6.43	5.15	4.62	5.53	5.60	5.69	5.73	5.51	4.82	4.67
50	8.08	6.39	6.79	5.49	4.96	5.92	5.98	6.03	6.08	5.89	5.20	5.10
60	8.26	6.59	7.08	5.77	5.24	6.24	6.29	6.31	6.37	6.19	5.52	5.46
70	8.40	6.78	7.31	6.02	5.49	6.54	6.54	6.54	6.60	6.46	5.78	5.77
80	8.53	6.94	7.51	6.24	5.71	6.80	6.76	6.75	6.81	6.69	6.02	6.03
90	8.66	7.11	7.73	6.48	5.94	7.07	7.00	6.97	7.02	6.94	6.26	6.32

100	8.78	7.27	7.92	6.69	6.15	7.32	7.21	7.16	7.22	7.16	6.49	6.58
110	8.87	7.40	8.06	6.86	6.33	7.51	7.37	7.31	7.37	7.33	6.66	6.77
120	8.95	7.52	8.20	7.01	6.49	7.68	7.52	7.45	7.50	7.49	6.82	6.95
130	9.04	7.66	8.35	7.19	6.67	7.88	7.69	7.61	7.66	7.67	7.00	7.16
140	9.13	7.78	8.49	7.36	6.84	8.07	7.84	7.76	7.80	7.84	7.17	7.35
150	9.20	7.90	8.61	7.52	7.00	8.24	7.99	7.90	7.93	7.99	7.33	7.53
160	9.28	8.02	8.73	7.66	7.15	8.40	8.12	8.03	8.06	8.14	7.48	7.70

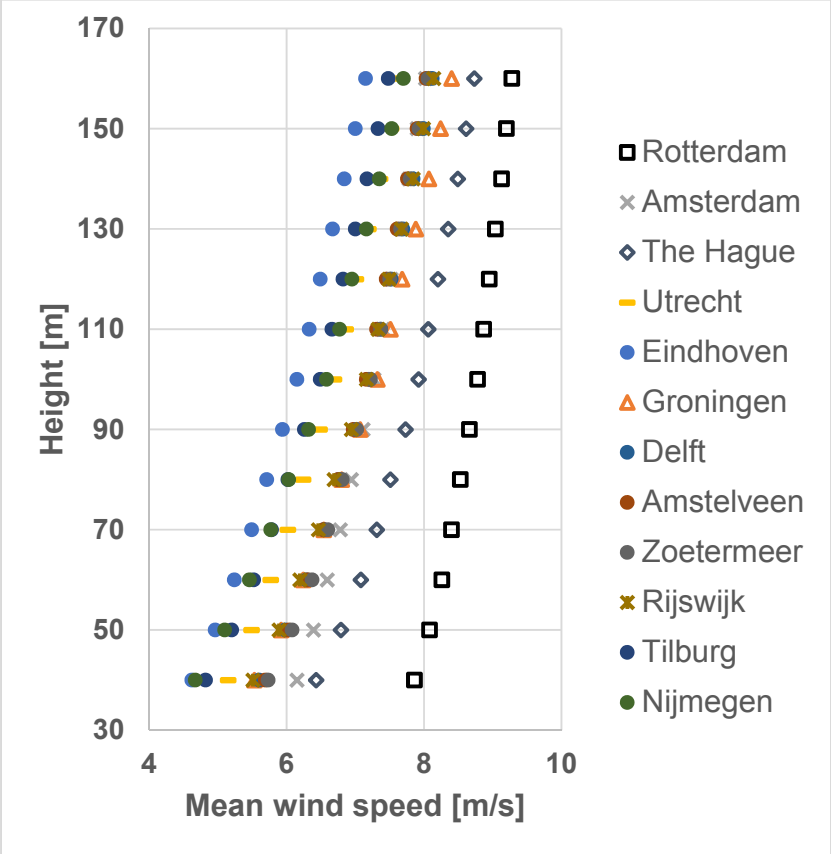

Figure 3. Mean wind speed versus height for major cities in the Netherlands (data from 'rvo.nl').

11 Annual wind speed distribution in the Netherlands

In the analysis, a typical Weibull distribution for the urban environment with reasonably favorable wind conditions, e.g. on the roof of a high-rise building, corresponding to a shape parameter of $k = 1.75$ is considered, according to Sunderland et al. (2013). The scale parameter A is calculated based on the different mean wind speed values, shown in Table 6, which later will be used to calculate the annual energy production (AEP) of the proposed wind turbines. The Weibull distributions, calculated using Eq. 1, are shown in Fig. 13 where U and h(U) are wind speed and probability of wind speed, respectively.

$$h(U) = \frac{k}{A}\left(\frac{U}{A}\right)^{k-1} e^{-\left(\frac{U}{A}\right)^{k}} \quad (1)$$

Table 6. Assumed Weibul distribution for the urban wind speed with different mean values.

	Weibull distribution parameters	
Mean wind speed [m/s]	A	k
5.0	5.61	1.75
5.5	6.18	1.75
6.0	6.74	1.75
6.5	7.30	1.75
7.0	7.86	1.75
7.5	8.42	1.75
8.0	8.98	1.75
8.5	9.54	1.75
9.0	10.10	1.75
9.5	10.67	1.75

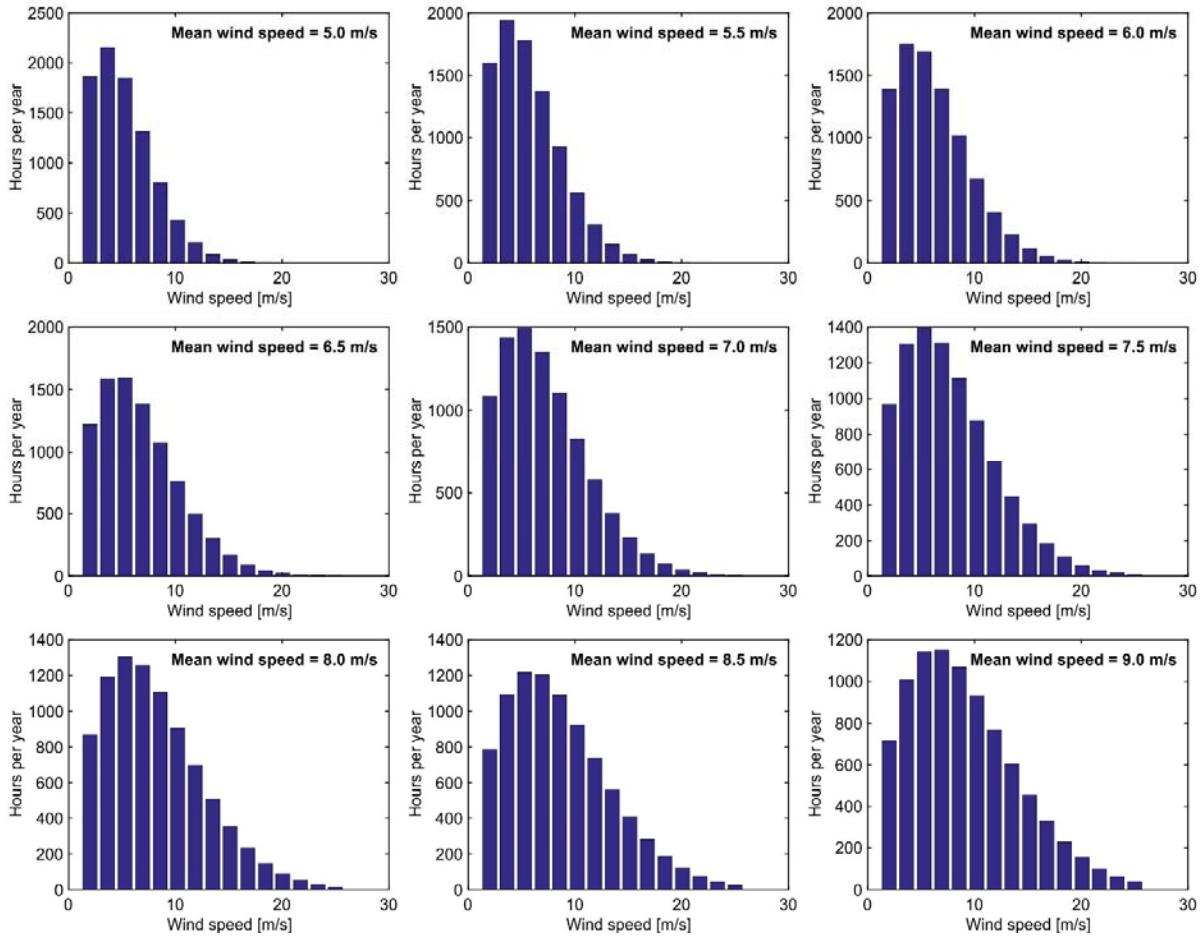

Figure 13. Annual wind speed distribution for different mean wind speeds.

12 Distribution of buildings based on their roof mean wind speed

As the parameter of interest for wind energy harvesting is the mean wind speed of the potential location, i.e. building roof, therefore, it is needed to quantify the number of potential buildings for wind energy harvesting with respect to their roof mean wind speed. Table 7 and 8 present the number of buildings with respect to their roof mean wind speed for the major cities across the Netherlands. No amplification factor due to the acceleration of the flow over the building roof is considered, therefore, the roof mean wind speed values presented in Table 7 and 8 correspond to the mean wind speed at the respective height in the corresponding city. This is to compensate for uncertainties in the analysis as the wind speed amplification factor on the building roof can be a local parameter dependent on the building dimensions, the arrangement of the surrounding buildings, the wind direction, etc.

Table 7. Number of buildings with respect to their roof mean wind speed for the 13 major cities across the Netherlands.

Mean wind speed [m/s]	5	5.5	6	6.5	7	7.5	8	8.5	9	9.5
# buildings with this roof mean wind speed	144	106	239	473	110	45	230	123	35	8

Table 8. Number of buildings with respect to their roof mean wind speed with details of each major city.

	Mean wind speed [m/s]	5	5.5	6	6.5	7	7.5	8	8.5
Rotterdam	Height [m]							35-50	50-80
	# buildings							220	117
Amsterdam	Height [m]				35-60	60-90	90-120	120-160	
	# buildings				298	53	13	2	
The Hague	Height [m]				35-50	50-60	60-80	80-110	110-150
	# buildings				125	40	29	8	6
Utrecht	Height [m]		35-60	60-70	70-100	100-120			
	# buildings		80	6	16	1			
Eindhoven	Height [m]	35-60	60-80	80-100	100-130				
	# buildings	73	10	3	2				
Groningen	Height [m]			35-60	60-70	70-90	90-110		
	# buildings			53	2	7	1		
Delft	Height [m]			35-60	60-70	70-100			
	# buildings			50	0	4			
Amstelveen	Height [m]			35-50	50-70				
	# buildings			47	6				
Zoetermeer	Height [m]			35-50	50-70	70-90			
	# buildings			33	16	2			
Rijswijk	Height [m]			35-60	60-80	80-100	100-130		
	# buildings			43	4	3	1		
Tilburg	Height [m]	35-50	50-60	60-80	80-110	110-140	140-160		
	# buildings	32	11	3	2	0	1		
Nijmegen	Height [m]	35-50	50-70	70-80	80-100				
	# buildings	39	5	1	2				

9	80-130	35																					
9.5	130-180	8																					

13 Selected turbine characteristics

The geometrical and operational characteristics of the selected turbine are presented in Table 9 with a schematic shown in Fig. 14. The turbine is a variable-speed small-scale (urban) H-type lift-based VAWT with 2 blades equipped with symmetric NACA0018 airfoil cross-section. The turbine has a diameter of 1 m, a height of 5 m, a swept area of 5 m^2 and a low solidity of 0.3. The variable-speed operation allows the turbine to maintain an optimal tip speed ratio of 2.5 within the cut-in to cut-out wind speeds, i.e. 2 – 24 m/s (see Fig. 15a) to maximize the aerodynamic performance. The turbine power performance and power curve calculated using high-fidelity CFD simulations extensively validated with experimental data are shown in Fig. 15b-c (Rezaeiha et al. 2017a, b, c, 2018a, b). The selected turbine employs a high-efficiency (> 97%) direct-drive brushless permanent magnet generator (PMG) where due to the very limited generator losses (< 3%), they are not considered in the presented power curves in Figs. 15b-c.

Table 9. Geometrical and operational characteristics of the selected turbine.

Parameter	**Value**
Type	Vertical axis wind turbine (VAWT) H-type Darrieus (lift-based)
Scale	Small-scale urban
Operation	Variable-speed
Number of blades, n	2
Diameter, d [m]	1
Height, h [m]	5
Swept area, A [m^2]	5
Turbine aspect ratio, h/d	5
Airfoil	NACA0018
Airfoil chord, c [m]	0.15
Solidity, σ	0.30
Blade aspect ratio, h/c	33.33
Shaft diameter [m]	0.04
Tip speed ratio, λ	2.5 (fixed)
Rotational speed, Ω [rad/s]	12.5 – 125
Cut-in wind speed [m/s]	2
Cut-out wind speed [m/s]	24
Noise level [dBA]	20 - 40
Lifetime	25 years
Generator type	Direct-drive brushless permenant magnet generator (PMG)
Estimated generator efficiency	> 97% (Dabiri 2011, 2014)

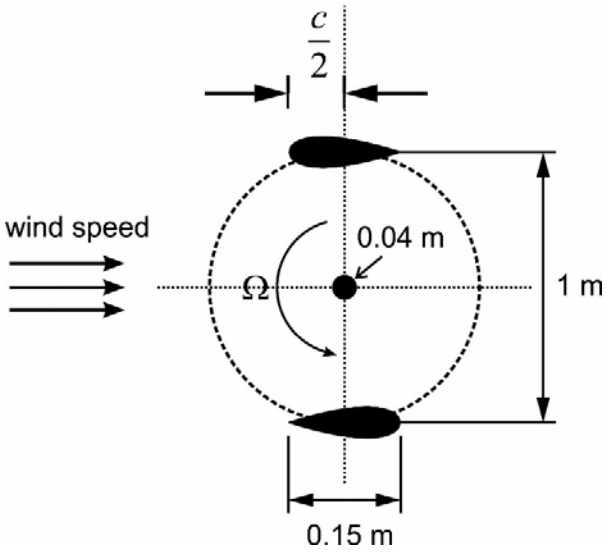

Figure 44. Schematic (top-view) of the selected turbine (not-to-scale).

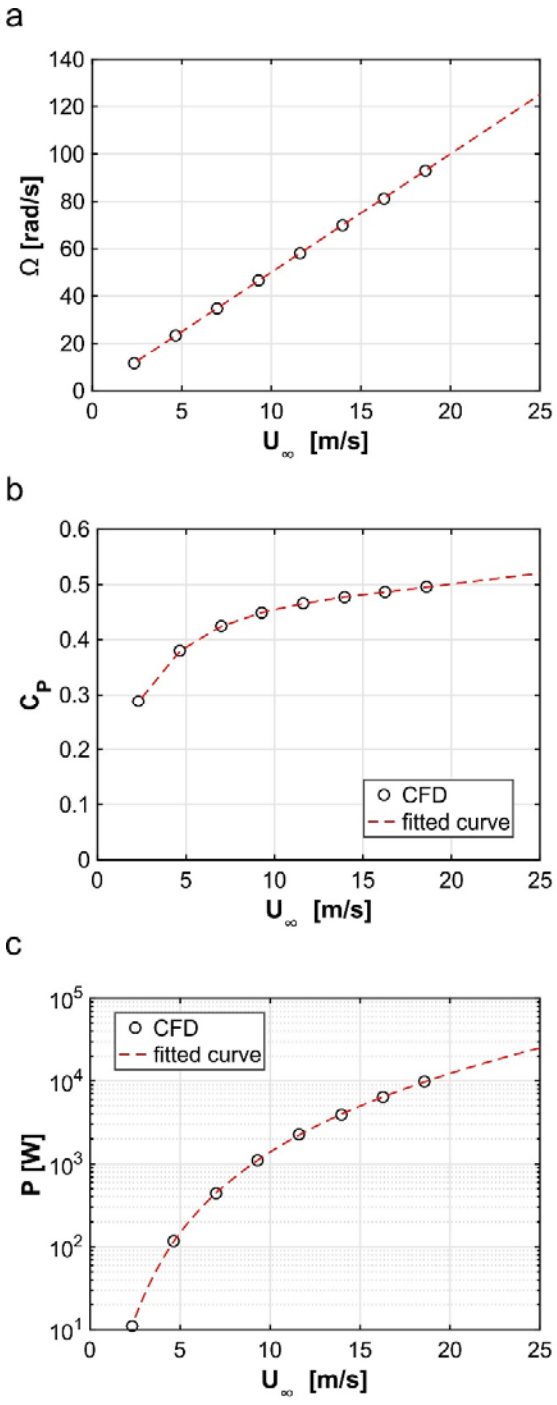

Figure 15. (a) Turbine rotational velocity, (b) power coefficient and (c) power curve (in log-scale) of the selected turbine versus wind speed.

14 Selected turbine arrangement

Research has shown that closely packed counter-rotating VAWTs will benefit from the adjacent turbine vortex system and, therefore, can have a substantially higher power coefficient. Based on this, as shown in

Fig. 16, an arrangement of 12 counter-rotating VAWTs installed on the roof corners is proposed per building. This is an average assumption. Therefore, on average 12 turbines with the selected arrangement are considered to be installed per buildings.

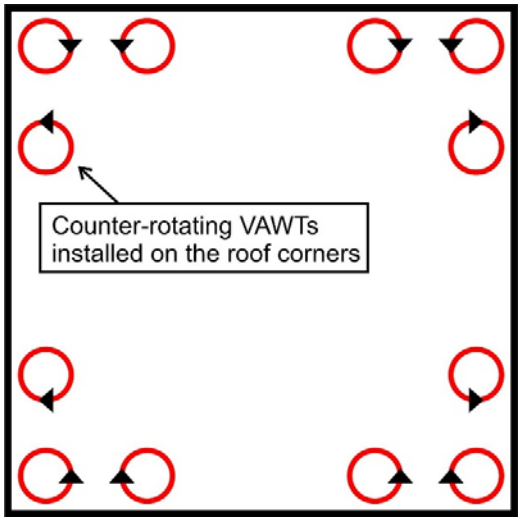

Figure 56. Schematic illustrating the selected arrangement of 12 counter-rotating vertical axis wind turbines installed on the roof corners of a building. Each pair of adjacent turbines is counter-rotating.

15 Prediction of total urban annual energy production (AEP)

In order to calculate the annual energy production (AEP) for these turbines installed in the urban environment, the following data are required: (i) turbine power curve, (ii) distribution of wind speed for potential locations, (iii) number of turbines per roof and (iv) number of buildings where turbines are going to be installed on their roof. Having this information, the AEP of a single turbine at a specific height and the total AEP of all the turbine installed can be calculated using the following steps:

1) Divide the range between cut-in and cut-out wind speeds into several bins, e.g. 11 bins
2) Calculate the probability of wind blowing within each range and the corresponding number of hours per year at the specific mean wind speed
3) Calculate the AEP of a single turbine at the specific mean wind speed (AEPz) using Eq. 2, where 'i' represents the number of the bin, 'Ui' and 'Pi' denote the wind speed and the turbine power at the ith bin, 'A' and 'k' are scale and shape parameters for the corresponding Weibull distribution and '8760' is the total hours per year.

$$AEP_z = \sum_{i=1}^{N-1} \frac{(P_i + P_{i+1})}{2} \times 8760 \times \left\{ e^{-\left(\frac{U_i}{A}\right)^k} - e^{-\left(\frac{U_{i+1}}{A}\right)^k} \right\} \quad (2)$$

4) Calculate the total AEP for all the turbines at the specific mean wind speed (AEPtotal,z) using Eq. 3, where '12' is the number of turbines per building roof and NB,z is the number of buildings at the specific roof mean wind speed given in Table 7:

$$AEP_{total,z} = AEP_z \times 12 \times N_{B,z} \quad (3)$$

5) Calculate the total AEP for all relevant wind speeds (AEP_{total}) using Eq. 4:

$$AEP_{total} = \sum AEP_{total,z} \quad (4)$$

Following the procedure mentioned above the range of wind speeds between cut-in, 2 m/s, and cut-out, 24 m/s, are divided into 11 bins with bin width of 2 m/s. The turbine performance and the number of hours for each bin is shown in Table 10. The row '1' presents the wind speed bins. The rows '3-4' present the turbine C_P and P (W) corresponding to each bin (see Figs. 15 b-c), respectively. The rows '7-16' list the annual number of hours corresponding to each bin with respect to their roof mean wind speed shown on the respective 2nd column. The values presented in Table 10 are, then, employed to calculate the AEP_z using Eq. 2 where for each column, row '4' corresponds to the first part on the right-hand-side and each row, from 7 to 16, present the rest of the right-hand-side. Note that numbers in Table 10 are rounded to the nearest integer number while the actual non-rounded real number is used to obtain the values in Table 11.

Table 10. Turbine power performance and annual wind speed distribution per wind speed bin.

1	Bins [m/s]	2-4	4-6	6-8	8-10	10-12	12-14	14-16	16-18	18-20	20-22	22-24
2		Turbine performance										
3	C_P	0.314	0.386	0.424	0.447	0.462	0.473	0.482	0.489	0.497	0.405	0.513
4	P [W]	26	148	446	997	1880	3181	4977	7357	10436	14312	19095
5												
6	U_{mean}	Annual number of hours										
7	5 m/s	2422	2727	1939	1032	435	150	43	10	2	0	0
8	5.5 m/s	2088	2517	1983	1205	597	248	88	27	7	2	0
9	6 m/s	1823	2315	1972	1326	743	356	148	54	18	5	1
10	6.5 m/s	1606	2125	1926	1404	867	466	221	93	35	12	4
11	7 m/s	1426	1952	1860	1447	968	570	300	142	61	24	9
12	7.5 m/s	1276	1795	1783	1464	1044	664	381	199	95	42	17
13	8 m/s	1150	1655	1701	1460	1100	744	459	260	136	66	30
14	8.5 m/s	1042	1530	1619	1443	1137	812	532	322	181	95	47
15	9 m/s	951	1419	1539	1416	1161	867	597	383	230	130	69
16	9.5 m/s	871	1319	1461	1383	1172	911	657	443	281	168	95

Based on Table 10, AEP_z is calculated as shown in Table 11:

Table 11. Calculation of AEP_z for different mean wind speed bins.

	U_{mean} [m/s]	# hours per year × P											AEP_z [MWh]
1	5	62979	403544	864855	1028572	817836	476141	212930	75650	21885	5231	1045	3.97
2	5.5	54293	372462	884230	1201001	1121904	788155	436290	196634	73893	23475	6377	5.16
3	6	47402	342572	879321	1321766	1396301	1132153	737552	398592	182888	72197	24790	6.54
4	6.5	41757	314541	859095	1399786	1630652	1481859	1098847	686087	368969	173119	71619	8.13
5	7	37084	288863	829630	1442929	1819385	1813225	1493155	1047857	640803	345782	166336	9.93

6	7.5	33179	265665	795177	1459193	1963559	2111095	1894827	1463775	994857	602193	327902	11.91
7	8	29890	244887	758628	1455686	2067857	2368139	2283571	1910929	1418131	944572	570239	14.05
8	8.5	27103	226378	721896	1438280	2138483	2582781	2645607	2368103	1892481	1366274	899707	16.31
9	9	24726	209947	686202	1411604	2181867	2757134	2973110	2818163	2398591	1854504	1314920	18.63
10	9.5	22656	195147	651691	1378559	2204180	2897491	3267745	3256226	2928053	2403392	1817670	21.02

Finally total AEPz and total AEP are calculated and shown in Table 12. A total of 170.5 GWh can be produced annually using the urban wind turbines installed in 13 major cities across the Netherlands.

Table 12. Total AEP generated by urban wind turbine in 13 major cities across the Netherlands.

U_{mean} [m/s]	# buildings with this roof mean wind speed	# turbines per roof	AEP_z	Total AEP_z [GWh]
5	144	12	3970668	6.861
5.5	106	12	5158715	6.562
6	239	12	6535534	18.75
6.5	473	12	8126331	46.125
7	110	12	9925048	13.101
7.5	45	12	1.2E+07	6.432
8	230	12	1.4E+07	38.785
8.5	123	12	1.6E+07	24.069
9	35	12	1.9E+07	7.825
9.5	8	12	2.1E+07	2.019
Total AEP [GWh]				**170.523**

The AEP calculations are based on the following assumptions:

- It is possible to install the small wind turbines on all the high-rise buildings in the aforementioned cities (see Table 5).
- The extracted wind profiles from 'rvo.nl' for each city, shown in Fig. 12, are representative of the actual mean wind conditions in the whole city.
- The employed shape factor, k = 1.75, is a representative of the wind speed distribution for the urban conditions in the studied cities.
- The possible wind speed amplification factor on the building roof is neglected.
- The turbulence impact on the turbine power curve, shown in Figs. 15b-c, is neglected.
- The generator losses, estimated to be less than 3%, are not considered in the turbine power calculations.
- The mutual impact of the adjacent turbines on each other's performance is not considered.
- The turbine performance is assumed to remain constant during the lifetime and any performance degradation, due to the collection of dirt on the blades or other reasons, are not considered.
- The maintenance is supposed to be arranged during the time where the wind speed is below the cut-in velocity, therefore, the turbine is not operational.

16 Some practical aspects

16.1 Noise level

As described in Table 9, the noise level of the selected turbine, within the operational range of wind speed, is predicted to be 20 - 40 dBA. The prediction is based on the actual values of the available commercial Darrieus H-type VAWTs described in Section 8.

16.2 Structural vibration

The vibration measurements by 'BerlinWind GmbH' (Grunwald et al. 2013) for the roof-mounted small Darrieus-type vertical axis wind turbines and root cause analysis has shown the following important issues:

- Variable-speed vertical axis SWT show complicated rotor and structural dynamics due to harmonics of the rotor speed which are relevant for resonance issues of the SWT and the building.
- The design of SWT rotor, support structure and foundation should include the structural dynamics over the entire rotor speed range and for all planned structure variations to prevent resonance issues.
- The degree of building vibration issues strongly depends on the roof type and building structure. For instance, due to higher damping of cement buildings, lower vibrational issues are caused by the turbines while the case is worse for steel framework constructions.
- SWT design, production and installation requires high quality standards as the specific investment per kWh is higher than for large WT and the costs of unexpected issues threaten the project economics fast. Detailed assembly instructions and experienced installation staff are recommended.
- Despite increased O&M efforts of pretensioned guy wires, for their defined pretensioning and inspection, the benefit on reduced resonance issues and defined natural frequencies of the structure is a relevant benefit compared to the braces.
- Aerodynamic and mass imbalance is a potential issue at SWT. Design, manufacture, quality control and professional erection should prevent it at best. Defined easy accessible locations for test and correction masses are necessary. Dynamic balancing of the assembled rotor is required especially for variable-speed SWT.
- Vibration issues of SWT, especially when installed on buildings, increase significantly wear and damages of the SWT threatening the project profit by increased O&M costs and stand still - and the costly root cause analysis. Additional costs for later vibration analysis and SWT modifications are estimated to reach easily 10-20% of the SWT initial costs (depending as well on the SWT size) but lie below the minimum repair costs of vital components if the issues are not addressed.
- For a detailed vibration analysis of SWT with strongly changing rotor speed, advanced measurement and evaluation techniques are required to prevent under-estimation of the real amplitudes which occurs when averaging over too long periods.
- Dampers need to be installed between foundation and roof to minimize resonance issues with the building. Design should take damper resonance, periodic damper inspection and eventual replacement into account. A carefully-designed structural damper for the turbine can significantly reduce the vibrations in the building and can possibly isolate the structural vibrations caused by the turbine. An example of a roof-mounted wind turbine with built-in dampers is shown in Fig. 17.

Figure 6. Small roof-mounted wind turbine with specially-designed vibration dampers (www.envergate.com).

17 Cost estimation

The installed cost of a wind power project is dominated by the upfront capital cost for the wind turbines (including foundation, towers and installation) which can account for as much as 84% of the total installed cost. The capital costs of a wind power project can be broken down into the following major categories:

- The turbine cost: Including rotor, tower and electrical components;
- Foundation: Including construction costs for site preparation and the foundations for the towers and structural damper;
- Grid connection costs: This can include transformers and sub-stations, as well as the connection to the local distribution or transmission network;
- Planning and project costs: These can represent a significant proportion of total costs; and
- Other capital costs: These can include the construction work on the building roof if necessary, control systems, etc.

The breakdown in total costs for a typical land-based wind is shown in Table 13 and Figure 18. These values can vary depending on the location site, the project, and the wind turbines used, which by themselves can account for between 64% and 84% of total installed costs. Similarly grid connection costs can vary between 9% and 14%, construction and civil works from 4% to 16%, while other capital costs typically range between 4% and 10%.

The turbine unit price for a large order quantity of 20,000 turbines in total is estimated to be approximately 5,000 €. The estimated is based on the current price of similar commercial turbines in the market. For instance, the Darrieus H-type 'Royall Power' turbine with a height of 9.1 m and a diameter of

1.4 m (swept area of 12.74 m^2) at a unit order quantity is priced at 6,995 $[2]. Note that the selected turbine has smaller dimensions with a height of 5 m and a diameter of 1 m (swept area of 5 m^2) and the order quantity would be very high, i.e. 18,154.

However, this constitutes the most beneficial situation in terms of costs, where all turbines would be ordered in one large order, which is rather unlikely. Therefore, also a safe estimate is made of 10,000 € per turbine. In this safe estimate, also all other costs are doubled.

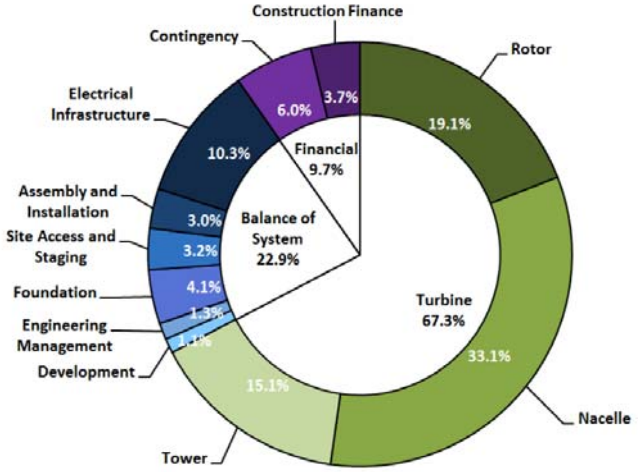

Figure 18. Capital expenditures for the land-based wind turbines from NREL (2017).

Table 13a. Economically beneficial estimate: Breakdown in total costs for urban wind energy with characteristics discussed in Sections 14-16.

Upfront capital cost	Turbine	Wind turbine (rotor, tower and generator)	90.78 million € (18,156 turbines with a unit price of 5000 €)	67.3%
	Balance of systems	Electrical infrastructure	13.89 million €	10.3%
		Assembly and installation	4.04 million €	3.0%
		Site access and staging	4.31 million €	3.2%
		Foundation	5.53 million €	4.1%
		Engineering management	1.75 million €	1.3%
		Development	1.48 million €	1.1%
	Financial	Construction finance	4.99 million €	3.7%
		Contingency	8.09 million €	6.0%
	SUM		134.89 million €	100%

[2] http://www.shoproyall.com/750w-Wind-Turbine-System_p_331.html

Lifetime O&M costs	20.23 million €	15% of upfront capital cost
Total project cost	155.12 million €	

Table 14b. Safe estimate: Breakdown in total costs for urban wind energy with characteristics discussed in Sections 14-16.

Upfront capital cost	Turbine	Wind turbine (rotor, tower and generator)	181.56 million € (18,156 turbines with a unit price of 10,000 €)	67.3%
	Balance of systems	Electrical infrastructure	27.78 million €	10.3%
		Assembly and installation	8.08 million €	3.0%
		Site access and staging	8.62 million €	3.2%
		Foundation	11.06 million €	4.1%
		Engineering management	3.50 million €	1.3%
		Development	2.96 million €	1.1%
	Financial	Construction finance	9.98 million €	3.7%
		Contingency	16.18 million €	6.0%
	SUM		269.78 million €	100%
Lifetime O&M costs			40.46 million €	15% of upfront capital cost
Total project cost			310.24 million €	

LCOE, or levelized cost of energy, Eq. 5, is a term which describes the cost of the power produced over a period of time, typically the warrantied life of the system. The calculations presented here does not take into account any tax benefit, discounted feed-in tariff or interest rate. To further dig into the details, a dedicated extensive cost analysis is required. The values are presented in Table 14a and 14b.

$$LCOE = \frac{Lifetime\ cost\ of\ the\ project}{Lifetime\ energy\ production} \tag{5}$$

Table 15a. Economically beneficial estimate. Details of the levelized cost of energy.

Turbine lifetime	**25 years**
Lifetime energy production	**4263.075 GWh (25 × 170.523 GWh)**
Safety factor	**1.25**
Lifetime cost of the project	**1.25 × 155.12 million € = 193.9 million €**
Levelized cost of energy (LCOE)	**45.48 €/MWh (~ 0.045 €/kWh)**

Table 16b. Safe estimate. Details of the levelized cost of energy.

Turbine lifetime	**25 years**
Lifetime energy production	**4263.075 GWh (25 × 170.523 GWh)**
Safety factor	**1.25**
Lifetime cost of the project	**1.25 × 310.24 million € = 387.8 million €**
Levelized cost of energy (LCOE)	**90.96 €/MWh (~ 0.091 €/kWh)**

18 Other types of wind energy integration in the built environment

As mentioned earlier, much less attention in wind energy has been given to wind energy installations near buildings (Campbell and Stankovic 2001, Beller 2009, Sharpe and Proven 2010). The concept of on-site micro wind energy generation is interesting because the energy is then produced close to the location where it is required. Campbell and Stankovic (2001) distinguish between three categories of possibilities for integration of wind energy generation systems into urban environments: (1) siting stand-alone wind turbines in urban locations; (2) retrofitting wind turbines onto existing buildings; and (3) full integration of wind turbines together with architectural form. Category 2 and 3 are often referred to as "building-integrated wind turbines".

Most of the early actual installations of wind turbines in urban contexts have been established in category 1 (Sharpe and Proven 2010). They were generally conventional HAWTs, intended to be mounted on the top of masts in fairly open areas. The performance of these systems has been reported to be very site-specific (Peacock et al. 2008) and in many cases the proximity to buildings has decreased the performance (e.g. Mithraratne 2009). Campbell and Stankovic (2001), Mertens (2006), Lu and Ip (2009) and Balducci et al. (2012a, 2012b), among others, investigated the potential to take advantage of augmented airflow around buildings, addressing both category 2 and category 3 applications. Category 2 includes traditional or newly developed wind turbines that can be fitted onto either existing buildings or new buildings, without the need for specially modifying the building form. Examples are the roof-mounted ducted wind turbine by Grant et al. (2008), the modern adaptation to the Sistan wind energy mill by Müller et al. (2009), the Crossflex design by Sharpe and Proven (2010), which is a new development of a Darrieus turbine form, and the 3-in-1 wind–solar and rain water harvester with power-augmentation-guide-vane (PAGV) for a Vertical Axis Wind Turbine (VAWT) by Chong et al. (2011). Finally, category 3 consists of modified building forms for full integration of wind turbines. Well-known examples of buildings designed for integration of large-scale wind turbines are the Bahrain World Trade Center, the Strata Tower in London and the Pearl River Tower in Guangzhou, China.

For completeness, a number of available or recently/currently investigated systems are mentioned below, however not with the intention to be complete/exhaustive.

Roof-integrated wind turbines.

A variety of roof-integrated systems has been devised that all belong to Category 3. These systems consist of a special roof configuration in which one or more VAWTs can be embedded. An example is the Powerdak 1.0 concept developed by Bronsema (2005, 2010, 2013). The philosophy of the Powerdak 1.0 (Fig. 19) is to exploit the Venturi effect to increase the wind speed in the narrowest part of the roof where a VAWT is located. However, one should carefully balance the increase of wind speed or flow rate by the contraction on the one hand, and the increase of flow resistance by this contraction itself and by possible vertical guiding vanes (van Hooff et al. 2011, Blocken et al. 2011, van Hooff et al. 2012). A common error made in the evaluation of this type of configurations is that the ratio between the wind speed at the narrowest section of the contraction and the wind

speed at the inlet of the contraction is used to calculate the wind energy potential based on meteorological data linked to the wind speed at the inlet. However, due to the large flow resistance that is induced by these roof configurations, the wind speed at the inlet of the roof will already be much lower than the meteorological wind speed at that height. This misconception can easily lead to unrealistic expectations that cannot be realized in practice. This is clearly shown in Figure 20 that shows the amplification of the mean wind speed in a horizontal and vertical plane through the roof construction. The amplification factor is defined as the ratio of the local wind speed to the wind speed at roof height without building present. As such, the first two configurations in Fig. 20 seem to yield no increase in the narrowest part of the contraction, as the amplification factor is equal to one. The reason is that these roof constructions present such a large obstruction to the wind in terms of flow resistance that the wind speed at the inlet of the roof construction is reduced by up to a factor 10 or more. The subsequent real Venturi effect that only occurs in the closed channels between the inlet of the contraction and the narrowest part of the contraction does yield an increase in wind speed, but apparently just enough to compensate the earlier reduction, yielding a net zero benefit. However, the Powerdak 1.0 design without vertical guiding vanes does yield a substantial increase in wind speed, up to a factor 1.35. Note that the first two roof configurations only provide space for a single VAWT at the position of the highest amplification factor, while the configuration without vertical guiding vanes provides space for placing several VAWTs.

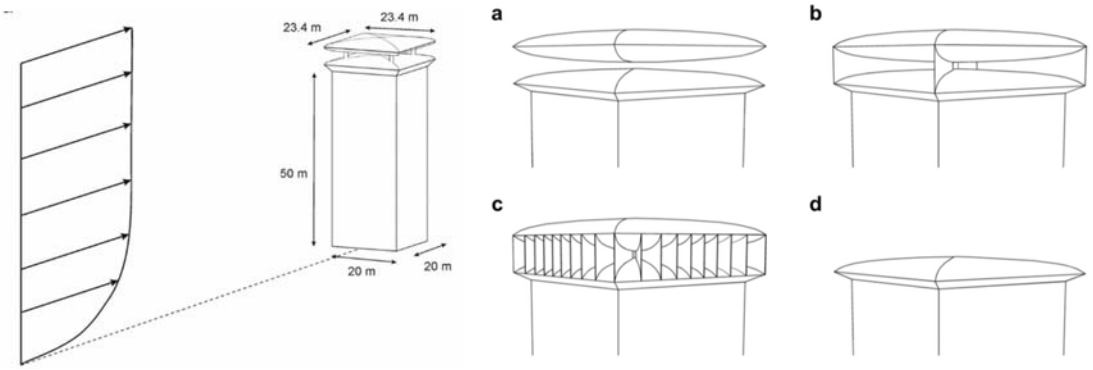

Figure 19. Analyzed configurations for roof-integrated wind turbine systems (van Hooff et al. 2011). Configuration (a) without vertical guiding vanes is the Powerdak 1.0 concept by Bronsema.

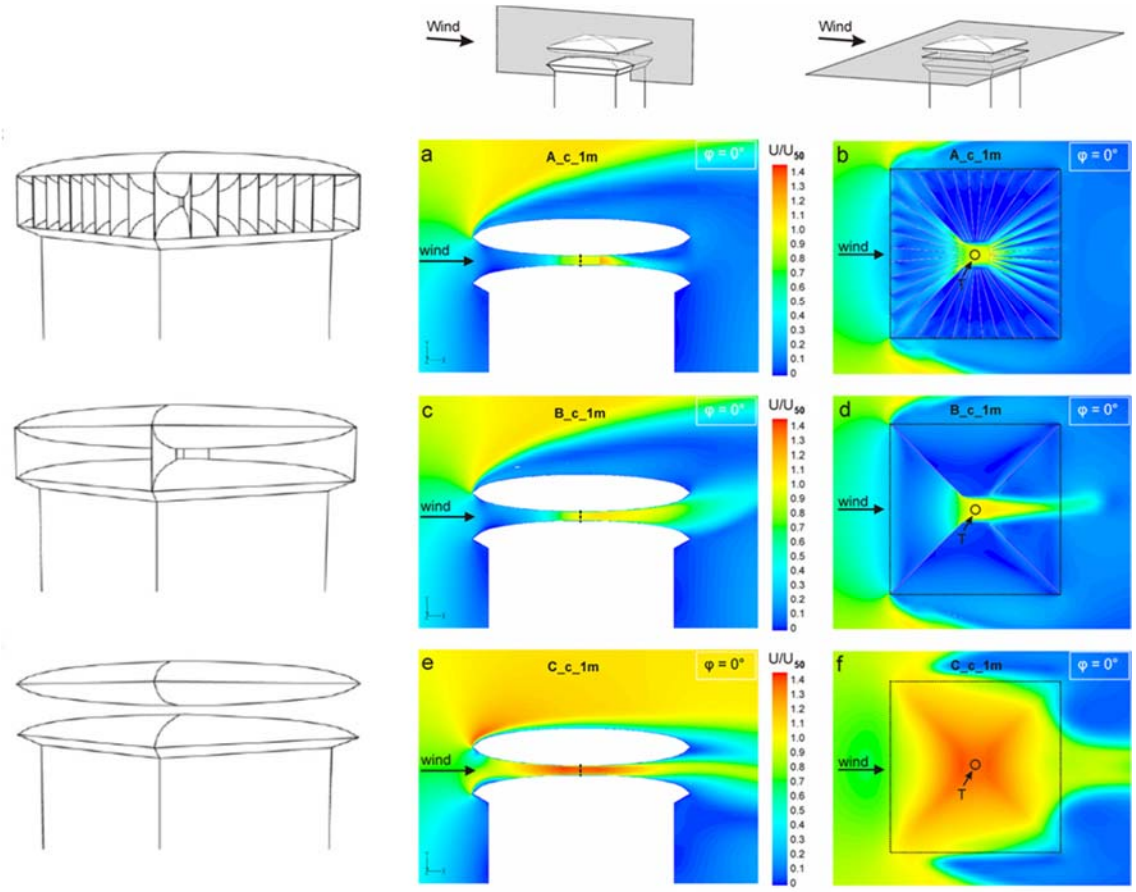

Figure 20. Wind speed amplification for different roof-integrated wind turbine configurations including the Powerdak 1.0 (van Hooff et al. 2011).

The preprints of these publications are provided at the end of the appendices. Three important disadvantages of this system are: (1) the added costs for the special roof construction; (2) the increased flow resistance through the roof due to the added guiding vanes, which reduce the wind speed and the power output; and (3) the limited space and height to add multiple and especially higher wind turbines. For these reasons, Bronsema has abandoned the original concept of the Powerdak (Powerdak 1.0; Fig. 19 and 20) and has moved towards the concepts of the Powerdak 2.0 and later 3.0 (Fig. 21), that include the installation of wind turbines on existing roofs, however, with rounded roof edges to avoid large areas of separated flow over the roof (Bronsema 2017, Blocken 2016c, d). However, even when the three above-mentioned problems are solved, the same essential problem for practical implementation remains: the current lack of highly efficient and reliable VAWTS. Recent concerted efforts towards the development of a new, efficient and reliable VAWT have been performed at Eindhoven University of Technology in the framework of the European Horizon2020 ITN project AEOLUS4FUTURE (Rezaeiha et al. 2017b, c, d, 2018a, b). The turbine characteristics resulting from this project have been used in the estimates of the urban wind energy potential in this report. Note that the Powerdak 3.0 concept has not been assumed in the present report but that it provides possibilities to increase the wind energy potential in the Netherlands further, however at the expense of increased costs for the establishment of the rounded roof edges.

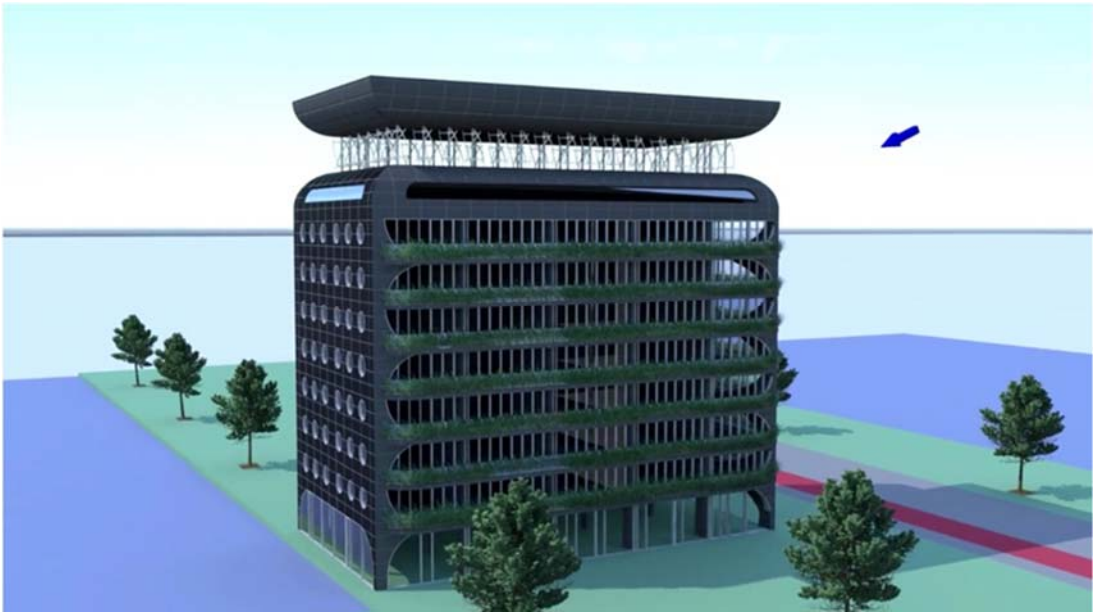

Figure 21a. Sketch of Breeze hotel with implementation of Powerdak 1.0 (not actually implemented due to abandonment of Powerdak 1.0 by its inventor).

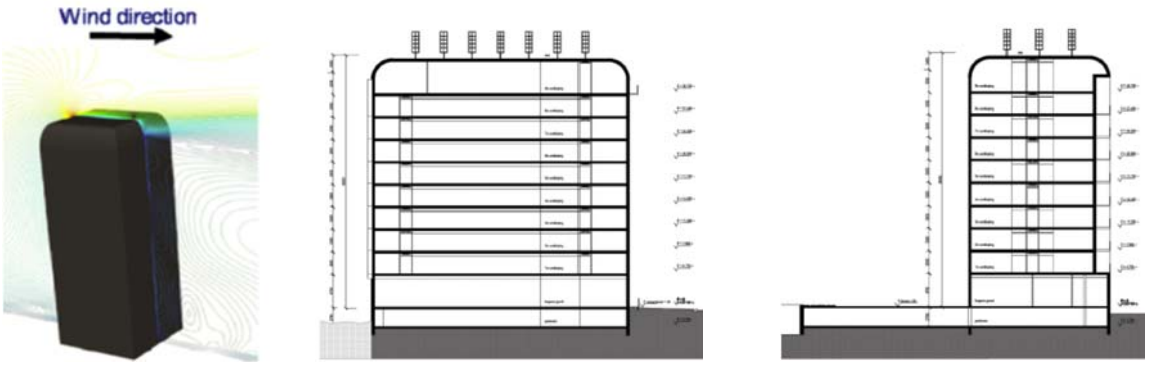

Figure 21b. Left: Sketch of high-rise building with implementation of Powerdak 3.0. Middle and right: Line drawing of Breeze hotel with Powerdak 3.0 (not implemented as such in reality due to current lack of efficient and reliable VAWTs). (Blocken 2016c, Bronsema 2017)

Façade-integrated wind turbines (corners)

Façade-integrated wind turbines (Fig. 22) are inspired by the amplified mean wind speed that can occur around building corners. Nevertheless, when integrated in the corner itself, they can be partly situated in the areas of separated flow or the area of flow stagnation when oriented to the approaching wind. For the other wind directions, they will almost always be situated in the area of separated flow or in the building wake. In addition, often Savonius turbines are used, that are generally characterized by very low power coefficients. Because of these reasons, façade-integrated wind turbines have not been considered in this report.

Figure 22. Parking garage: Greenway Self-Park, 60 W Kinzie St, Chicago, USA (https://www.friedmanproperties.com/portfolio/greenway-self-park)

Façade-integrated wind turbines (open floors or ducts through buildings)
From the study of pedestrian-level wind (PLW) conditions around buildings, it is known that PLW speed can be increased substantially in passages through buildings (Wiren 1975). Such a passage is shown in Fig. 23. This increase in wind speed results from pressure short-circuiting between the overpressure area at the windward façade and the underpressure area at the leeward façade. Similarly, through-passages can be made at larger height above the ground, where the increased wind speed can be used for wind energy harvesting (Fig. 24).

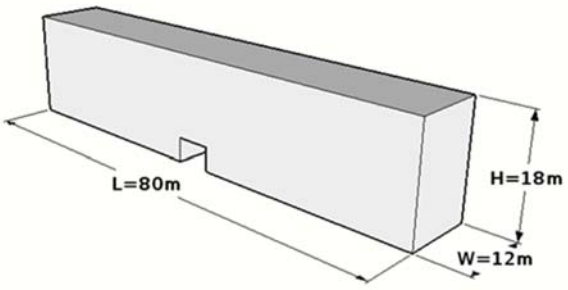

Figure 23. A building with a through-passage

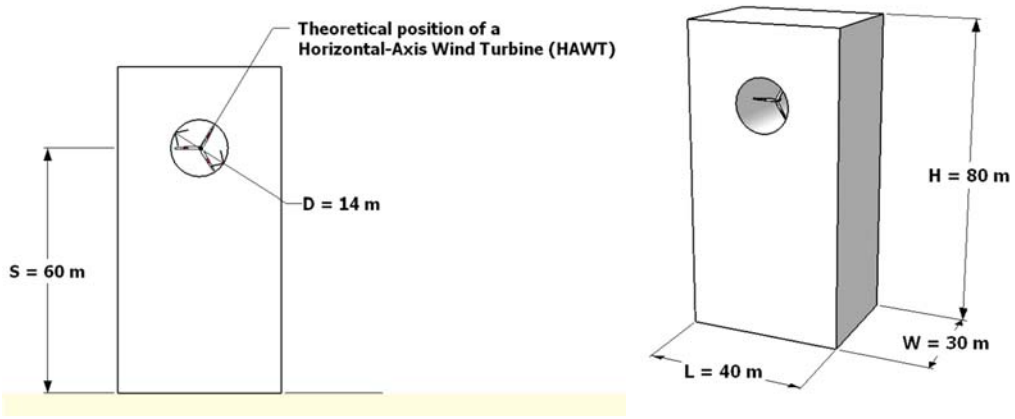

Figure 24. A building with a through-passage at larger height for implementation of a HAWT.

In the study by Alanis Ruiz (2016), various relevant parameters for such an integration were numerically investigated, including building dimensions, wind direction, through-passage diameter and the curvature of the through-passage edges. Especially the latter parameter was shown to be important (Fig. 25). Similar to the Powerdak 3.0 concept, rounded edges can be used to avoid flow separation and to yield a higher and more uniform wind speed in the through-passage, see Fig. 26. As shown in Fig. 26, a sufficient curvature can yield an amplification of mean wind speed up to a factor 1.9, which is substantial and higher as has been achieved in the Powerdak 1.0 concept. Nevertheless, the very substantial intervention required to the original building structure renders the integration of wind turbines in through-passages a less likely alternative for wide implementation. Therefore, although it could be considered for a few specific pilot projects, it has not been considered in the present report to determine the wind energy potential in the Netherlands.

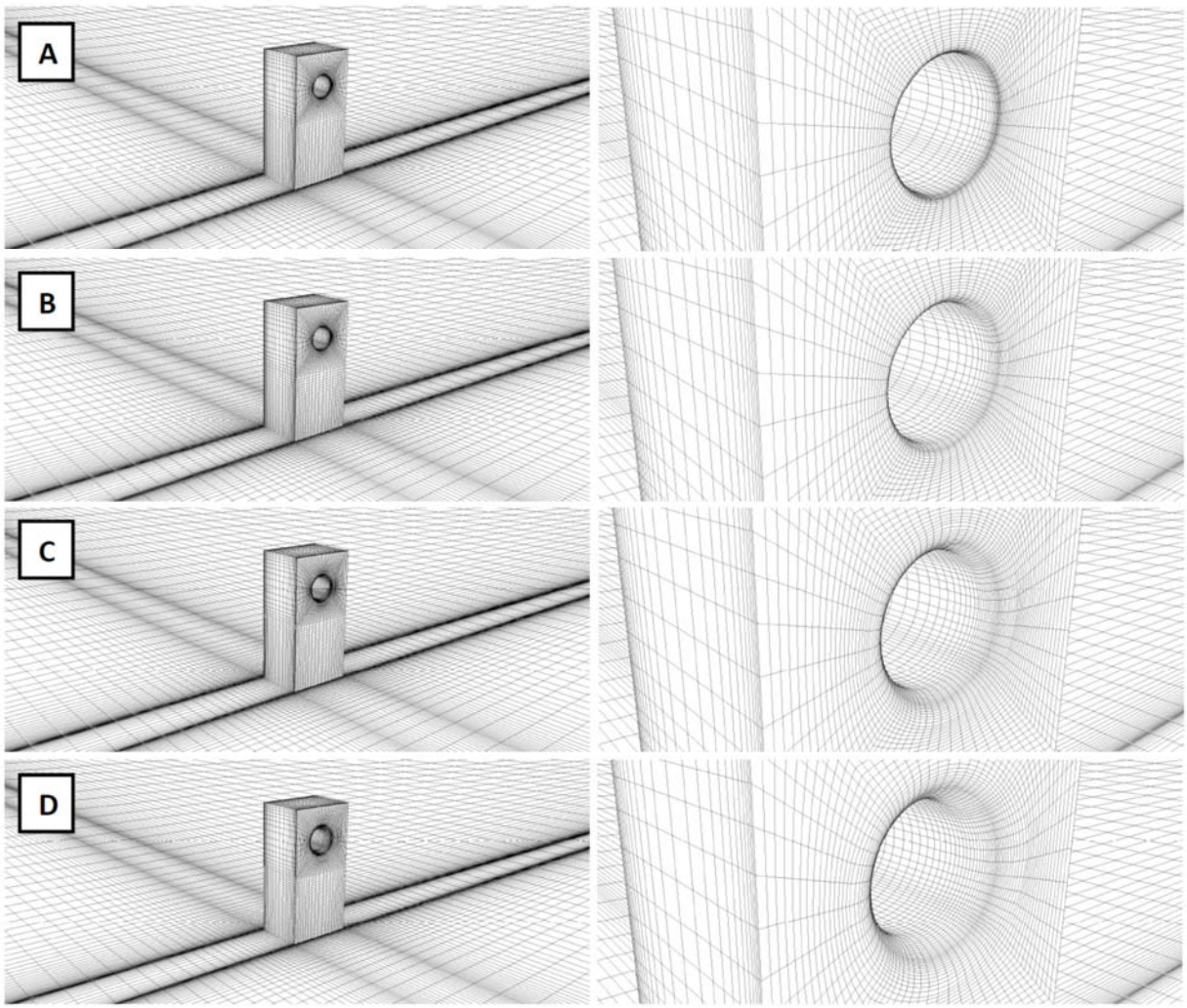

Figure 25. Computational grids for the four different fillet radius configurations: ***A)*** *Case 2-1 with fillet radius r=(1/20)*D=0.7 m;* ***B)*** *Case 2-2 with fillet radius r=(1/10)*D=1.4 m;* ***C)*** *Case 2-3 with fillet radius r=(1/5)*D=2.8 m; and* ***D)*** *Case 2-4 with fillet radius r=(1/3)*D=4.66 m (Alanis Ruiz 2016).*

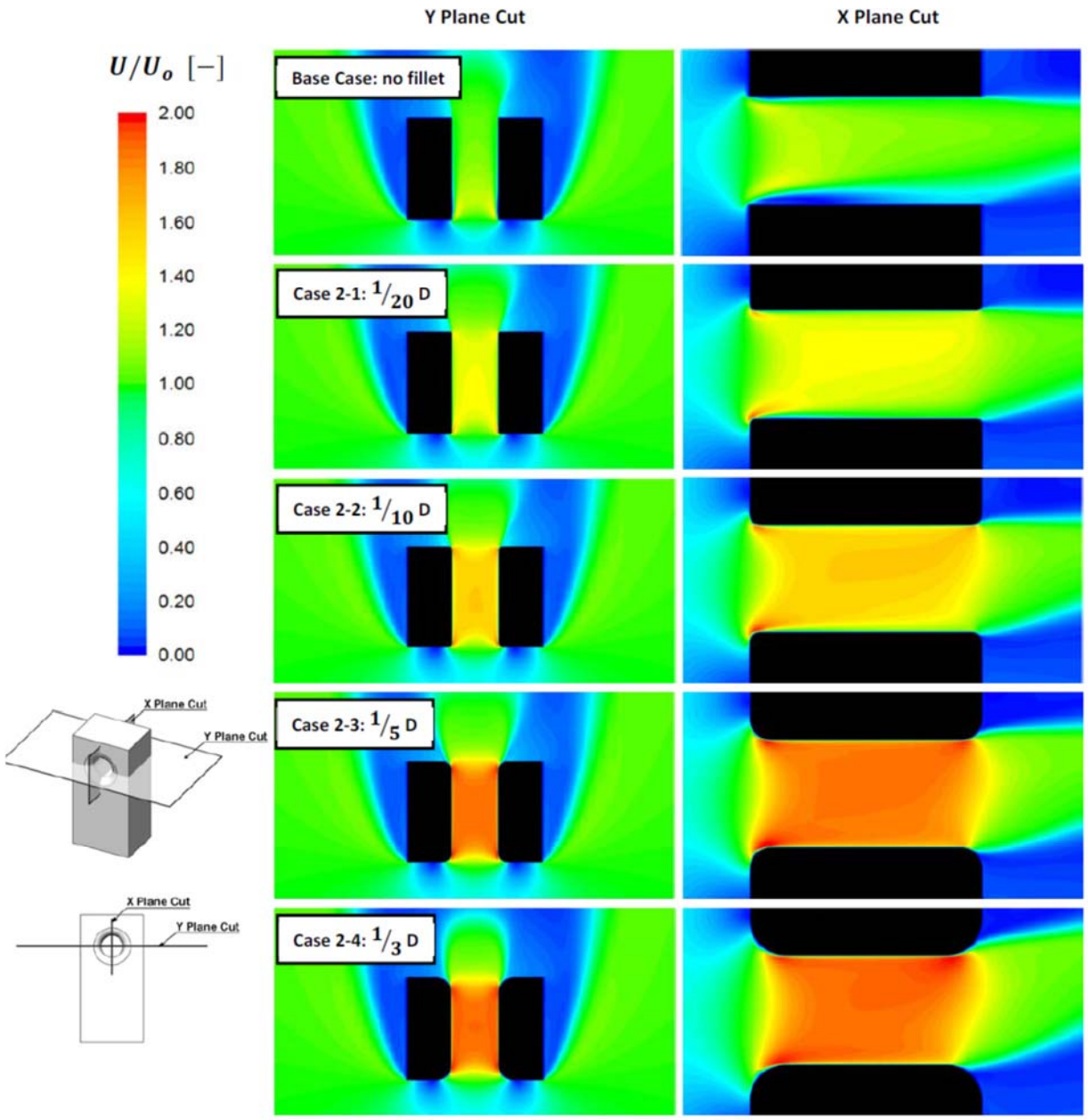

Figure 26. Contours of local wind velocity amplification for the building configurations with different fillet radii at 0° angle of attack (Alanis Ruiz 2016).

Tubular structures with integrated wind turbines

Another alternative is the integration of HAWTs in tubular structures. One of the most recent of these systems carries the name "In-Velox" (Fig. 27, 28). Similar to the roof systems, the philosophy of these systems is to exploit the Venturi effect to increase the wind speed in the tube or channel where generally a HAWT is located in the narrowest section. However, similar to roof-integrated wind turbines, one should carefully balance the increase of wind speed or flow rate through the tube on the one hand, and the increase of flow resistance by the tubular structure itself. A common error made in the evaluation of this type of systems is that the ratio between the wind speed at the

narrowest section of the tube and the wind speed at the inlet of the tube is used to calculate the wind energy potential based on meteorological data. However, due to the large flow resistance, the wind speed at the inlet of the tube will already be much lower than the meteorological wind speed. This misconception can easily lead to unrealistic expectations that cannot be realized in practice. Tubular structures with integrated turbines have not yet seen the same level of detailed and peer-reviewed scientific investigation as roof-integrated turbine systems and therefore further research is necessary to determine their real potential. Nevertheless, given the current lack of precise estimates of the real potential and the associated costs, this system is not included in this report to calculate the wind energy potential of the Netherlands.

Figure 27. Invelox wind energy system in curved channel. (https://financialtribune.com/articles/energy/45861/iran-to-employ-efficient-invelox-wind-turbines)

Figure 28. Invelox wind energy system in a straight channel.
(https://www.deingenieur.nl/artikel/proef-met-windtoeter)

19 Unique position of the Netherlands

As a very knowledge-intensive country in general and with regards to urban aerodynamics and wind energy in particular, the Netherlands have unique position towards the successful implementation of wind energy in the urban environment. The following universities and university research groups have specific expertise in wind energy Note that this is a non-exhaustive list of active groups that is provided below in alphabetical order of institute name:

- Delft University of Technology, Department of Aerospace Engineering, Section Wind Energy (G.J.W. van Bussel e.a.)
- Delft University of Technology, Wind Energy Institute (DUWIND)
- ECN part of TNO (contact W. Boogaard)
- Eindhoven University of Technology, Department of the Built Environment (B. Blocken, M. Hornikx, e.a.)
- Eindhoven University of Technology, Department of Electrical Engineering (J.G. Slootweg e.a.)
- Eindhoven University of Technology, Department of Mathematics and Computer Science (B. Koren e.a.)
- Eindhoven University of Technology, Equipment Prototype Center (E.C.A. Dekkers e.a.)
- University of Twente, Engineering Technology (R. Akkerman, H.W.M. Hoeijmakers e.a.)

Urban wind energy assessment: van Bussel, Blocken e.a.
Aerodynamic analysis of rotor designs: van Bussel, Blocken e.a.
Integration in electrical grid: Slootweg e.a.
Prototype development: Dekkers e.a.
Wind turbine interaction: Koren e.a.
Noise and vibration: Hornikx e.a.
Economical analysis: Boogaard e.a.

In addition, a wide range of manufacturing and consultancy companies with specific expertise in wind turbines and/or components for wind turbines exist. Extreme care should be applied in building consortia with partners that have excellent expertise and past performance in all relevant subfields of (urban) wind energy realization.

References

Alanis Ruiz C, Kalkman I, Blocken B. 2016. Building integrated wind power – wind energy potential in ducted openings through high-rise buildings. MSc thesis Eindhoven University of Technology, Sustainable Energy Technology.

Aslam Bhutta MM, Hayat N, Farooq AU, Ali Z, Jamil SR, and Hussain Z. 2012. Vertical axis wind turbine – A review of various configurations and design techniques. Renewable and Sustainable Energy Reviews, vol. 16 (4), pp. 1926-1939.

Balduzzi F, Bianchini A, Ferrari L. 2012b. Microeolic turbines in the built environment: Influence of the installation site on the potential energy yield. Renew Energ 45:163-174.

Balduzzi F, Bianchini A., Carnevale EA, Ferrari L, Magnani S. 2012a. Feasibility analysis of a Darrieus vertical-axis windturbine installation in the rooftop of a building. Applied Energy 97, 921-9.

Bedon G, Schmidt Paulsen U, Aagaard Madsen H, Belloni F, Raciti Castelli M, and Benini E. 2017. Computational assessment of the DeepWind aerodynamic performance with different blade and airfoil configurations. Applied Energy, vol. 185 (2), pp. 1100-1108.

Beller C. 2009. Urban wind energy – state of the art 2009. Riso DTU National Laboratory of Sustainable Energy, Riso-R-1668(EN).

Blocken B, van Hooff T, Aanen L, Bronsema B. 2011. Computational analysis of the performance of a venturi-shaped roof for natural ventilation: venturi-effect versus wind-blocking effect. Computers & Fluids 48(1): 202-213.

Blocken B, van Hooff T. 2016. Breeze – deel 1: Numeriek onderzoek naar aerodynamische prestaties Powerdak – parameterstudie Powerdak 2.0. Report Eindhoven University of Technology in Breeze project.

Blocken B. 2016a. Breeze – deel 2: Aerodynamische analyse bladprofiel voor verticale-as-windturbine. Report Eindhoven University of Technology in Breeze project.

Blocken B. 2016b. Breeze – deel 3: Schatting van windenergieopbrengsten voor het Powerdak 2.0. Report Eindhoven University of Technology in Breeze project.

Blocken B. 2016c. Breeze – deel 4: Schatting van windenergieopbrengsten voor het Powerdak 3.0. Report Eindhoven University of Technology in Breeze project.

Blocken B. 2016d. Breeze – deel 5: Schatting van windenergieopbrengsten voor het hotel met Powerdak 3.0. Report Eindhoven University of Technology in Breeze project.

Borg M and Collu M. 2015. Frequency-domain characteristics of aerodynamic loads of offshore floating vertical axis wind turbines. Applied Energy, vol. 155, pp. 629-636.

Borg M, Shires A, and Collu M. 2014. Offshore floating vertical axis wind turbines, dynamics modelling state of the art. Part I: aerodynamics. Renewable and Sustainable Energy Reviews, vol. 39, pp. 1214-1225.

Bronsema B. 2005. Earth, Wind & Fire – Towards new concepts for climate control in buildings. CIB W096 Meeting Lyngby, November 2-4 2005.

Bronsema B. 2010. Earth, Wind & Fire – Air-conditioning powered by nature. 10th REHVA World Congress CLIMA 2010, 9-12 May, Antalya, Turkey, 2010

Bronsema B. 2013. Earth, Wind & Fire – Natuurlijke Airconditioning. PhD thesis Delft University of Technology. Uitgeverij Eburon, Delft, the Netherlands. ISBN 978 90- 5972 762 5.

Bronsema B. 2017. Windenergie voor Hotel Breeze - Verslag activiteiten 2014/2015 en voorstel vervolgonderzoek.

Campbell NS, Stankovic S. 2001. Wind energy for the Built environment–Project WEB, A report for Joule III Contract No JOR3-CT98-01270.
Chen W-H, Chen C-Y, Huang C-Y, and Hwang C-J. 2017. Power output analysis and optimization of two straight-bladed vertical-axis wind turbines. Applied Energy, vol. 185, pp. 223-232.
Dabiri JO. 2011. Potential order-of-magnitude enhancement of wind farm power density via counter-rotating vertical-axis wind turbine arrays. Journal of Renewable and Sustainable Energy, vol. 3 (4), p. 043104, 2011. doi:10.1063/1.3608170
Dabiri JO. 2014. Emergent aerodynamics in wind farms," Physics Today, vol. 67 (10), pp. 66-67. doi:10.1063/pt.3.2559
Grant A, Johnstone C, Kelly N. 2008. Urban wind energy conversion: the potential of ducted turbines. Renew Energ 33(6): 157–1163.
Grunwald A, Melsheimer M, Heilmann C, Twele J, Amme J, and Pieniak N. 2013. Reducing vibration issues at small vertical-axis wind turbines on buildings. In Europe's Premier Wind Energy Event (EWEA2013), Vienna, Austria.
Islam MR, Mekhilef S, and Saidur R. 2013. Progress and recent trends of wind energy technology. Renewable and Sustainable Energy Reviews, vol. 21, pp. 456-468, 2013.
King G, Roland-Mieszkowski M, Jason T, and Rainham DG. 2012. Noise levels associated with urban land use. Journal of Urban Health, vol. 89 (6), pp. 1017-1030.
Leishman JG. 2002. Challenges in modelling the unsteady aerodynamics of wind turbines. Wind Energy, vol. 5 (2-3), pp. 85-132.
Lu L, Ip KY. 2009. Investigation on the feasibility and enhancement methods of wind power utilization in high- rise buildings of Hong Kong, Renew Sust Energ Rev 13:450-461.
Mertens S. 2006. Wind energy in the built environment. Brentwood (UK): Multi-Science.
Mithraratne N. 2009. Roof-top wind turbines for microgeneration in urban houses in New Zealand. Energ Buildings 41: 1013–1018.
Müller G., Jentsch M.F., Stoddart E. 2009. Vertical axis resistance type wind turbines for use in buildings. Renewable Energy, 34 (5), 1407-1412.
NREL. 2017. Wind energy review in 2016.
Park JH, Chung MH, and Park JC. 2016. Development of a small wind power system with an integrated exhaust air duct in high-rise residential buildings. Energy and Buildings, vol. 122, pp. 202-210.
Paulsen US, Madsen HA, Kragh KA, Nielsen PH, Baran I, Hattel J, Ritchie E, Leban K, Svendsen H, and Berthelsen PA. 2014. DeepWind-from idea to 5 MW concept. Energy Procedia, vol. 53, pp. 23-33.
Peacock AD, Jenkins D, Ahadzi M, Berry A, Turan S. 2008. Micro wind turbines in the UK domestic sector, Energ Buildings 40 (7):1324–1333.
Rezaeian M, Montazeri H, and Loonen R. 2017. Science foresight using life-cycle analysis, text mining and clustering: a case study on natural ventilation. Technological Forecasting & Social Change, vol. 118 (C), pp. 270-280.
Rezaeiha A, Pereira R, and Kotsonis M. 2017a. Fluctuations of angle of attack and lift coefficient and the resultant fatigue loads for a large horizontal axis wind turbine. Renewable Energy, vol. 114 (B), pp. 904-916.
Rezaeiha A, Kalkman I, and Blocken B,. 2017b. Effect of pitch angle on power performance and aerodynamics of a vertical axis wind turbine. Applied Energy, vol. 197, pp. 132-150.
Rezaeiha A, Kalkman I, and Blocken B. 2017c. CFD simulation of a vertical axis wind turbine operating at a moderate tip speed ratio: guidelines for minimum domain size and azimuthal increment. Renewable Energy, vol. 107, pp. 373-385.
Rezaeiha A, Kalkman I, Montazeri H, and Blocken B. 2017d. Effect of the shaft on the aerodynamic performance of urban vertical axis wind turbines. Energy Conversion and Management, vol. 149 (C), pp. 616-630.
Rezaeiha A, Montazeri H, Blocken B. 2018a. Towards accurate CFD simulations of vertical axis wind turbines at different tip speed ratos and solidities: guidelines for azimuthal increment, domain size and convergence. Energy Conversion and Management 156: 301-316.

Rezaeiha A, Montazeri H, and Blocken B. 2018b. Characterization of aerodynamic performance of vertical axis wind turbines: impact of operational parameters. Energy Conversion and Management.

Sharpe T, Proven G. 2010. Crossflex: concept and early development of a true building integrated wind turbine. Energ Buildings 42 (12):2365–2375.

Simão Ferreira C and Scheurich F. 2014. Demonstrating that power and instantaneous loads are decoupled in a vertical-axis wind turbine. Wind Energy, vol. 17 (3), pp. 385-396.

Sunderland K, Woolmington T, Blackledge J, and Conlon M. 2013. Small wind turbines in turbulent (urban) environments: A consideration of normal and Weibull distributions for power prediction. Journal of Wind Engineering and Industrial Aerodynamics 121: 70-81, 2013.

Toja-Silva F, Colmenar-Santos A, and Castro-Gil M. 2013. Urban wind energy exploitation systems: behaviour under multidirectional flow conditions—opportunities and challenges. Renewable and Sustainable Energy Reviews, vol. 24, pp. 364-378.

Tummala A, Velamati RK, Sinha DK, Indraja V, and Krishna VH. 2016. A review on small scale wind turbines. Renewable and Sustainable Energy Reviews, vol. 56, pp. 1351-1371.

van Hooff T, Blocken B, Aanen L, Bronsema B. 2011. A venturi-shaped roof for wind-induced natural ventilation of buildings: wind tunnel and CFD evaluation of different design configurations. Building and Environment 46(9): 1797-1807.

van Hooff T, Blocken B, Aanen L, Bronsema B. 2012. Numerical analysis of the performance of a venturi-shaped roof for natural ventilation: influence of building width. Journal of Wind Engineering and Industrial Aerodynamics 104-106: 419-427.

Wiren B. 1975. A wind tunnel study study of wind velocities in passages between and through buildings. Heathrow, Cambridge University Press, pp. 465 - 475.

World Wind Energy Association. 2017. Small wind world report. World Wind Energy Association (WWEA), Germany, 2017.

Yang A-S, Su Y-M, Wen C-Y, Juan Y-H, Wang W-S, and Cheng C-H. 2016. Estimation of wind power generation in dense urban area. Applied Energy, vol. 171, pp. 213-230.

van Hooff T, Blocken B, Aanen L, Bronsema B. 2011. A venturi-shaped roof for wind-induced natural ventilation of buildings: wind tunnel and CFD evaluation of different design configurations. ***Building and Environment*** *46(9): 1797-1807.*

2011 Best Paper Award from Building and Environment

A venturi-shaped roof for wind-induced natural ventilation of buildings: wind tunnel and CFD evaluation of different design configurations

T. van Hooff [(a,b)], B. Blocken * [(a)] , L. Aanen [(c)] , B. Bronsema [(d)]

(a) Building Physics and Systems, Eindhoven University of Technology, P.O. box 513, 5600 MB Eindhoven, the Netherlands
(b) Division of Building Physics, Department of Civil Engineering, Katholieke Universiteit Leuven, Kasteelpark Arenberg 40, P.O. Box 2447, 3001 Leuven, Belgium
(c) Peutz BV, P.O. box 66, 6585 ZH, Mook, The Netherlands
(d) Faculty of Architecture – Department of Climate Design, Delft University of Technology, Prof. Boerhaaveweg 37, 2251 HX Voorschoten, The Netherlands

Graphical abstract:

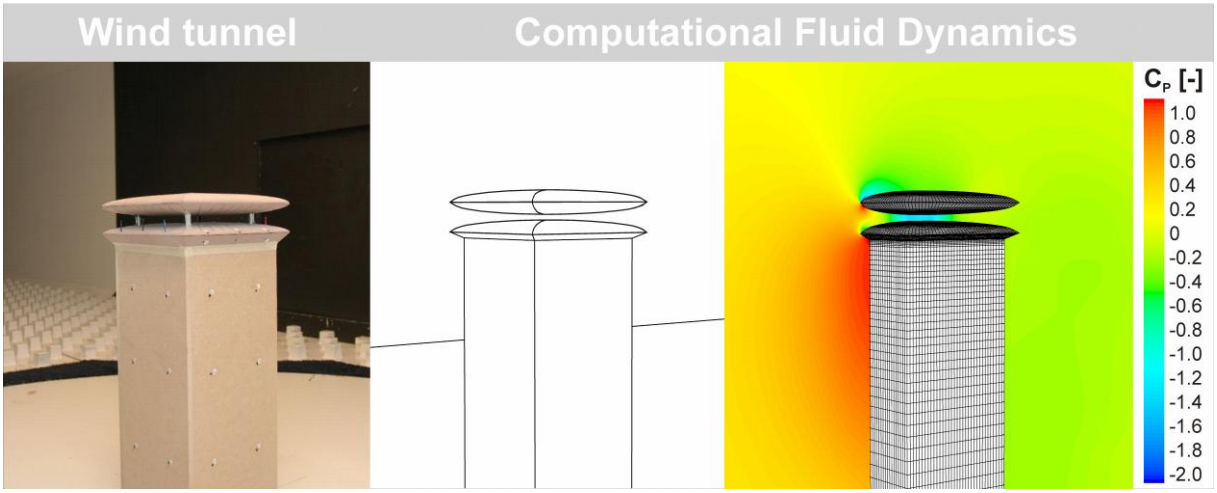

Highlights:

► Detailed experimental and numerical analysis of aerodynamic performance.
► Roof design without guiding vanes yields large underpressure in roof.
► Roof design with guiding vanes does not yield large underpressure in roof.
► Counter-intuitive result: guiding vanes do not improve but reduce aerodynamic performance.
► Reason: wind-blocking effect dominates venturi-effect when guiding vanes are present.

* **Corresponding author**: Bert Blocken, Building Physics and Systems, Eindhoven University of Technology, P.O.Box 513, 5600 MB Eindhoven, the Netherlands. Tel.: +31 (0)40 247 2138, Fax +31 (0)40 243 8595
E-mail address: b.j.e.blocken@tue.nl

van Hooff T, Blocken B, Aanen L, Bronsema B. 2011. A venturi-shaped roof for wind-induced natural ventilation of buildings: wind tunnel and CFD evaluation of different design configurations. ***Building and Environment*** *46(9): 1797-1807.*

2011 Best Paper Award from Building and Environment

A venturi-shaped roof for wind-induced natural ventilation of buildings: wind tunnel and CFD evaluation of different design configurations

T. van Hooff [(a,b)], B. Blocken * [(a)] , L. Aanen [(c)] , B. Bronsema [(d)]

(a) Building Physics and Systems, Eindhoven University of Technology, P.O. box 513, 5600 MB Eindhoven, the Netherlands
(b) Division of Building Physics, Department of Civil Engineering, Katholieke Universiteit Leuven, Kasteelpark Arenberg 40, P.O. Box 2447, 3001 Leuven, Belgium
(c) Peutz BV, P.O. box 66, 6585 ZH, Mook, The Netherlands
(d) Faculty of Architecture – Department of Climate Design, Delft University of Technology, Prof. Boerhaaveweg 37, 2251 HX Voorschoten, The Netherlands

Abstract
Wind tunnel experiments and Computational Fluid Dynamics (CFD) are used to analyse the flow conditions in a venturi-shaped roof, with focus on the underpressure in the narrowest roof section (contraction). This underpressure can be used to partly or completely drive the natural ventilation of the building zones. The wind tunnel experiments are performed in an atmospheric boundary layer wind tunnel at scale 1:100. The 3D CFD simulations are performed with steady RANS and the RNG k-ε model. The purpose of this study is twofold: (1) to evaluate the accuracy of steady RANS and the RNG k-ε model for this application and (2) to assess the magnitude of the underpressures generated with different design configurations of the venturi-shaped roof. The CFD simulations of mean wind speed and surface pressures inside the roof are generally in good agreement (10-20%) with the wind tunnel measurements. The study shows that for the configuration without guiding vanes, large negative pressure coefficients are obtained, down to -1.35, with reference to the free-stream wind speed at roof height. The comparison of design configurations with and without guiding vanes shows an – at least at first sight – counter-intuitive result: adding guiding vanes strongly decreases the absolute value of the underpressure. The reason is that the presence of the guiding vanes increases the flow resistance inside the roof and causes more wind to flow over and around the roof, and less wind through it (wind-blocking). As a result, the optimum configuration is the one without guiding vanes.

Keywords: Computational Fluid Dynamics (CFD); sustainable building; natural ventilation; energy efficiency; venturi-effect; airflow

1. Introduction

Natural ventilation is a sustainable approach to achieve a healthy and comfortable indoor environment in buildings. One of the most important influencing parameters concerning the feasibility of natural ventilation of buildings is the geometry of the building itself. In the past, several studies have been conducted to improve the natural ventilation of a building by modifying the building facades (e.g. wind floors, double-skin facades) or by adding structures on the roof of a building (e.g. wind towers, wind catchers). An overview of wind-driven ventilation techniques is provided by Khan et al. [1]. The present study consists of the analysis of the aerodynamic performance of a venturi-shaped roof that was designed by Bronsema as part of the research project "Earth, Wind & Fire – Air-conditioning powered by Nature" [2] (Fig. 1). The roof consists of a disk-shaped roof construction that is positioned at a certain height above the actual building, creating a contraction that is expected

* **Corresponding author**: Bert Blocken, Building Physics and Systems, Eindhoven University of Technology, P.O.Box 513, 5600 MB Eindhoven, the Netherlands. Tel.: +31 (0)40 247 2138, Fax +31 (0)40 243 8595
E-mail address: b.j.e.blocken@tue.nl

to provide significant negative pressures that can be used to partly or completely drive the natural ventilation of the building.

Analysis of natural ventilation of buildings can be performed using a wide range of methods [3], including: (1) reduced-scale water tank experiments (e.g. [4-6]); (2) analytical and/or semi-empirical formulae (e.g. [4,7-9]); (3) full-scale measurements (e.g. [10-13]); (4) reduced-scale atmospheric boundary layer wind tunnel experiments (e.g. [14-17]); and (5) numerical simulation with Computational Fluid Dynamics (CFD) (e.g. [6,10,13,14,18-20]). Water tank experiments and analytical formulae have generally been applied for simplified configurations and have proved very valuable to gain insight in the process of natural ventilation, such as the combined effects of wind and buoyancy as driving forces (e.g. [5,7]). They are however less suitable for practical applications for specific buildings in specific environments. For such applications, full-scale measurements are very valuable but they are generally time-consuming and expensive and the boundary conditions are often uncontrollable. In addition, full-scale measurements are not an option in the design phase of buildings. Wind tunnel experiments allow much better control of the boundary conditions. However, they strictly need to be performed in an atmospheric boundary layer wind tunnel, with a sufficiently long upstream fetch to establish appropriate atmospheric boundary layer profiles. Additionally, scaling of the model geometry can be a problem, especially for small openings in which, when scaled down, the Re numbers can drop below the threshold for fully turbulent flow. In that case – among others – CFD is an interesting option [13]. CFD has the advantage that it allows full control over the boundary conditions, that it provides data in every point of the domain simultaneously ("whole-flow field data") and that it does not suffer from scaling limitations because simulations can be performed at full scale. It also allows efficient parametric analysis of different design configurations (e.g. [13]). However, the accuracy of CFD is an important concern and solution verification and validation studies are imperative [21].

In this paper, the aerodynamic performance of the venturi-shaped roof concept is analysed by a combination of wind tunnel measurements and CFD simulations. The purpose of the study is twofold: (1) to evaluate the accuracy of steady RANS CFD and the RNG k-ε model for this application and (2) to assess the magnitude of the underpressures in the contraction and to compare the performance of different design configurations. Three different wind roof configurations are assessed in terms of the negative pressure at position E in the contraction (see Fig. 1). Note that the concept of the wind roof design to some extent resembles that of the wind floor that has been applied in the Liberty Tower of Meiji University in Japan [22] and the wind roof of GSW headquarters in Berlin, Germany [23] to increase the natural ventilation of high-rise buildings.

First, the building and roof geometry are described. Next, the wind tunnel measurements are outlined, followed by the CFD simulations. Finally, the results of the wind tunnel measurements and CFD simulations will be presented and compared, and topics for future work will be discussed.

2. Description of building and roof geometry

The study is conducted for a rectangular (20 m x 20 m) building with a height of 50 m, measured up to the edge of the roof (Fig. 1a). The venturi-shaped roof consists of two parts. The lower part is constructed from half a "square disk" with dimensions 23.4 m x 23.4 m x 2 m (L x W x H) and it is positioned directly on top of the building, this way creating a roof overhang of 1.7 m on each side of the building, at which ventilation inlets will be placed. At a distance 'c' above this part of the roof a full "square disk" is positioned with dimensions 23.4 m x 23.4 m x 4 m (L x W x H), resulting in a nozzle-shaped roof entrance from all four sides of the building. This part can be supported by e.g. a set of slender vertical columns or by the guiding vanes, which will be discussed further. In this study, the distances 'b' and 'c' in Fig. 1 are taken equal to 5 m and 1 m, respectively, yielding a contraction ratio of 5. 'c' is the height of the narrowest part of roof contraction. The position of interest inside the roof is indicated with the letter E (from "exhaust") in Figure 1a and b. In this study, the exhaust is considered to be closed and the surface pressure at this position will be evaluated. A reasonable expectation is that at this position, the flow speed will have increased due to the decrease of the cross-sectional area of the contraction, which will locally yield increased negative pressures. While this could be called "venturi-effect", it is important to note that strictly, the term venturi-effect refers to confined flows, while in the case of this roof, the air can also flow over and around the roof, rather than only through it. It will therefore generally not be true that the flow speed in the contraction is inversely proportional to the cross-sectional area, as it would be in a confined flow. This discussion is similar to the one for wind flow in passages between parallel buildings [24] and for wind flow in passages between buildings in converging and diverging arrangement [25,26]. In the present study, we will use the term "venturi-effect" to refer to the expected increase of flow speed and underpressure, in spite of the non-confined flow conditions.

In an attempt to enhance the venturi-effect, guiding vanes could be added between the lower part and the upper part of the roof opening. Two configurations of guiding vanes are studied: (a) 4 guiding vanes (one at every 90° interval), or (b) 36 guiding vanes (one at every 10° interval) (Fig. 1b). For both configurations, the

resulting opening 'f' in the centre of the roof has dimensions 2 x 2 m^2 (L x W) (see Fig. 1). Overall, three configurations are studied in detail (Fig. 2):

- Configuration A: venturi-shaped roof without guiding vanes;
- Configuration B: venturi-shaped roof with guiding vanes every 90°;
- Configuration C: venturi-shaped roof with guiding vanes every 10°.

In addition, a fourth configuration (D) is briefly included, to serve as a reference case. It is the same building but without venturi-shaped roof (i.e. only half a "square disk" and no "full" square disk above it). All experiments and simulations are conducted for an isolated building, i.e. without surrounding buildings. Therefore, all differences in velocities and surface pressures between the different configurations are only due to changes in the wind roof design.

3. Wind tunnel measurements

A reduced-scale model (1:100) of the building with venturi-shaped roof is constructed and placed in the closed-circuit atmospheric boundary layer (ABL) wind tunnel (Fig. 3) at Peutz BV in Mook, the Netherlands. The dimensions of the test section are 3.2 x 1.8 m^2 (W x H), resulting in a blockage ratio of about 2%. The building model was placed on a turntable with a diameter of 2.3 m. The measurement positions on the building and roof surfaces and in the roof are schematically indicated in Figure 4. Surface pressures are measured at 24 positions on the four vertical facades, at 8 positions on the inclined facade parts (ventilation inlets) and at 26 positions in the roof contraction. The measurements are performed with HCLA12X5EB amplified differential pressure sensors from Sensortechnics. Wind speed is measured at 7 positions inside the roof contraction using NTC resistor elements. All wind speed measurements are made at mid-height in the contraction. The NTCs are operated with a constant current and are calibrated by Peutz by determining the relationship between wind speed and temperature (and corresponding resistance) of each individual probe. The probes are not direction-sensitive and due to the relatively long reaction time of the probes, only average wind speeds can be measured, with an accuracy of ±10%. Approach-flow vertical profiles of mean wind speed U and turbulence intensity I_u are measured at the edge of the turntable using hot-wire anemometers and are presented in Figure 5. The measured wind speed profile can be described by a logarithmic law with a friction velocity $u^* = 0.956$ m/s and an aerodynamic roughness length $y_0 = 0.005$ m (full scale: $y_0 = 0.5$ m). The incident reference wind speed at roof height (0.5 m) is 10.5 m/s. Measurements are made for four wind directions: $\varphi = 0°$, 15°, 30° and 45°, taking into account the symmetry of the building and the building roof.

4. CFD simulations: computational model and computational parameters

4.1. Computational geometry and grid

A computational model was made of the reduced-scale building model used for the wind tunnel measurements. The same scale was used for validation purposes. The computational domain has dimensions L x B x H = 10.2 m x 10.2 m x 3 m (Fig. 6a). This domain shape allows modelling different wind directions (0° to 45°). A lot of effort has been devoted to construct high-quality and high-resolution computational grids (Fig. 6b and Fig. 7). The grids have at least 10 cells between each two adjacent surfaces, such as the guiding vanes, as requested by the best practice guidelines by Franke et al. [27] and Tominaga et al. [28]. The grids are made using the grid generation technique presented by van Hooff and Blocken [13]. In this technique, the geometry and the grid are created simultaneously, by a series of extrusion operations. This procedure allows a large degree of control over the size and shape of the cells, and therefore of the quality and resolution of the computational grid. It allows high-quality grids to be made, even for rather complex geometries. The same technique has been used successfully on previous occasions to model sport stadium geometries [13,20,29]. The four grids are block-structured and consist of 2.0 million, 2.4 million, 3.3 million and 1.8 million hexahedral cells for configurations A, B, C and D, respectively. Note that the grids do not contain any pyramidal or tetrahedral cells. Special attention was paid to the detailed reproduction and meshing of the wind roof geometry. A high grid resolution is applied in the proximity of the roof in view of the expected large flow gradients. A detailed grid-sensitivity analysis was performed indicating that the grids shown in Figure 7 provide nearly grid-independent results. The grid-sensitivity analysis will be reported in section 5.1.

4.2. Boundary conditions

At the inlet of the domain the measured approach-flow mean wind speed profile is imposed. Turbulent kinetic energy k is calculated from the turbulence intensity I_u using $k = 0.5(I_u.U)^2$. The turbulence dissipation rate $\varepsilon = (u^*)^3/\kappa(y+y_0)$, where y is the height coordinate, κ the von Karman constant ($\kappa = 0.42$) and u* the friction velocity related to the logarithmic mean wind speed profile. At the ground and building surfaces, the standard

wall functions by Launder and Spalding [30] are used with the sand-grain based roughness modification by Cebeci and Bradshaw [31]. For the ground surface, the parameters k_S and C_S, to be used in Fluent [32], should be selected to correctly represent the rough fetch upstream of the building model (see Fig. 3a). This type of consistent atmospheric boundary layer simulation is very important to obtain accurate simulation results [24,33]. Therefore, k_S and C_S have to be determined using their appropriate consistency relationship with y_0. This relationship was derived by Blocken et al. [33] for Fluent and CFX. For Fluent 6, up to at least version 6.3, it is given by $k_S = 9.793y_0/C_S$. The combination $k_S = 0.0098$ m and $C_S = 5$ m is selected. The building surfaces are assumed to be smooth ($k_S = 0$ m and $C_S = 0.5$). Zero static pressure is imposed at the outlet of the domain and the top of the domain is modeled as a slip wall (zero normal velocity and zero normal gradients of all variables).

4.3. Solver settings

The 3D Reynolds-averaged Navier-Stokes (RANS) equations are solved in combination with the Renormalisation Group (RNG) k-ε turbulence model [34], using Fluent 6.3.26. The RNG k-ε turbulence model was chosen for this study because of its good performance in predicting the surface pressures on the windward building facades and in the roof opening in a preliminary study, and because of its superior performance in an earlier study by Evola and Popov [35]. Pressure-velocity coupling is taken care of by the SIMPLE algorithm, pressure interpolation is standard and second-order discretization schemes are used for both the convection terms and the viscous terms of the governing equations. Convergence has been monitored carefully and the iterations have been terminated when all residuals showed no further reduction with increasing number of iterations. At this stage, the scaled residuals were: 10^{-4} for continuity, 10^{-7} for momentum, 10^{-6} for turbulent kinetic energy and 10^{-4} for turbulence dissipation rate.

5. Results

5.1. Grid-sensitivity analysis

To reduce numerical errors, not only iterative convergence but also grid convergence should be assessed. In this study, a grid-sensitivity analysis was performed by constructing two additional grids for the configurations A and C: a coarser grid and a finer grid. Coarsening and refining was performed with an overall linear factor $\sqrt{2}$. The model for configuration A (no guiding vanes) has 549,380 cells for the coarse grid, 2,041,268 cells for the middle grid and 4,364,688 cells for the fine grid. The model for configuration C (guiding vanes every 10°) has 2,040644 cells for the coarse grid, 3,250,032 cells for the middle grid and 7,107,648 cells for the fine grid. The resulting grids for configuration A are shown in Fig. 8a. The results on the three grids are compared in terms of the mean wind speed along a vertical line in the centre of the roof contraction (Fig. 8b), indicating only a very limited dependence of the results on the grid resolution. The results on the three grids are also compared in terms of the absolute values of the pressure coefficients at the windward building facade and in the centre of the roof contraction (Fig. 8c-d). Note that the pressure coefficients are computed as $C_p = (P-P_0)/(0.5\rho U_{ref}^2)$ with P the static pressure at the surface, P_0 the reference static pressure, $\rho = 1.225$ kg/m³ the air density and U_{ref} the reference wind speed at roof height ($U_{ref} = 10.5$ m/s at $y = 0.5$ m). A small deviation (7 %) is found between the coarse and middle grid for the C_p at position E, while almost no deviation is found for the value of this parameter between the middle grid and the fine grid. Similar results are obtained for configuration C. Therefore, the middle grids (i.e. those shown in Fig. 7) are retained for further analysis.

5.2. Model-scale versus full-scale CFD simulations

Most CFD simulations presented in this paper have been performed at model scale (i.e. wind tunnel scale). To assess their validity in reality, i.e. at full scale, some simulations at full scale have been conducted. The results from both sets are compared in Figure 9, for the configuration without guiding vanes and the configuration with guiding vanes every 10°. The differences between the values of the mean underpressure and the mean wind speed in the centre of the roof contraction are very limited. Only for C_p and configuration C, the difference is about 10%. The model scale Reynolds numbers are 10400 and 6850 for configurations A and C, respectively. Apparently, these numbers are large enough to provide a sufficient degree of Reynolds number independence.

5.3. Comparison of CFD and wind tunnel results

The presentation of the CFD and wind tunnel results and their comparison is performed in three parts. First, the pressure coefficients at the windward vertical facades and at the windward inclined facade parts are

presented. Next, the wind speed ratio U/U_{ref} at mid-height in the centre of the roof contraction is shown. Finally, the pressure coefficients at position E in the centre of the roof contraction are displayed.

Figure 10 compares the numerically simulated and measured pressure coefficients at the windward facades of the configurations A, B and C and for the four wind directions: $\varphi = 0°$, 15°, 30°, and 45°. Only the windward facades are considered, because it is known that steady RANS CFD is deficient in reproducing the wind flow downstream of windward facades [36,37]. This deficiency is considered less important for the present study, because the actual focus is on the flow conditions inside the roof contraction. For the windward facades, the general agreement is quite good, although there seems to be a systematic overestimation of the measurement values by the CFD results, by about 10%. Possible reasons for this are the performance of the RNG model and/or streamwise gradients in the approach-flow mean wind speed and turbulence intensity profile due to the smooth turntable. Note that the smooth part of the turntable, between the roughness elements and the position of the building model, was modelled as a rough surface in CFD, while it is actually not covered by roughness elements in the experiment. Therefore, in the wind tunnel, horizontally inhomogeneous profiles are present, which can affect the accuracy of the results.

Fig. 11 compares the numerically simulated and measured mean wind speed ratios U/U_{ref} at mid-height in the centre of the roof contraction, for the three roof configurations and for the four wind directions. The deviations are generally smaller than 10%, which is considered a very close agreement. Note that the CFD results all slightly underestimate the mean wind speed ratio compared to the wind tunnel results.

Fig. 12 compares the numerically simulated and measured pressure coefficients C_p at position E in the centre of the roof contraction. For $\varphi = 0°$ and $\varphi = 15°$, the CFD results and the wind tunnel results are in fairly good agreement. The agreement however deteriorates for the more oblique wind directions, $\varphi = 30°$ and 45°. The reasons are (1) the specific geometry of the roof, with four "ribs" on the roof surfaces (see e.g. Fig. 1 and 2); (2) the flow separation at the vanes, which is more pronounced for the oblique wind directions; and (3) the large C_p gradients at the roof surfaces. In spite of these deviations between the numerical and the measured C_p values, the trends are clear and allow a comparison of the performance of the different roof configurations.

5.4. Comparison of roof configurations

Fig. 10 shows that there are no clear differences between the different roof configurations in terms of C_p on the windward vertical and inclined facade parts. On the other hand, very clear differences are found for the wind speed ratio U/U_{ref} in Fig. 11. The ratio for the configuration without guiding vanes is about 50% higher than with guiding vanes. The configuration with guiding vanes every 90° only provides a slightly higher wind speed ratio than the one with guiding vanes every 10°. The parameter that is of most interest however is the pressure coefficient at the intended exhaust opening E, i.e. at the bottom centre of the roof contraction. Fig. 12 shows that a strong negative pressure coefficient is obtained for the configuration without guiding vanes: the numerically simulated C_p value ranges between -1.05 and -1.33, while the measured C_p value ranges between -1.20 and -1.35. For the configurations with guiding vanes however, much less negative C_p values obtained, which are at best (i.e. for $\varphi = 0°$) only about 30% of those for the configuration without guiding vanes. For $\varphi = 15°$, the values drop to less than 25% of those without guiding vanes. And for $\varphi = 30°$ and 45°, the values either drop even further, or become positive. Both the numerical and the experimental results show the superior performance of the configuration without guiding vanes.

6. Discussion

The discussion focuses on three issues: (1) the calculation of the approach-flow turbulent kinetic energy profile from the measured turbulence intensity; (2) the reasons for the superior performance of the roof configuration without guiding vanes; and (3) the limitations of the present study.

The approach-flow turbulent kinetic energy k was calculated from the measured turbulence intensity I_u using the equation $k = 0.5(I_u.U)^2$. The reason for this is that I_u is the turbulence intensity measured by a single horizontally oriented hot wire. It therefore not only includes the contribution by the streamwise turbulent fluctuations but also part of the vertical turbulent fluctuations. When I_u would be the streamwise turbulence intensity only, the equation $k = (I_u.U)^2$ would probably have been more appropriate [28]. Nevertheless, the calculation of k from I_u in the present study is a source of uncertainty. Therefore, the effect of using different equations to calculate k from I_u on the calculated wind speed ratio U/U_{ref} and on the underpressure at position E was assessed, for configuration A. The effect on the ratio U/U_{ref} is less than 1% and therefore considered insignificant. The effect on the underpressure coefficient however is larger: for $k = 0.5(I_u.U)^2$, $C_p = -1.21$; for $k = (I_u.U)^2$, $C_p = -1.30$; for $k = 1.5(I_u.U)^2$, $C_p = -1.35$. Note however that $k = 0.5(I_u.U)^2$ is considered the best choice for the present study, and that the related uncertainty does not compromise the conclusions of the study.

Both the numerical and the experimental results show the – at least at first sight – counter-intuitive result that the configuration without guiding vanes yields a much larger underpressure in the centre of the roof contraction

than the configurations with guiding vanes. Note that the intention of adding guiding vanes was to increase the magnitude of the underpressure, but that their presence actually has the opposite effect. The reason for this is twofold. First, while it could be expected that the guiding vanes provide a smoother conduction of the flow through the roof contraction, they actually represent multiple locations of flow separation, which is associated with momentum losses and flow speed reduction. Second, and more importantly, the presence of guiding vanes adds a considerable resistance to the flow through the roof contraction. This way, the wind flow that approaches the building roof will for a larger part flow over and around the roof rather than being forced through it. This phenomenon is called the wind-blocking effect. It was first identified by Blocken and Carmeliet in 2006 [38] in their investigations of wind-driven rain deposition on buildings. Later, Blocken et al. [24-26] showed this effect to dominate over the so-called venturi-effect for wind flow in passages between buildings. These two effects also occur for the venturi-shaped roof. The venturi-effect refers to the increase of the wind speed in the roof due to the flow contraction. The wind-blocking effect refers to the decrease of the wind speed in the roof due to the increased resistance in the roof contraction. For the configuration without guiding vanes, it can be said that the venturi-effect dominates over the wind-blocking effect, yielding indeed a strong increase of the wind speed in the contraction and a strong negative underpressure. For the configurations with guiding vanes however, the wind-blocking effect seems to dominate over the venturi-effect: the increase of wind speed in the roof contraction is almost absent ($U/U_{ref} \approx 1$, see Fig. 11), and the resulting pressure coefficients are very low and might even become positive (overpressure).

In this respect, it is worthwhile to compare the performance of the three different roof configurations A, B and C with that of the reference configuration D, i.e. a building without venturi-shaped roof (see Fig. 2 and Fig. 7g-h). The C_p values at position E are compared in Table 1. The results show that the venturi-shaped roof without guiding vanes has a very good performance in terms of generating a strong underpressure coefficient. On the other hand, including guiding vanes has a negative effect: it cancels the positive effect of the venturi-shaped roof and generally leads to a performance that is even less than that without venturi-shaped roof. This means that for the configuration without guiding vanes, the term "venturi-roof" could be used with some justification, while this justification seems absent for the configurations with guiding vanes. In that case, the terminology should be restricted to "venturi-shaped roof".

It is important to mention the limitations of the present study. This study has focused on three different venturi-shaped roof designs. However, it has been conducted for only one set of parameters b, c, g and f (see Fig. 1). It has also only been conducted for one building geometry (L x B x H = 20 m x 20 m x 50 m) and without explicitly including the effect of surrounding buildings. Note that the effect of (distant) urban surroundings was included using an aerodynamic roughness length $y_0 = 0.5$ m (full scale value). Finally, the present study did not model the exhaust air flow coming from the building zones and being extracted by the generated underpressure. Therefore, further research should focus on at least the following important issues:

- Optimization of the performance of the venturi-shaped roof by the optimum combination of parameters b and c;
- Analysing the influence of the overall building dimensions (L, B, H) on the performance of the venturi-shaped roof;
- Analysing the influence of the approach-flow profile (y_0 value) on the roof performance;
- Analysing the influence of explicitly modelled urban surroundings (neighbouring buildings) on the roof performance;
- Analysing the performance of the venturi-shaped roof including the discharge of exhaust air in the roof contraction.

The present and future research efforts are intended to support the design of new buildings with a venturi-shaped roof to drive the natural ventilation of the building zones. Given the importance of exposure of the building roof to the oncoming wind, this roof concept will typically be applied for medium-rise and/or high-rise buildings, or for low-rise buildings without significant nearby obstructions. More information about the integration of this roof concept into a larger framework of sustainable building design can be found in [2].

7. Conclusions

In this study, Computational Fluid Dynamics (CFD) and wind tunnel experiments have been used to analyse the wind flow conditions in a venturi-shaped roof, with focus on the underpressure in the narrowest roof section (contraction). This underpressure can be used to partly or completely drive the natural ventilation of the building zones. The following conclusions have been obtained:

- The 3D CFD simulations were performed with special care for high-quality grid generation, specification of consistent boundary conditions and comparison with detailed wind tunnel measurements.
- The 3D steady RANS CFD simulations with the RNG k-ε model show a good agreement with the wind tunnel measurements for the mean wind speed ratio inside the roof. For the surface pressures inside the roof,

the agreement is less good, but this less agreement does not compromise the evaluation of the different design configurations.

- The following different design configurations of the venturi-shaped roof have been analysed: without guiding vanes, with guiding vanes at every 90° interval and with guiding vanes at every 10° interval.
- The configuration without guiding vanes strongly outperforms the other configurations in terms of the magnitude of the underpressure in the roof contraction. The reason is that adding guiding vanes strongly increases the flow resistance, which causes a larger part of the approaching wind flow to flow over and around the roof, rather than being forced through it. This phenomenon has been called wind-blocking effect in previous studies.
- The wind-blocking effect causes the – at least at first sight – strange observation that the venturi-shaped roof with guiding vanes performs worse than the configuration without venturi-shaped roof.
- For the configuration without guiding vanes, the venturi-effect dominates over the wind-blocking effect. Indeed, due to the flow contraction, the mean wind speed in the contraction and the resulting underpresssure are strongly augmented. This is in line with the definition of the venturi-effect (i.e. increase in fluid speed due to flow contraction) and therefore provides justification to call the roof not only a "venturi-shaped roof" but also a "venturi-roof".
- For the configurations with guiding vanes, the wind-blocking effect dominates over the venturi-effect, and the roof can be called "venturi-shaped roof" but should not be called a "venturi-roof".
- The results of this study only apply for the roof and building configurations studied here. Further research is needed to expand the validity of the present findings, especially concerning the balance between the venturi-effect and the wind-blocking effect.

References

[1] Khan N, Su Y, Riffat SB. A review on wind driven ventilation techniques. Energy Build 2008;40(8), 1586-1604.

[2] Bronsema B. Earth, Wind & Fire – Air-conditioning powered by nature. 10th REHVA World Congress CLIMA 2010, 9-12 May, Antalya, Turkey.

[3] Chen Q. Ventilation performance prediction for buildings: A method overview and recent applications. Build Environ 2009;44(4) 848-858.

[4] Linden PF. The fluid mechanics of natural ventilation. Annu Rev Fluid Mech 1999;31: 201-238.

[5] Hunt GR, Linden PF. The fluid mechanics of natural ventilation - displacement ventilation by buoyancy-driven flows assisted by wind. Build Environ 1999;34(6): 707-720.

[6] Heiselberg P, Li Y, Andersen A, Bjerre M, Chen Z. Experimental and CFD evidence of multiple solutions in a naturally ventilated building. Indoor Air 2004;14(1): 43-54.

[7] Li YG, Delsante A. Natural ventilation induced by combined wind and thermal forces. Build Environ 2001;36(1): 59-71.

[8] Costola D, Blocken B, Hensen JLM. Overview of pressure coefficient data in building energy simulation and airflow network programs. Build Environ 2009;44(10): 2027-2036.

[9] Costola D, Blocken B, Ohba M, Hensen JLM. Uncertainty in airflow rate calculations due to the use of surface-averaged pressure coefficients. Energy Build 2010;42(6): 881-888.

[10] Tsutsumi J, Katayama T, Ishii A, He P, Hayashi T. Investigation and numerical simulation of the wind effects on thermal comfort in a house. J Wind Eng Ind Aerod 1996;60(1-3): 267-280.

[11] Gao NP, Niu JL, Perino M, Heiselberg P. The airborne transmission of infection between flats in high-rise residential buildings: Tracer gas simulation. Build Environ 2008;43(11): 1805-1817.

[12] Tablada A, de Troyer F, Blocken B, Carmeliet J, Verschure H. On natural ventilation and thermal comfort in compact urban environments - the Old Havana case. Build Environ 2009;44(9): 1943-1958.

[13] van Hooff T, Blocken B. Coupled urban wind flow and indoor natural ventilation modelling on a high-resolution grid: A case study for the Amsterdam ArenA stadium. Environ Modell Softw 2010;25(1): 51-65.

[14] Jiang Y, Alexander D, Jenkins H, Arthur R, Chen Q. Natural ventilation in buildings: Measurement in a wind tunnel and numerical simulation with large-eddy simulation. J Wind Eng Ind Aerod 2003;91(3) 331-353.

[15] Karava P, Stathopoulos T, Athienitis AK. Wind-induced natural ventilation analysis. Sol Energy 2007;81(1): 20-30.

[16] Karava P, Stathopoulos T, Athienitis AK. Airflow assessment in cross-ventilated buildings with operable facade elements. Build Environ 2011;46(1): 266-279.

[17] Bu Z, Kato S, Takahashi T. Wind tunnel experiments on wind-induced natural ventilation rate in residential basements with areaway space. Build Environ 2010;45(10): 2263-2272.

[18] Norton T, Grant J, Fallon R, Sun DW. Assessing the ventilation effectiveness of naturally ventilated livestock buildings under wind dominated conditions using computational fluid dynamics. Biosystems Engineering 2009;103(1): 78-99.
[19] Norton T, Grant J, Fallon R, Sun DW. Optimising the ventilation configuration of naturally ventilated livestock buildings for improved indoor environmental homogeneity. Build Environ 2010;45(4): 983-995.
[20] van Hooff T, Blocken B. On the effect of wind direction and urban surroundings on natural ventilation of a large semi-enclosed stadium. Comput Fluids 2010;39(7): 1146-1155.
[21] Blocken B, Stathopoulos T, Carmeliet J, Hensen JLM. Application of CFD in building performance simulation for the outdoor environment: an overview. Journal of Building Performance Simulation 2011; in press. doi: 10.1080/19401493.2010.513740
[22] Chikamoto T, Kato S, Ikaga T. Hybrid air-conditioning system at Liberty Tower of Meiji University. First International One day Forum on Natural and Hybrid Ventilation (HybVent Forum'99), Sydney, Australia, 1999.
[23] Sauerbruch M, Hutton L. 2000. GSW headquarters Berlin. Lars Müller, Berlin, 2000.
[24] Blocken B, Carmeliet J, Stathopoulos T. CFD evaluation of the wind speed conditions in passages between buildings – effect of wall-function roughness modifications on the atmospheric boundary layer flow. J Wind Eng Ind Aerod 2007;95(9-11): 941-962.
[25] Blocken B, Stathopoulos T, Carmeliet J. Wind environmental conditions in passages between two long narrow perpendicular buildings. J Aerospace Eng–ASCE 2008;21(4): 280-287.
[26] Blocken B, Stathopoulos T, Carmeliet J. A numerical study on the existence of the Venturi-effect in passages between perpendicular buildings. J Eng Mech-ASCE 2008;134(12): 1021-1028.
[27] Franke J, Hellsten A, Schlünzen H, Carissimo B (Eds.). Best practice guideline for the CFD simulation of flows in the urban environment. COST Office Brussels; 2007.
[28] Tominaga Y, Mochida A, Yoshie R, Kataoka H, Nozu T, Yoshikawa M, Shirasawa T. AIJ guidelines for practical applications of CFD to pedestrian wind environment around buildings. J Wind Eng Ind Aerod 2008;96(10-11): 1749-61.
[29] van Hooff T, Blocken B, van Harten M. 3D CFD simulations of wind flow and wind-driven rain shelter in sports stadia: influence of stadium geometry. Build Environ 2011;46(1): 22-37.
[30] Launder BE, Spalding DB, The numerical computation of turbulent flows. Comput Method Appl M 1974;3: 269-289.
[31] Cebeci T, Bradshaw P. Momentum transfer in boundary layers, Hemisphere Publishing Corporation; 1977.
[32] Fluent Inc. Fluent 6.3. User's Guide. Fluent Inc., Lebanon; 2006.
[33] Blocken B, Stathopoulos T, Carmeliet J. CFD simulation of the atmospheric boundary layer: wall function problems. Atmos Environ 2007;41(2): 238-252.
[34] Yakhot V, Orszag SA, Thangam S, Gatski TB, Speziale CG. Development of turbulence models for shear flows by a double expansion technique. Physics of Fluids 1992;A4: 1510-1520.
[35] Evola G, Popov V. Computational analysis of wind driven natural ventilation in buildings. Energy Build 2006;38(5): 491-501.
[36] Murakami S. Comparison of various turbulence models applied to a bluff body. J Wind Eng Ind Aerod 1993;46 & 47: 21-36.
[37] Tominaga Y, Mochida A, Murakami S, Sawaki S. Comparison of various revised k–ε models and LES applied to flow around a high-rise building model with 1:1:2 shape placed within the surface boundary layer. J Wind Eng Ind Aerod;96 (4), 389-411.
[38] Blocken B, Carmeliet J. The influence of the wind-blocking effect by a building on its wind-driven rain exposure. J Wind Eng Ind Aerod 2006;94(2): 101-127.

FIGURE CAPTIONS

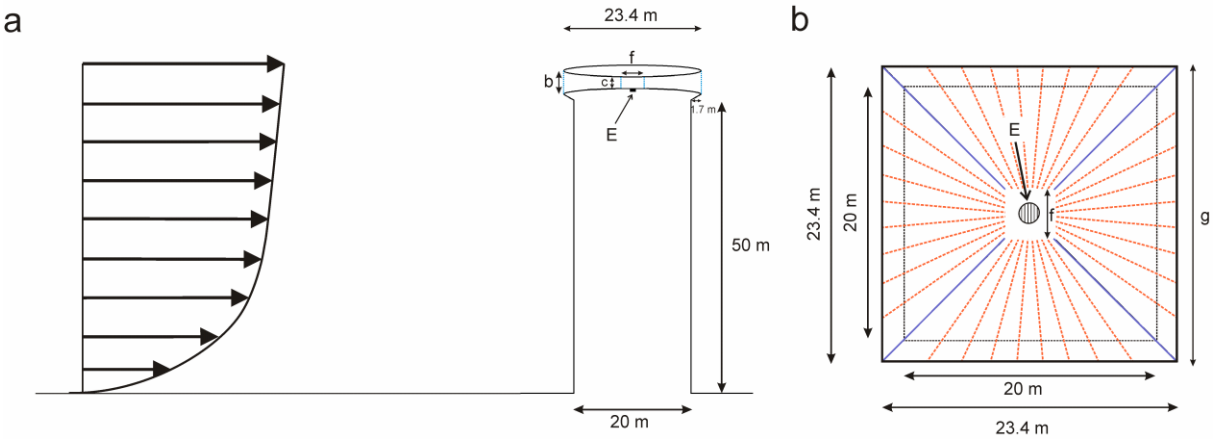

Fig. 1: Geometry of the building used for the wind tunnel experiments and the CFD simulations (a) Vertical cross-section showing the building with the square disk-shaped roof (not to scale) and position E where the surface pressure is evaluated. (b) Horizontal cross-section of the roof. The solid blue lines represent the guiding vanes positioned at every 90° interval, the dashed orange lines indicate the positions of the guiding vanes at every 10° interval.

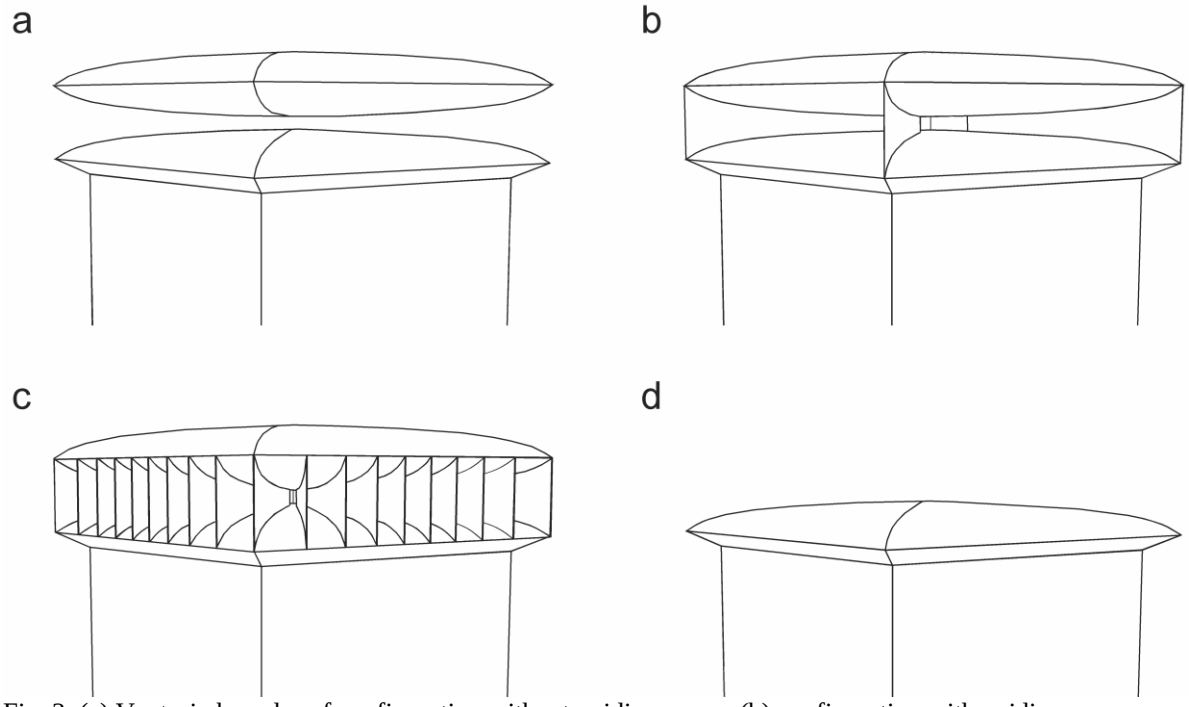

Fig. 2: (a) Venturi-shaped roof configuration without guiding vanes; (b) configuration with guiding vanes every 90°; (c) configuration with guiding vanes every 10°. (d) Reference configuration without venturi-shaped roof.

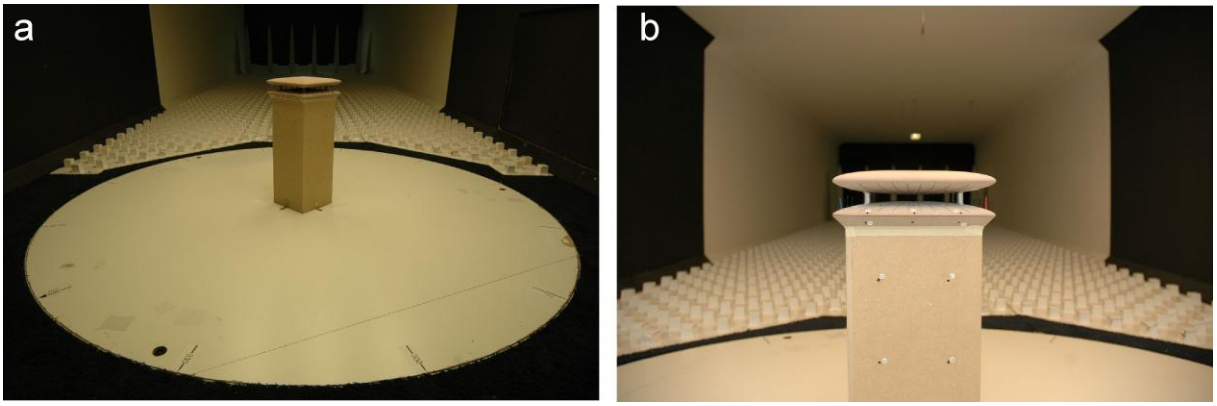

Fig. 3: Pictures of the building model in the closed-circuit ABL wind tunnel at Peutz BV. (a) View of the upstream domain with building model positioned in the middle of the turntable for wind direction of 45°. (b) Close-up view of the building showing some of the leeward facade locations of the surface pressure measurements (see also Fig. 4).

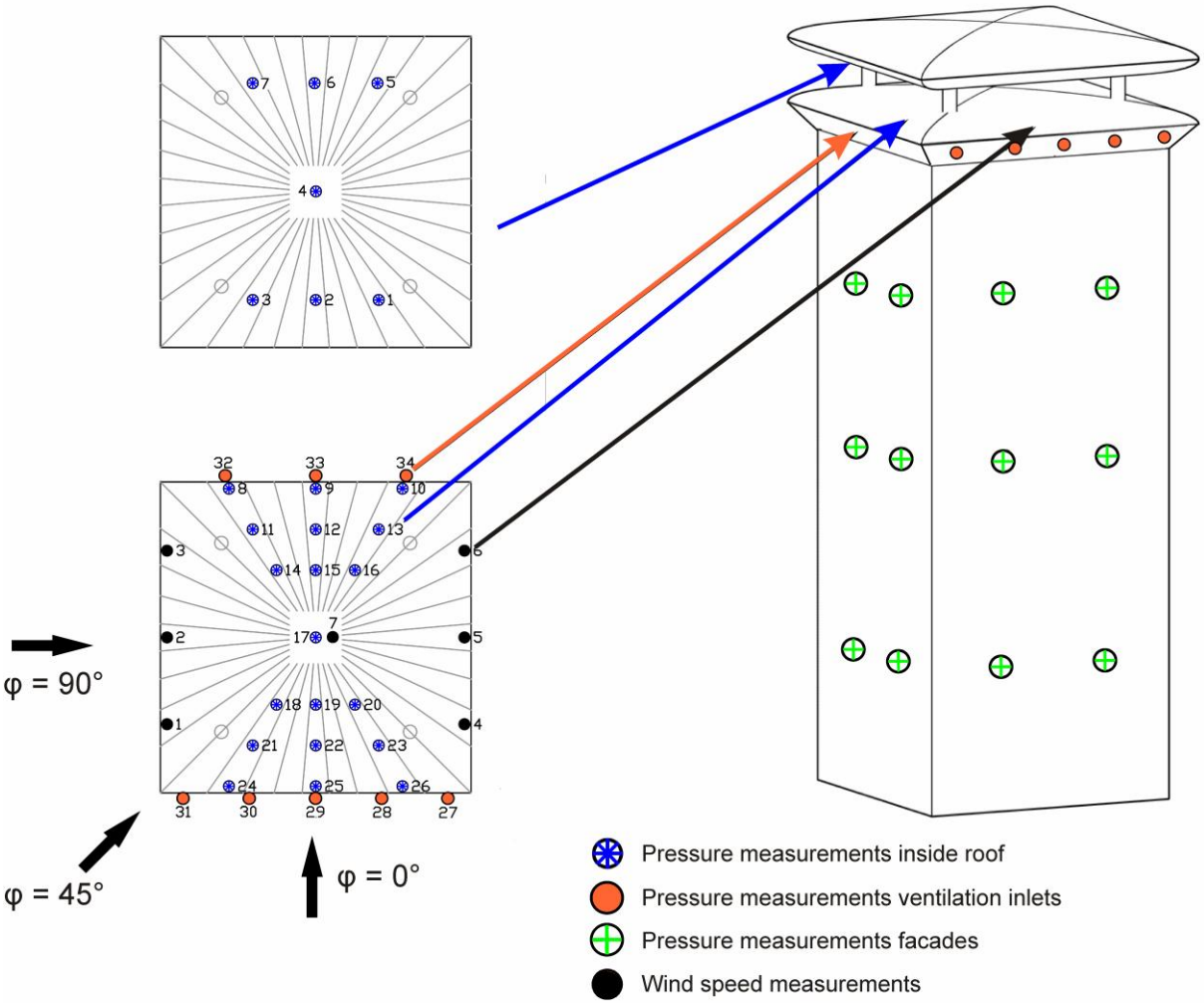

Fig. 4: Schematic view of the building model with indication of the measurement positions. The blue (star-type) symbols indicate the positions of the surface pressure measurements inside the roof, the solid red symbols indicate the positions of the surface pressure measurements at the ventilation inlets of the building, the green (cross-type) symbols indicate the position of the surface pressure measurements on the facades. Finally, the solid black symbols indicate the position of the wind speed measurements, which are performed at mid-height inside the roof contraction.

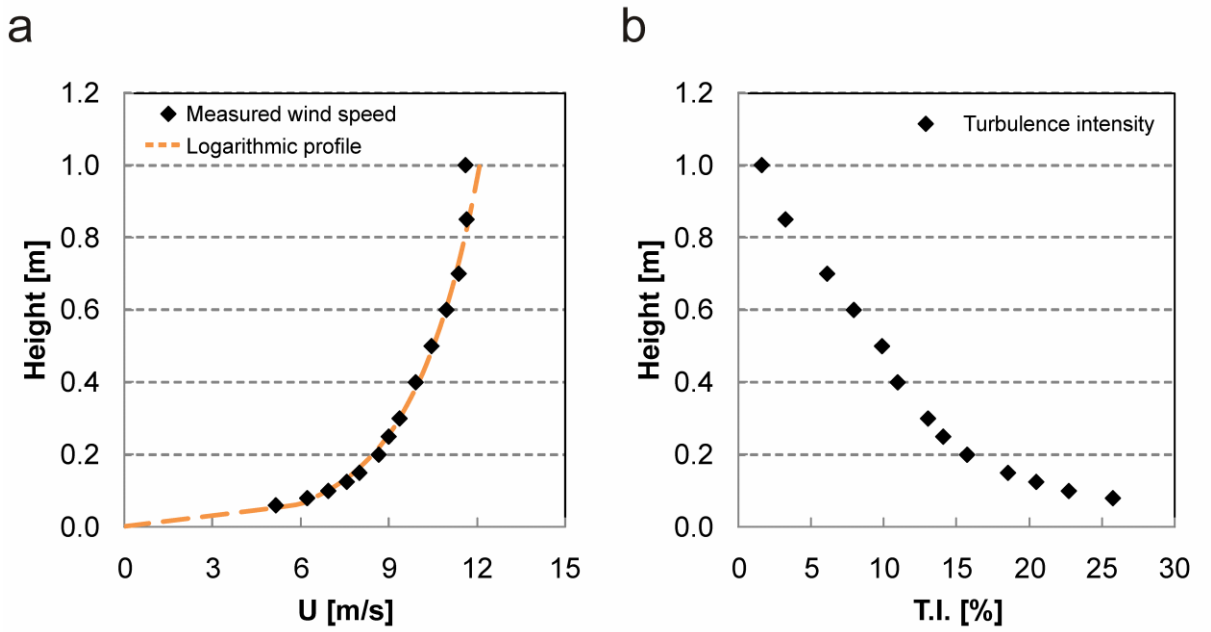

Fig. 5: (a) Measured approach-flow mean wind speed profile along a vertical line at the upstream edge of the turntable. It closely resembles a log law profile with u* = 0.956 m/s and y_0 = 0.005 m (full–scale y_0 = 0.5 m). (b) Measured turbulence intensity T.I. along the same vertical line.

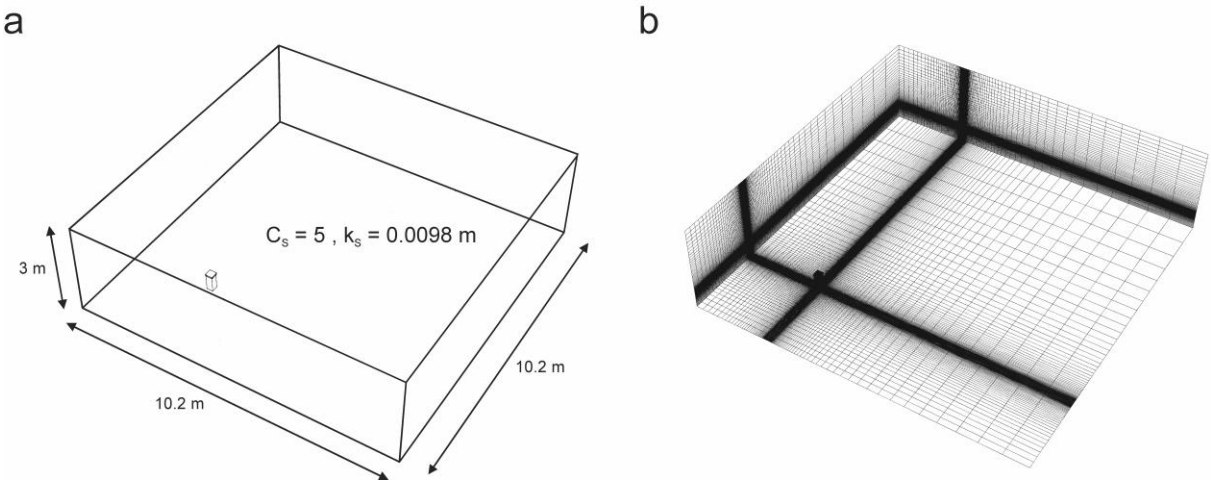

Fig. 6: (a) Perspective view of the building in its computational domain at model scale. (b) View of the computational grid at some of the domain surfaces.

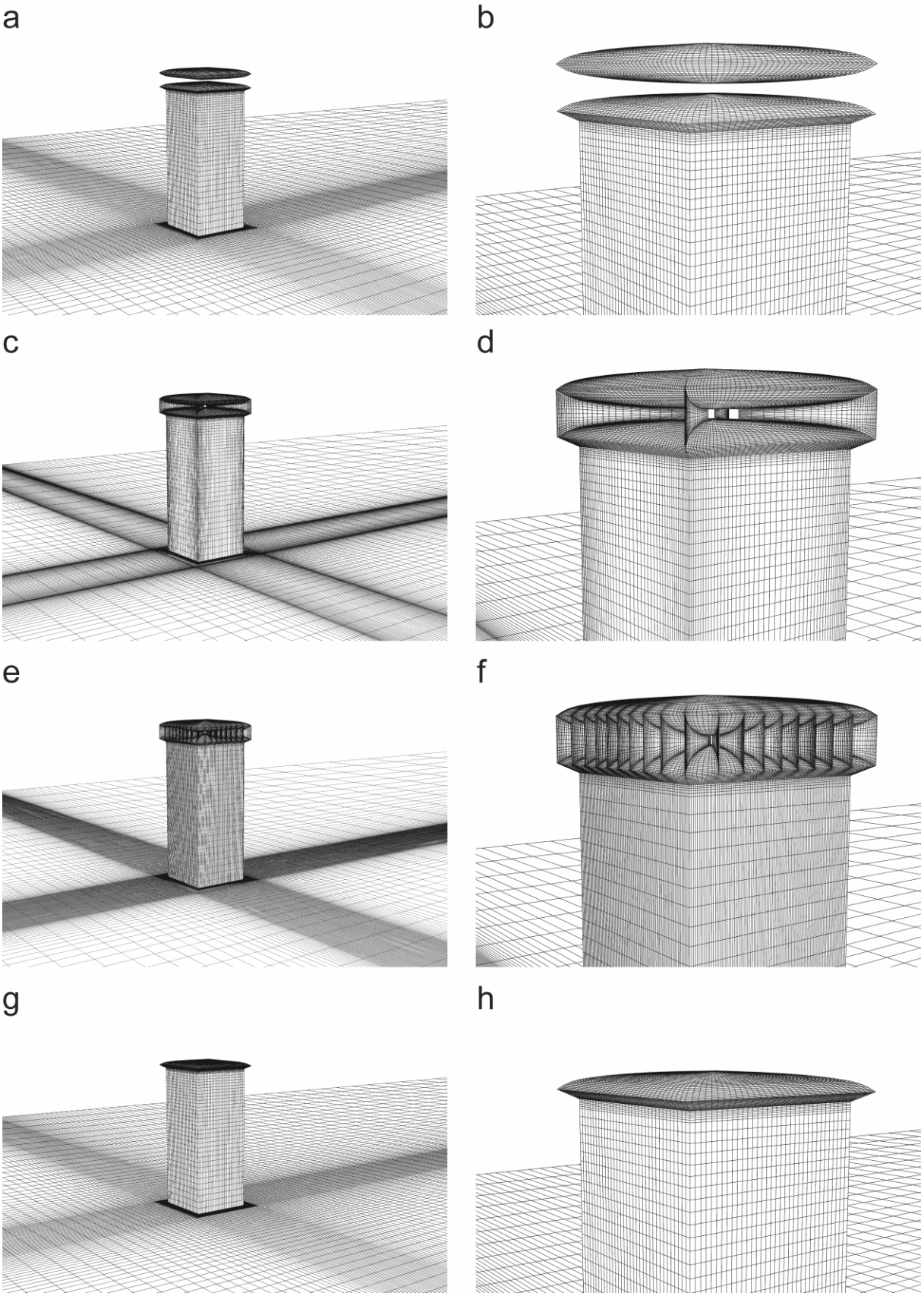

Fig. 7: Computational grids for the three different design configurations and the reference configuration: (a,b) no guiding vanes (2,0 million cells); (c,d) guiding vanes every 90° (2,4 million cells); (e,f) guiding vanes every 10° (3.3 million cells); (g,h) no venturi-shaped roof (1.8 million cells).

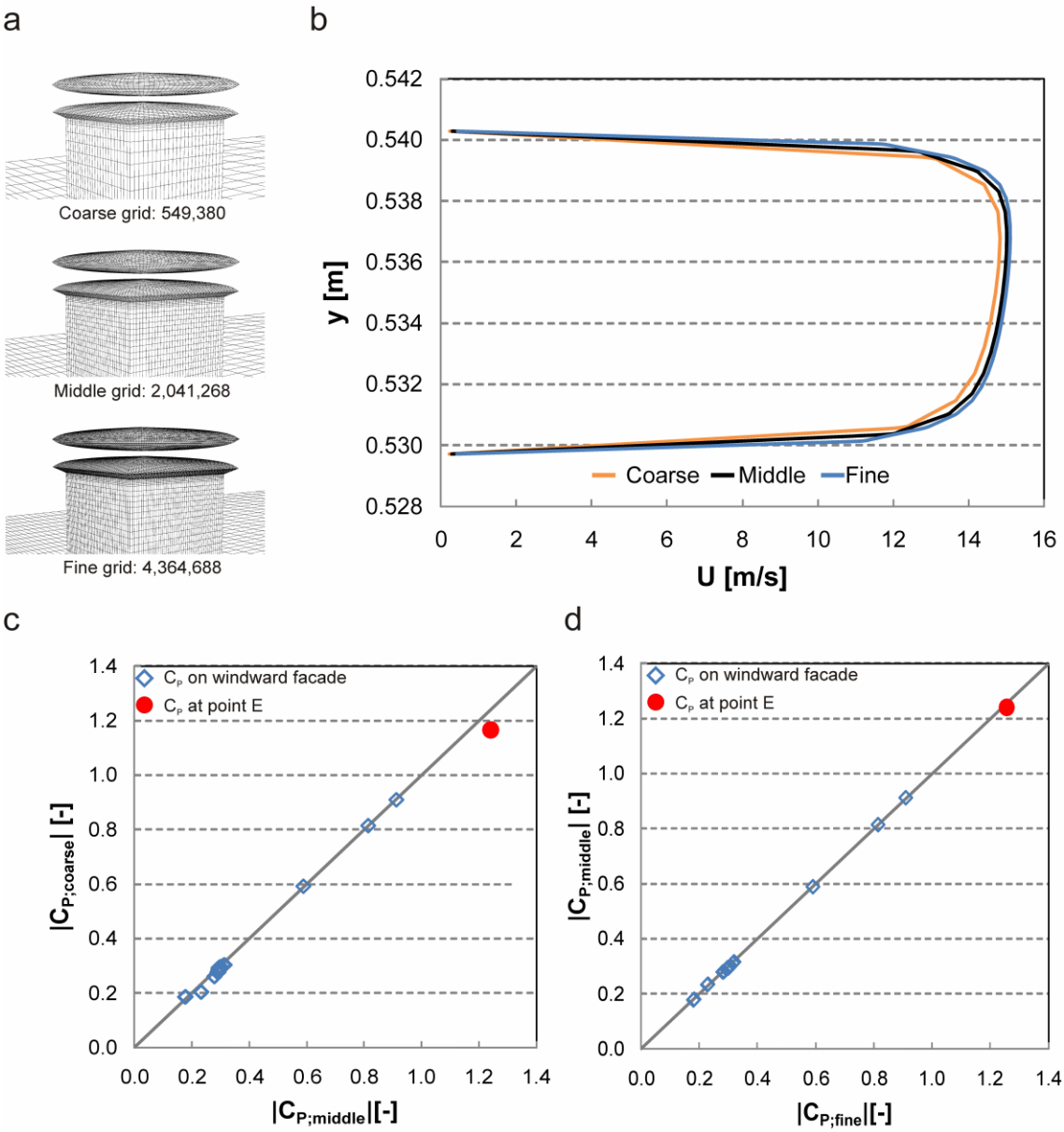

Fig. 8: Grid-sensitivity analysis for configuration A (no guiding vanes) and φ = 0°. (a) View of the three computational grids: coarse grid (549,380 cells), middle grid (2,041,268 cells) and fine grid (4,364,688 cells). (b) Mean wind speed profile for the three grids along a vertical line in the centre of the roof contraction. (c) Comparison of pressure coefficients obtained with the coarse grid and the middle grid. (d) Comparison of pressure coefficients obtained with the middle grid and the fine grid.

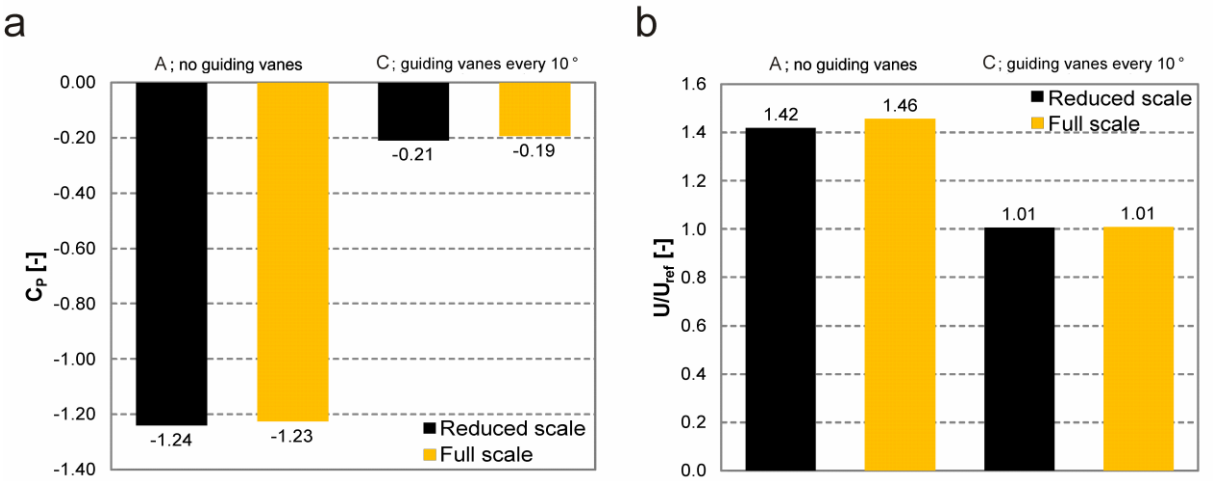

Fig. 9: Comparison between results obtained from CFD simulations with the reduced-scale model and the full-scale model for configurations A and C and for a wind direction φ = 0°. (a) Comparison of pressure coefficient at position E. (b) Comparison of wind speed ratio U/U_{ref} at mid-height in the centre of the roof contraction.

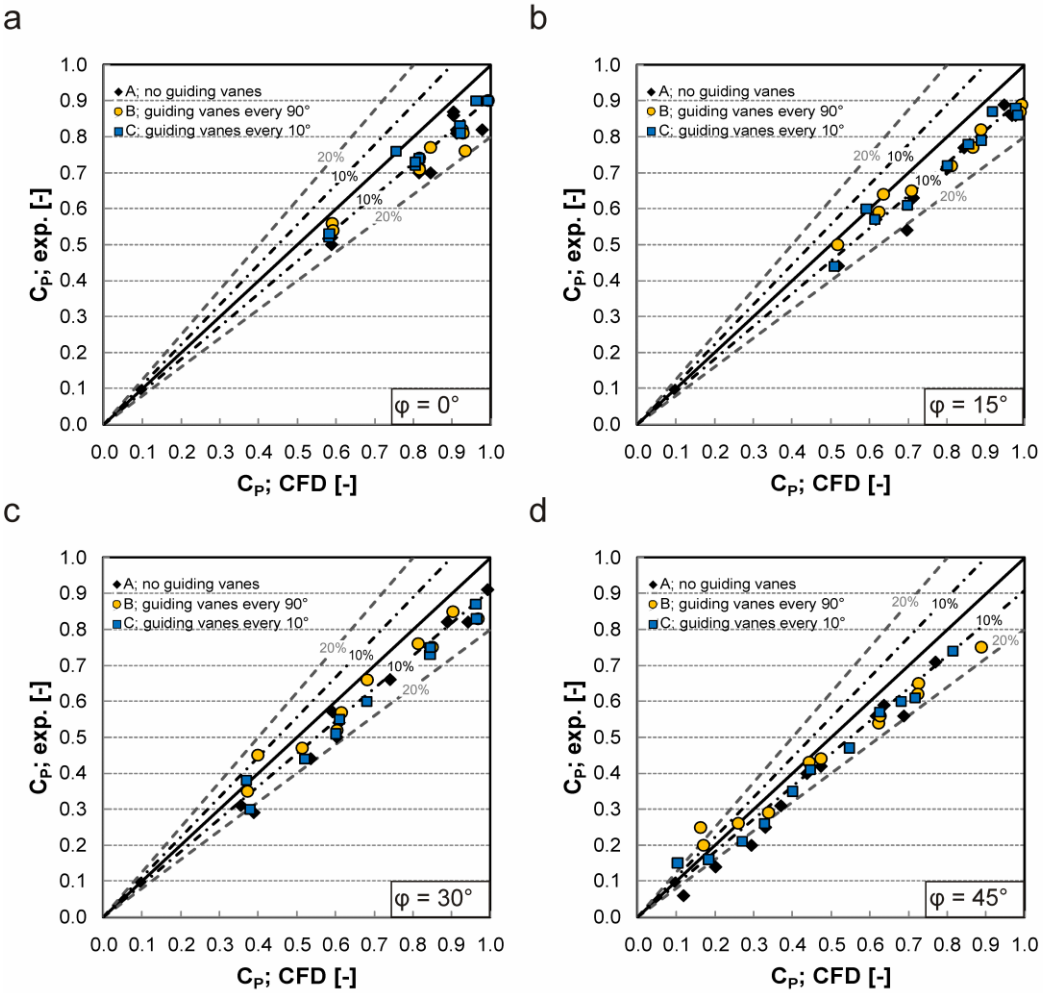

Fig. 10: Comparison between numerically simulated and measured pressure coefficients C_P on the windward facades and the windward ventilation inlet of the building for the roof configurations A, B, C and for the four wind directions: (a) φ = 0°; (b) φ = 15°; (c) φ = 0°; (d) φ = 45°.

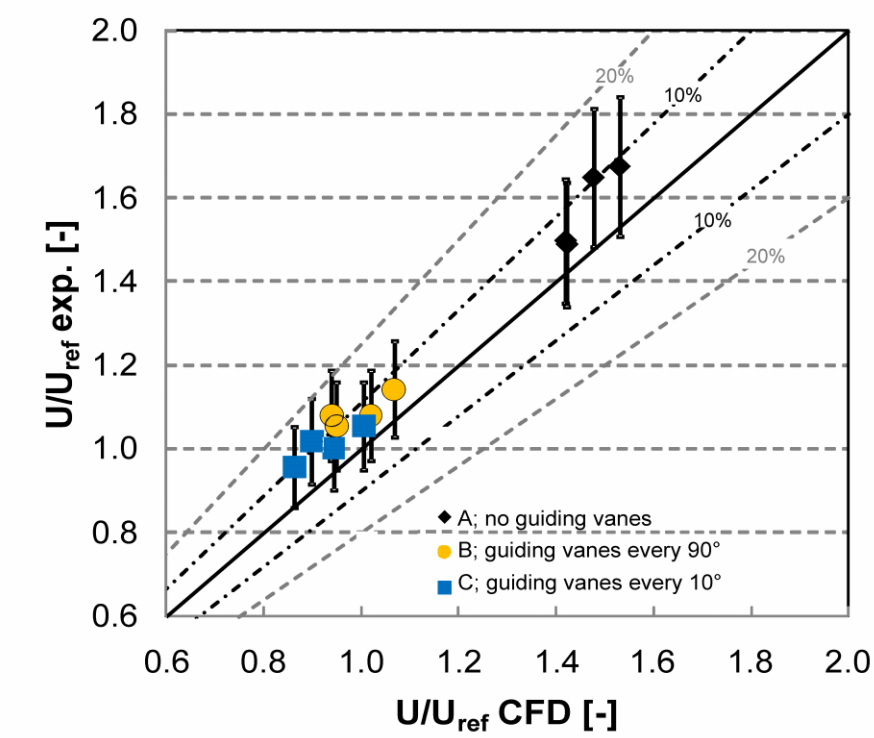

Fig. 11: Comparison between numerically simulated and measured velocity ratio U/U_{ref} at mid-height in the centre of the roof contraction for the roof configurations A, B, C and for the four wind directions (φ = 0°, 15°, 30°, 45°). The error bars represent the measuring accuracy of ±10%.

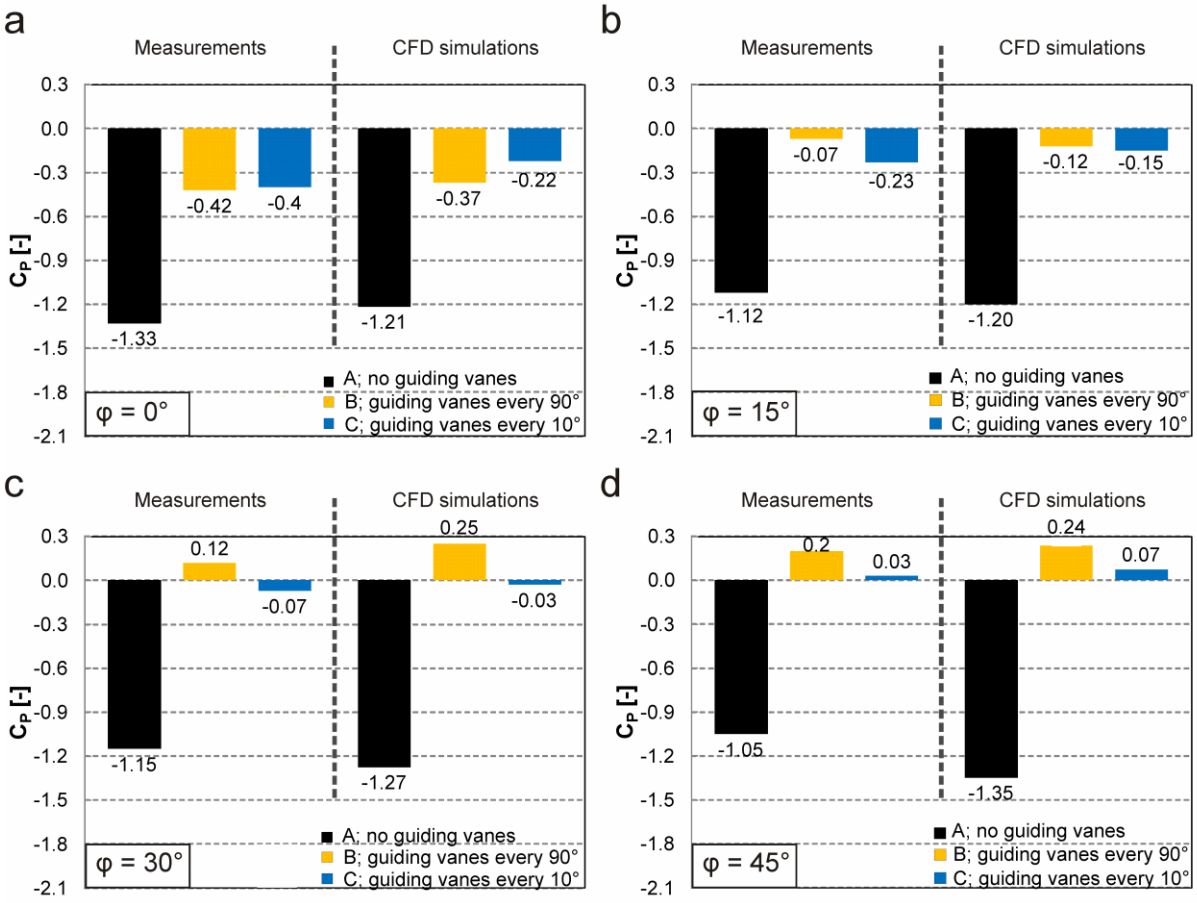

Fig. 12: Comparison between numerically simulated and measured pressure coefficients C_P at position E for the roof configurations A, B, C and for the four wind directions: (a) φ = 0°; (b) φ = 15°; (c) φ = 30°; (d) φ = 45°.

Blocken B, van Hooff T, Aanen L, Bronsema B. 2011. Computational analysis of the performance of a venturi-shaped roof for natural ventilation: venturi-effect versus wind-blocking effect.
***Computers & Fluids** 48(1): 202-213.*

Computational analysis of the performance of a venturi-shaped roof for natural ventilation: venturi-effect versus wind-blocking effect

B. Blocken * [(a)], T. van Hooff [(a,b)], L. Aanen [(c)] , B. Bronsema [(d)]

(a) Building Physics and Systems, Eindhoven University of Technology, P.O. box 513, 5600 MB Eindhoven, the Netherlands
(b) Division of Building Physics, Department of Civil Engineering, Katholieke Universiteit Leuven, Kasteelpark Arenberg 40, P.O. Box 2447, 3001 Leuven, Belgium
(c) Peutz BV, P.O. box 66, 6585 ZH, Mook, The Netherlands
(d) Faculty of Architecture – Department of Climate Design, Delft University of Technology, Prof. Boerhaaveweg 37, 2251 HX Voorschoten, The Netherlands

Abstract
Computational Fluid Dynamics (CFD) is used to gain insight in the aerodynamic performance of a venturi-shaped roof (called VENTEC roof). The simulations are performed with the 3D steady Reynolds-averaged Navier-Stokes (RANS) equations and the Renormalization Group k-ε model. A detailed analysis is conducted of the influence of the so-called venturi-effect and the wind-blocking effect on the aerodynamic performance of the VENTEC roof. The specific roof configuration is intended to create a negative pressure in the narrowest roof section (contraction) which can be used to partly or completely drive the natural ventilation of the building zones. The CFD simulations are based on a detailed grid-sensitivity analysis and on successful validation of the grid-independent results by comparison with experiments in an atmospheric boundary layer wind tunnel. The simulations show that the aerodynamic performance of the roof is governed by the balance between the so-called venturi-effect on the one hand and the wind-blocking effect on the other hand. The venturi-effect cannot act to its full extent because the flow is non-confined. The wind-blocking effect refers to the effect of the resistance exerted by the roof contraction on the air flow and the resulting tendency of the approaching wind to flow around and over the roof, rather than only being forced through the roof contraction. The results indicate that because of the wind-blocking effect, the highest contraction ratio does not provide the best aerodynamic performance and the largest negative pressure, which is a counter-intuitive result. The paper also provides a parametric analysis to optimise the roof contraction height and contraction ratio. The study in this paper illustrates the use of CFD to increase insight in building aerodynamics and to support sustainable building design.

Keywords: Computational Fluid Dynamics (CFD); natural ventilation; venturi-effect; wind-blocking effect; buildings; energy efficiency

1. Introduction

Energy efficiency is an increasingly important design criterion for buildings and urban areas. Natural ventilation or hybrid natural-mechanical ventilation of buildings can be used to provide a comfortable and healthy indoor environment with reduced energy consumption. Natural ventilation is based on either wind-induced pressure differences or thermally-induced pressure differences, or – most often – a combination of both [1-7].

The potential for natural ventilation can be significantly enhanced by the design of the building. Research on natural ventilation of buildings can be performed using different methods [8], including experiments [1,2,5,6,9-17], analytical and/or semi-empirical formulae [1-3,5,15,18,19] and numerical simulation with Computational Fluid Dynamics (CFD) [6,9-13,20-23]. CFD has a number of clear advantages compared with the other approaches (e.g. [24]): (1) as opposed to most experimental techniques, CFD provides whole-flow field data, i.e. data on the relevant parameters in every point of the computational domain; (2) CFD avoids the sometimes incompatible similarity requirements in reduced-scale testing because simulations can be performed at full scale; and (3) CFD allows full control over the boundary conditions and easily and efficiently allows parametric studies

* **Corresponding author**: Bert Blocken, Building Physics and Systems, Eindhoven University of Technology, P.O.Box 513, 5600 MB Eindhoven, the Netherlands. Tel.: +31 (0)40 247 2138, Fax +31 (0)40 243 8595
E-mail address: b.j.e.blocken@tue.nl

to be performed. For these reasons, many studies on evaluating and optimising the natural ventilation potential of buildings have employed CFD (e.g. [6,9-13,20-23]).

Because the roof of a building is often the most exposed part to the oncoming wind, in particular the roof geometry can be employed to enhance natural ventilation. This reasoning has driven the design of a specific venturi-shaped roof by Bronsema in the framework of the research project "Earth, Wind & Fire – Air-conditioning powered by Nature" [7] (Fig. 1). The roof is called the Ventec roof, which is the combination of the Latin word "ventum" (wind) and "tectum" (roof), or the combination of the words "ventilation" and "technology". The Ventec roof consists of a disk-shaped roof construction that is positioned at a certain height above the actual building, creating a contraction that is expected to provide significant negative pressures due to the so-called Venturi-effect. The negative pressure can be used to partly or completely drive the natural ventilation of the building zones. For this purpose, a vertical channel (not shown in Fig. 1) is provided in the centre of the building, which connects point E of the roof contraction with the building zones at each floor. In a previous paper [23], the present authors have provided a preliminary evaluation of the aerodynamic performance of this roof design by CFD and wind tunnel experiments. At this stage, it was found that adding vertical guiding vanes in the roof contraction actually did not improve but cancelled the effect of the contraction. It was suggested that due to the guiding vanes, the flow resistance through the contraction became too large and that therefore the oncoming wind would flow over and around the roof and the building, rather than being forced to flow between and along the guiding vanes in the contraction. This phenomenon was called the "wind-blocking effect" in earlier studies [23,25-27]. However, this previous study [23] on the venturi-shaped roof did neither investigate the wind-blocking effect in detail, nor did it provide an optimisation analysis of the roof contraction height and contraction ratio. These two effects and the optimisation analysis are interrelated and they are the main focus of the present paper.

In the present study, 3D steady Reynolds-averaged Navier-Stokes (RANS) CFD with the Renormalization Group (RNG) k-ε model is used to investigate the balance between the so-called venturi-effect and the wind-blocking effect for flow through and around the venturi-shaped roof and to determine the optimum contraction height. RANS CFD requires turbulence modelling, which in turn requires solution verification and validation studies. Therefore, the study also contains a detailed grid-sensitivity analysis and a validation study based on comparison of the grid-independent simulation results with a set of experiments in an atmospheric boundary layer wind tunnel. Next, the validated CFD model is used for a series of parametric CFD simulations that allow (1) optimising the aerodynamic performance of the roof in terms of the roof contraction height and (2) investigating the balance between the venturi-effect and the wind-blocking effect.

2. Venturi-effect and wind-blocking effect

In this section, the venturi-effect and the wind-blocking effect are briefly addressed. The venturi-effect refers to the increase of the fluid speed due to a decrease of the flow cross-section [27,28]. This effect was originally defined for confined flows [28], but the same terminology has been used for non-confined flow or open flows, e.g. to describe the increase of wind speed in passages between buildings [29-31]. Recent research however has shown that in a passage between two buildings, the venturi-effect is – at least in some cases – not the governing effect [25-27]. Indeed, as the passage width decreases, the resistance for flow through the passage increases and more wind will flow around and over the building passage, rather than being forced to flow through it. Blocken et al. [25-27] referred to this as the "wind-blocking effect": the high resistance of the passage partly blocks the flow through the passage and diverts a large part of the oncoming wind over and around the buildings and the passage. This is an explicit characteristic of non-confined flows, and therefore the term venturi-effect is less suitable here [25,27]. A detailed analysis in terms of average wind speed and wind fluxes was performed, confirming that – at least for the building configurations under investigation – the so-called venturi-effect was not present, because it was overruled by the wind-blocking effect [25-27]. Figure 2 illustrates results of this previous study for buildings in a so-called converging arrangement. In the past, this arrangement has been called "venturi-throat". The presence of the venturi-effect would at least imply that the fluxes (flow rates) through the passage plane are higher than the free-field flux through a similar plane in the upstream undisturbed flow. However, the previous CFD study, validated by wind tunnel experiments, has shown that the flow rates through these "converging" building passages are consistently lower than the corresponding free-field flow rates, irrespective of the passage width (Fig. 2a). This implies that the term venturi-effect is not really applicable for such building configurations. Therefore, as a general rule for non-confined flows, the term venturi-effect should be used with caution, because it is not known in advance to which extent this effect will be overruled by the wind-blocking effect. Figure 2b shows that the wind-blocking effect causes an uplift of the approaching flow and part of it therefore flows over the buildings and the passage and not through the passage.

The flow through and around the Ventec roof in the present study is also a non-confined flow. Similar to the case of the two-building configuration in [25-27], the resulting wind flow through the roof will be influenced by the resistance of the contraction. In the next sections, the balance between the venturi-effect (due to roof

contraction) and the wind-blocking effect (due to resistance caused by roof contraction) will be analysed for the building in Fig. 1 with varying contraction height c. Note that in this paper, we will use the term "venturi-effect" to refer to the expected increase of flow speed and negative pressure in the contraction, in spite of the non-confined flow conditions.

3. Description of building and roof geometry

Fig. 1 illustrates the geometry under study. The building has a rectangular (20 m x 20 m) floor plan and a height of 50 m, measured up to the edge of the roof. The Ventec roof consists of two parts. The lower part is constructed from half a "square disk" with dimensions 23.4 m x 23.4 m x 2 m (L x W x H) and it is positioned directly on top of the building, this way creating a roof overhang of 1.7 m on each side of the building, at which ventilation inlets will be placed. At a distance 'c' (contraction height) above this part of the roof a "full square disk" is positioned with dimensions 23.4 m x 23.4 m x 4 m (L x W x H), resulting in a nozzle-shaped roof entrance from all four sides of the building. This part can be supported by a set of slender vertical columns, as indicated in Fig. 1a. In this study, the contraction height c (and therefore also the inlet height b) will be varied by vertically translating the "full square disk" and increasing the distance b and c with the same translation distance. Therefore, the geometry of the building and the square disk itself will not change. The values of the parameter c and the corresponding values of the parameter b and the contraction ratio b/c are given in Table 1.

The position of interest inside the roof contraction is the point in the bottom centre of the roof, indicated with the letter E (from "exhaust") in Figure 1a and b. In this study, the exhaust is considered to be closed and the surface pressure at this position will be evaluated. A reasonable expectation is that at this position, the flow speed will reach a maximum value and that also the resulting absolute value of the negative pressure will reach a maximum value.

All experiments and simulations are conducted for an isolated building, i.e. without surrounding buildings. Therefore, all differences in wind speed and surface pressures between the different configurations are only due to changes in the parameter c.

4. Wind tunnel measurements

A reduced-scale model (1:100) of the building with Ventec roof is constructed and placed in the closed-circuit atmospheric boundary layer (ABL) wind tunnel (Fig. 3) at Peutz BV in Mook, the Netherlands. The dimensions of the wind tunnel test section are 3.2 x 1.8 m^2 (W x H), resulting in a blockage ratio of about 2%. The building model was placed on a turntable with a diameter of 2.3 m. Part of the measurements were reported in the previous paper [23]. In the present paper, additional measurement results for different values of the parameter c are reported. The surface pressure was measured at the position E (Fig. 1) with a HCLA12X5EB amplified differential pressure sensor from Sensortechnics. The wind speed in the roof contraction was measured in the centre of the contraction, at mid-height, using a NTC resistor element. The NTCs are operated with a constant current and are calibrated by Peutz by determining the relationship between wind speed and temperature (and corresponding resistance) of each individual probe. The probes are not direction-sensitive and due to the relatively long reaction time of the probes, only average wind speeds can be measured, with an accuracy of ±10%. Approach-flow vertical profiles of mean wind speed U and turbulence intensity I_u are measured at the edge of the turntable using hot-wire anemometers and are presented in Figure 4. The measured wind speed profile can be described by a logarithmic law with a friction velocity $u^* = 0.956$ m/s and an aerodynamic roughness length $y_0 = 0.005$ m (full scale: $y_0 = 0.5$ m). The incident reference wind speed at roof height (full scale: 50 m) is 10.5 m/s. Measurements are made for four wind directions: $\varphi = 0°$, 15°, 30° and 45°, taking into account the symmetry of the building and the building roof.

5. CFD simulations: geometry, grid, boundary conditions and solver settings

5.1. Computational geometry and grid

After having verified that the results are Reynolds number independent and that simulations at model scale therefore yield similar results as simulations at full scale [23], all other simulations were performed at model scale. For clarity however, all parameter and results will be expressed with full-scale values. The computational domain has (full-scale) dimensions L x B x H = 1020 m x 1020 m x 300 m (Fig. 5a). This domain shape allows modelling different wind directions (0° to 45°). High-quality and high-resolution computational grids were constructed (Fig. 5 and Fig. 6). The grids have at least 10 cells between each two adjacent surfaces as requested by the best practice guidelines by Franke et al. [32] and Tominaga et al. [33]. The grids are made using the grid generation technique presented by van Hooff and Blocken [6]. In this technique, the geometry and the grid are created simultaneously, by a series of extrusion operations. This procedure allows a large degree of control over

the size and shape of the cells, and therefore of the quality and resolution of the computational grid. It allows high-quality grids to be made, even for rather complex geometries. The same technique has been used successfully on previous occasions to model sport stadium geometries [6,22,34]. The grids are block-structured. The number of cells for every configuration (c value) is between about 2.0 and 2.3 million cells. Note that the grids do not contain any pyramidal or tetrahedral cells. Special attention was paid to the detailed reproduction and meshing of the wind roof geometry. A high grid resolution is applied in the proximity of the roof in view of the expected large flow gradients (Fig. 6 and 7). A detailed grid-sensitivity analysis was performed indicating that the grid resolution shown in Figure 6c provides nearly grid-independent results. The grid-sensitivity analysis will be reported in section 6.1.

5.2. Boundary conditions

At the inlet of the domain the measured approach-flow mean wind speed profile is imposed. Turbulent kinetic energy k is calculated from the turbulence intensity I_u using $k = 0.5(I_u.U)^2$. The turbulence dissipation rate $\varepsilon = (u^*)^3/\kappa(y+y_0)$, where y is the height coordinate, κ the von Karman constant ($\kappa = 0.42$) and u* the friction velocity related to the logarithmic mean wind speed profile. At the ground and building surfaces, the standard wall functions by Launder and Spalding [35] are used with the sand-grain based roughness modification by Cebeci and Bradshaw [36]. For the ground surface, the parameters k_S and C_S, to be used in Fluent [37] should be selected to correctly represent the rough fetch upstream of the building model (see Fig. 3a). This type of consistent atmospheric boundary layer simulation is very important to obtain accurate simulation results [25,38]. Therefore, k_S and C_S have to be determined using their appropriate consistency relationship with y_0. This relationship was derived by Blocken et al. [38] for Fluent and CFX. For Fluent 6, up to at least version 6.3, it is given by $k_S = 9.793y_0/C_S$. The combination $k_S = 0.98$ m and $C_S = 5$ is selected (see Fig. 5). The building surfaces are assumed to be smooth ($k_S = 0$ m and $C_S = 0.5$). Zero static pressure is imposed at the outlet of the domain and the top of the domain is modelled as a slip wall (zero normal velocity and zero normal gradients of all variables).

5.3. Solver settings

The 3D steady RANS equations are solved in combination with the RNG k-ε turbulence model [39] using Fluent 6.3.26. The RNG k-ε turbulence model was chosen because of its good performance in predicting the surface pressures on the windward building facades and in the roof opening in a preliminary study [23] and because of its superior performance in an earlier study by Evola and Popov [40]. Pressure-velocity coupling is taken care of by the SIMPLE algorithm, pressure interpolation is standard and second-order discretization schemes are used for both the convection terms and the viscous terms of the governing equations. Convergence has been monitored carefully and the iterations have been terminated when all scaled residuals showed no further reduction with increasing number of iterations. At this stage, the scaled residuals [37] were: 10^{-4} for continuity, 10^{-7} for momentum, 10^{-6} for turbulent kinetic energy and 10^{-4} for turbulence dissipation rate.

6. Grid-sensitivity analysis, experimental validation and optimisation results

6.1. Grid-sensitivity analysis

A grid-sensitivity analysis was performed by constructing two additional grids for the configuration with c = 1 m: a coarser grid and a finer grid (Fig. 6 and 7). Coarsening and refining was performed with an overall linear factor $\sqrt{2}$. The coarse grid has 549,380 cells, the middle grid has 2,041,268 cells and the fine grid has 4,364,688 cells. These grids are shown in Fig. 6b-d and Fig. 7a-c. The results on the three grids are compared in Figure 8 in terms of the absolute values of the mean pressure coefficients on the windward building facade and at position E in the roof contraction. The pressure coefficients are computed as $C_p = (P-P_0)/(0.5\rho U_{ref}^2)$ with P the static pressure at the surface, P_0 the reference static pressure, $\rho = 1.225$ kg/m³ the air density and U_{ref} the reference wind speed at roof height ($U_{ref} = 10.5$ m/s at y = 0.5 m). A small deviation (7 %) is found between the coarse and middle grid for the C_p at position E, while almost no deviation is found for the value of this parameter between the middle grid and the fine grid. Therefore, the middle grid (i.e. that in Fig. 6c) is retained for further analysis, and the grids for the other c values are constructed with similar grid resolution.

6.2. Experimental validation

Validation is performed by comparing the CFD simulation results with the wind tunnel measurements. Figure 9 compares the numerically simulated and measured mean pressure coefficients C_p at position E in the centre of the roof contraction. The CFD results and the wind tunnel results are in fairly good agreement. The agreement however seems to deteriorates for the lower c values. These deviations can be attributed to: (1) the specific

geometry of the roof, with four "ribs" on the roof surfaces (see e.g. Fig. 1a); (2) the fact that the vertical roof supports were not included in the numerical model; and (3) the large C_p gradients at the roof surfaces, which are more pronounced for lower c values. In spite of these deviations between the numerical and the measured C_p values, the trends are clear and allow a comparison of the performance of the different roof configurations. Figure 10 compares the numerically simulated and measured mean wind speed ratios U/U_{ref} at mid-height in the centre of the roof contraction, for the three configurations (c = 0.5 m, c = 1 m and c = 2 m) and for the four wind directions. The deviations are generally smaller than 10%, which is considered a very close agreement.

6.3. Optimisation results

Based on the grid-sensitivity analysis and the validation study, CFD simulations are performed to determine the mean C_p at position E for different values of the contraction height c. Figure 11 shows that a maximum (negative) value is obtained for c = 0.5 m. The existence of this optimal value is the result of the balance between the so-called venturi-effect and the wind-blocking effect. This will be examined in more detail in the next section.

7. Analysis of venturi-effect versus wind-blocking effect

A detailed analysis of the flow rates and average wind speeds through different cross-sections of the roof is performed for wind direction $\varphi = 0°$. Figure 12a defines the line segment L_1 in the middle of the roof contraction. Fig. 12b defines the vertical bounded planes A_1, A_2, A_3 and A_6 and the corresponding air flow rates F_1, F_2, F_3 and F_6 through these planes. A_1 is situated in the upstream undisturbed flow and represents "free-field" conditions. A_2 is the "roof contraction inlet" plane. A_3 is the "roof contraction middle plane" and A_6 is the "roof contraction outlet" plane. Note that the areas of A_1, A_2 and A_6 are the same, while the area of A_3 is smaller, due to the specific roof geometry/contraction. Figure 12c defines two additional bounded planes A_4 and A_5, which correspond to the side openings of the roof and which have the same area as A_1. The corresponding air flow rates are F_4 and F_5. Note that Fig. 12 only shows the configuration for one value of the parameter c (c = 1 m). For a given configuration (and value of the parameter c), the areas of the bounded planes A_1, A_2, A_4, A_5 and A_6 are the same. However, these areas vary with c.

Figure 13 illustrates how the ratio F_2/F_1 decreases with decreasing contraction height c. The smaller c, the larger the resistance in the roof contraction (more wind-blocking) and the smaller the ratio of the air flow rate entering the roof contraction (through A_2) to the free-field air flow rate (through A_1).

Figure 14 shows two curves. The first one indicates the decrease of the ratio F_6/F_2 (outlet flow rate to inlet flow rate) with decreasing value of c. The second one shows the increase of the ratio $(F_4 + F_5)/F_2$ (side flow rate to inlet flow rate) with decreasing c. The sum of the two curves is equal to one. These curves indicate that the smaller the contraction height, the larger the resistance and the wind-blocking effect. Due to the wind-blocking effect, a larger fraction of the air that enters the roof will exit through the side planes A_4 and A_5 instead of through the exit plane A_6. This is further clarified in Fig. 15, that shows the velocity vector field in a horizontal plane through the middle of the roof contraction, for c = 0.25 and c = 2 m. Fig. 15a shows a strong lateral deviation of wind flow in the roof for c = 0.25 m, which is much less pronounced for c = 2 m. Fig. 16 shows the velocity vector field in the vertical centre plane for c = 0.25 and c = 2 m. Comparing Fig. 16a and b clearly shows the much stronger exit flow in the case with larger c value. Comparing Fig. 16c and d also shows larger vertical velocity components upstream of the roof inlet, indicating that the wind-blocking forces more of the air to flow over the roof rather than only through it.

Finally, Fig. 17 illustrates curves for two average velocity ratios, in which the average velocity is calculated as the flow rate through the bounded plane divided by the area of the bounded plane, or as the average values of the velocities along the vertical line segment L. The first ratio U_{A3}/U_{A2} is the average velocity through area A_3 (vertical contraction middle plane) to the average velocity through area A_2 (vertical contraction inlet plane). The second ratio U_{L1}/U_{A2} is the average velocity along line segment L_1 to U_{A2}. Both curves illustrate the balance between the venturi-effect and the wind-blocking effect, in which this balance yields a maximum velocity ratio for c = 0.5 m. For lower c values, the higher contraction ratio yields a stronger wind-blocking effect and the ratios decrease. For higher c values, the lower contraction ratio yields a less strong venturi-effect. The fact that the ratio U_{L1}/U_{A2} is always larger than U_{A3}/U_{A2} is a direct consequence of the shape of the roof contraction and indicates that position E is indeed a good position for a ventilation outlet.

8. Discussion

This study has evaluated the balance between the so-called venturi-effect and the wind-blocking effect in the aerodynamic performance of a venturi-shaped roof (called the Ventec roof) for wind-induced natural ventilation of buildings. The study has built further on a previous investigation which included evaluating the effect of

vertical guiding vanes in the contraction [23]. This previous study had shown that adding guiding vanes has a strong negative effect on the aerodynamic performance of the roof, which was attributed to the wind-blocking effect that overruled the venturi-effect.

Therefore, the present study has investigated the venturi-effect and the wind-blocking effect in detail. It has also investigated the optimum contraction height. While the study has provided new insights in the aerodynamic performance of the Ventec roof, the study also has some important limitations. It has focused on only one building geometry (L x B x H = 20 m x 20 m x 50 m), one roof geometry (square disk of 23.4 m x 23.4 m with 4 m maximum thickness) and – for the largest part – also only one wind direction. The study did also not explicitly include the effect of surrounding buildings. Finally, also the exhaust air flow coming from the building zones and being extracted by the generated negative pressure was not modelled. Therefore, it is possible that in a real situation the optimum contraction height (and contraction ratio) will be somewhat different. Nevertheless, in spite of these limitations, this study has clarified the two main aerodynamic effects that determine the aerodynamic performance of the Ventec roof: the so-called venturi-effect and the wind-blocking effect. These two effects should also be considered in future optimisation studies for different building and roof geometries, different surroundings and exhaust air flow rates.

Note that we have chosen to present the results in this paper as a function of the actual contraction height c, rather than as a function of a normalised/dimensionless contraction height value. The reason is that it is not yet clear which geometrical parameter is a suitable length scale for normalisation. Ideally, such a length scale would need to somehow represent both the dimensions of the roof and the dimensions of the building, because both set of dimensions are expected to play an important role in the aerodynamic performance of the roof. This is a topic of further analysis in future studies.

The evaluation of the aerodynamic performance of the roof has been mainly conducted based on the value of the negative pressure coefficient at point E. However, as mentioned in section 6.2, large pressure gradients are present in the roof contraction. Point E was chosen because of its position in the centre of the contraction, and because it corresponded to the location of the point measurement in the wind tunnel model. A future study on the aerodynamic performance of the roof will include modelling the exhaust flow rate through the vertical channel, and that enters the roof contraction due to the generated negative pressure.

9. Conclusions

This paper has presented a computational analysis of the aerodynamic performance of a venturi-shaped roof for natural ventilation of buildings, from the viewpoint of the two main governing effects: the so-called venturi-effect and the wind-blocking effect. The analysis has been performed with 3D steady Reynolds-averaged Navier-Stokes (RANS) CFD simulations with closure by the Renormalisation Group k-ε model. The CFD simulations have been based on a detailed grid-sensitivity analysis and on successful validation of the grid-independent results by comparison with experiments in an atmospheric boundary layer wind tunnel.

The aerodynamic performance of the roof has been evaluated in terms of the mean negative pressure generated in the narrowest part of the contraction. This negative pressure can be used to drive the natural ventilation of the building zones. The performance of the roof is determined by the balance between the so-called venturi-effect and the wind-blocking effect. Note that this paper has used the adjective “so-called” for venturi-effect because this effect strictly refers to confined flows, which is not the case in the present study. The wind-blocking effect refers to the resistance exerted by the roof contraction on the air flow and the resulting tendency of the approaching wind to flow around and over the roof, rather than only being forced through the roof.

The study has shown that due to the wind-blocking effect, the negative pressure in the roof does not monotonically decrease with increasing contraction height and that an optimum contraction height exists. The reason is that a smaller contraction height leads to a higher resistance for flow through the contraction, which causes more of the approaching wind to flow over and around the roof rather than through its narrow contraction. Due to this wind-blocking effect, the highest contraction ratio does not provide the best aerodynamic performance and the largest mean negative pressure, which is a counter-intuitive result.

The study in this paper has illustrated the use of CFD to increase insight in building aerodynamics and to support sustainable building design.

References

[1] Linden PF. The fluid mechanics of natural ventilation. Annu Rev Fluid Mech 1999;31: 201-238.

[2] Hunt GR, Linden PF. The fluid mechanics of natural ventilation - displacement ventilation by buoyancy-driven flows assisted by wind. Build Environ 1999;34(6): 707-720.

[3] Li YG, Delsante A. Natural ventilation induced by combined wind and thermal forces. Build Environ 2001;36(1): 59-71.

[4] Khan N, Su Y, Riffat SB. A review on wind driven ventilation techniques. Energy Build 2008;40(8), 1586-1604.
[5] Larsen TS, Heiselberg P. Single-sided natural ventilation driven by wind pressure and temperature difference. Energy Build 2008;40(6): 1031-1040.
[6] van Hooff T, Blocken B. Coupled urban wind flow and indoor natural ventilation modelling on a high-resolution grid: A case study for the Amsterdam ArenA stadium. Environ Modell Softw 2010;25(1): 51-65.
[7] Bronsema B. Earth, Wind & Fire – Air-conditioning powered by nature. 10th REHVA World Congress CLIMA 2010, 9-12 May, Antalya, Turkey.
[8] Chen Q. Ventilation performance prediction for buildings: A method overview and recent applications. Build Environ 2009;44(4) 848-858.
[9] Kato S, Murakami S, Mochida A, Akabayashi Shin-ichi, Tominaga Y. Velocity-pressure field of cross ventilation with open windows analyzed by wind tunnel and numerical simulation. J Wind Eng Ind Aerod 1992;44(1-3): 2575-2586.
[10] Kato S, Murakami S, Takahashi T, Gyobu T. Chained analysis of wind tunnel test and CFD on cross ventilation of large-scale market building. J Wind Eng Ind Aerod 1997;67-68: 573-587.
[11] Jiang Y, Alexander D, Jenkins H, Arthur R, Chen Q. Natural ventilation in buildings: Measurement in a wind tunnel and numerical simulation with large-eddy simulation. J Wind Eng Ind Aerod 2003;91(3) 331-353.
[12] Heiselberg P, Li Y, Andersen A, Bjerre M, Chen Z. Experimental and CFD evidence of multiple solutions in a naturally ventilated building. Indoor Air 2004;14(1): 43-54.
[13] Gao NP, Niu JL, Perino M, Heiselberg P. The airborne transmission of infection between flats in high-rise residential buildings: Tracer gas simulation. Build Environ 2008;43(11): 1805-1817.
[14] Tablada A, de Troyer F, Blocken B, Carmeliet J, Verschure H. On natural ventilation and thermal comfort in compact urban environments - the Old Havana case. Build Environ 2009;44(9): 1943-1958.
[15] Karava P, Stathopoulos T, Athienitis AK. Wind-induced natural ventilation analysis. Sol Energy 2007;81(1): 20-30.
[16] Bu Z, Kato S, Takahashi T. Wind tunnel experiments on wind-induced natural ventilation rate in residential basements with areaway space. Build Environ 2010;45(10): 2263-2272.
[17] Karava P, Stathopoulos T, Athienitis AK. Airflow assessment in cross-ventilated buildings with operable facade elements. Build Environ 2011;46(1): 266-279.
[18] Costola D, Blocken B, Hensen JLM. Overview of pressure coefficient data in building energy simulation and airflow network programs. Build Environ 2009;44(10): 2027-2036.
[19] Costola D, Blocken B, Ohba M, Hensen JLM. Uncertainty in airflow rate calculations due to the use of surface-averaged pressure coefficients. Energy Build 2010;42(6): 881-888.
[20] Norton T, Grant J, Fallon R, Sun DW. Assessing the ventilation effectiveness of naturally ventilated livestock buildings under wind dominated conditions using computational fluid dynamics. Biosystems Engineering 2009;103(1): 78-99.
[21] Norton T, Grant J, Fallon R, Sun DW. Optimising the ventilation configuration of naturally ventilated livestock buildings for improved indoor environmental homogeneity. Build Environ 2010;45(4): 983-995.
[22] van Hooff T, Blocken B. On the effect of wind direction and urban surroundings on natural ventilation of a large semi-enclosed stadium. Comput Fluids 2010;39(7): 1146-1155.
[23] van Hooff T, Blocken B, Aanen L, Bronsema B. A venturi-shaped roof for wind-induced natural ventilation of buildings: wind tunnel and CFD evaluation of different design configurations. Build Environ 2011. In press. doi:10.1016/j.buildenv.2011.02.009
[24] Blocken B, Stathopoulos T, Carmeliet J, Hensen JLM. Application of CFD in building performance simulation for the outdoor environment: an overview. Journal of Building Performance Simulation 2011; in press. doi: 10.1080/19401493.2010.513740
[25] Blocken B, Carmeliet J, Stathopoulos T. CFD evaluation of the wind speed conditions in passages between buildings – effect of wall-function roughness modifications on the atmospheric boundary layer flow. J Wind Eng Ind Aerod 2007;95(9-11): 941-962.
[26] Blocken B, Stathopoulos T, Carmeliet J. Wind environmental conditions in passages between two long narrow perpendicular buildings. J Aerospace Eng–ASCE 2008;21(4): 280-287.
[27] Blocken B, Stathopoulos T, Carmeliet J. A numerical study on the existence of the Venturi-effect in passages between perpendicular buildings. J Eng Mech-ASCE 2008;134(12): 1021-1028.
[28] Venturi GB. Experimental enquiries concerning the principle of the lateral communication of motion in fluids: applied to the explanation of various hydraulic phenomena. 1799. Translated from the French by Nicholson W, 1st English ed., J. Taylor, Architectural Library, High-Holborn, London.
[29] Gandemer J. Wind environment around buildings: aerodynamic concepts. Proc., 4th Int. Conf. Wind Effects on Buildings and Structures, Heathrow 1975, Cambridge University Press, 423-432.
[30] Lawson TV. Wind effects on buildings, Vol. 1, 1980, Applied Science Publishers Ltd., London, England.

[31] Dutt AJ. Wind flow in an urban environment. Environ. Monit. Assess. 1991;19(1-3): 495-506.
[32] Franke J, Hellsten A, Schlünzen H, Carissimo B (Eds.). Best practice guideline for the CFD simulation of flows in the urban environment. COST Office Brussels; 2007.
[33] Tominaga Y, Mochida A, Yoshie R, Kataoka H, Nozu T, Yoshikawa M, Shirasawa T. AIJ guidelines for practical applications of CFD to pedestrian wind environment around buildings. J Wind Eng Ind Aerod 2008;96(10-11): 1749-61.
[34] van Hooff T, Blocken B, van Harten M. 3D CFD simulations of wind flow and wind-driven rain shelter in sports stadia: influence of stadium geometry. Build Environ 2011;46(1): 22-37.
[35] Launder BE, Spalding DB, The numerical computation of turbulent flows. Comput Method Appl M 1974;3: 269-289.
[36] Cebeci T, Bradshaw P. Momentum transfer in boundary layers, Hemisphere Publishing Corporation; 1977.
[37] Fluent Inc. Fluent 6.3. User's Guide. Fluent Inc., Lebanon; 2006.
[38] Blocken B, Stathopoulos T, Carmeliet J. CFD simulation of the atmospheric boundary layer: wall function problems. Atmos Environ 2007;41(2): 238-252.
[39] Yakhot V, Orszag SA, Thangam S, Gatski TB, Speziale CG. Development of turbulence models for shear flows by a double expansion technique. Physics of Fluids 1992;A4: 1510-1520.
[40] Evola G, Popov V. Computational analysis of wind driven natural ventilation in buildings. Energy Build 2006;38(5): 491-501.

Table 1. Parameters c (contraction height), b and b/c (contraction ratio) for the six different configurations.

c (m)	0.25	0.375	0.5	0.75	1	2
b (m)	4.25	4.375	4.5	4.75	5	6
b/c	17.0	11.7	9.0	6.3	5.0	3.0

FIGURES

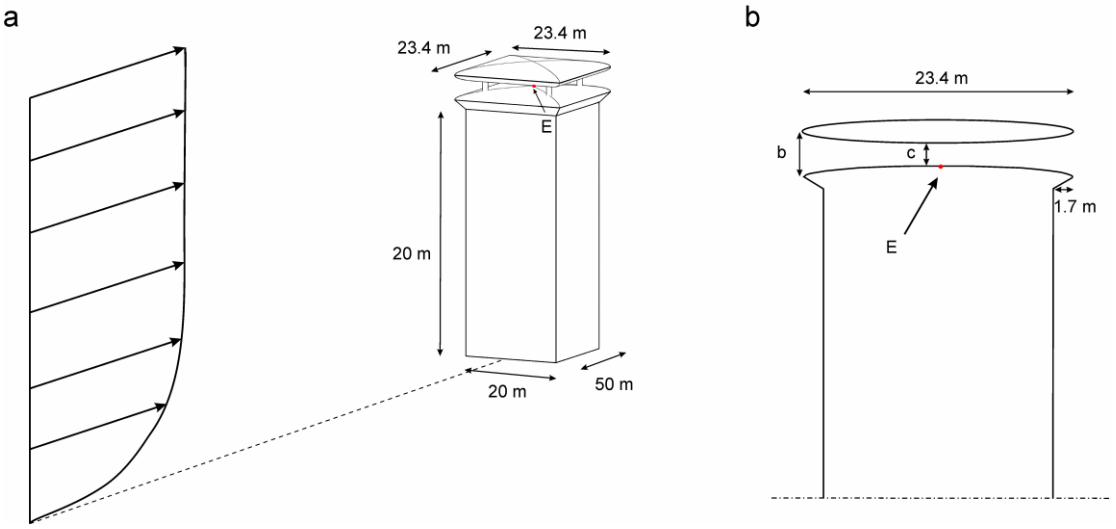

Figure 1: (a) Perspective view of the building with venturi-shaped roof (Ventec roof) and main dimensions. (b) Vertical cross-section of the building and Ventec roof with indication of parameters b and c and position E where the surface pressure is evaluated.

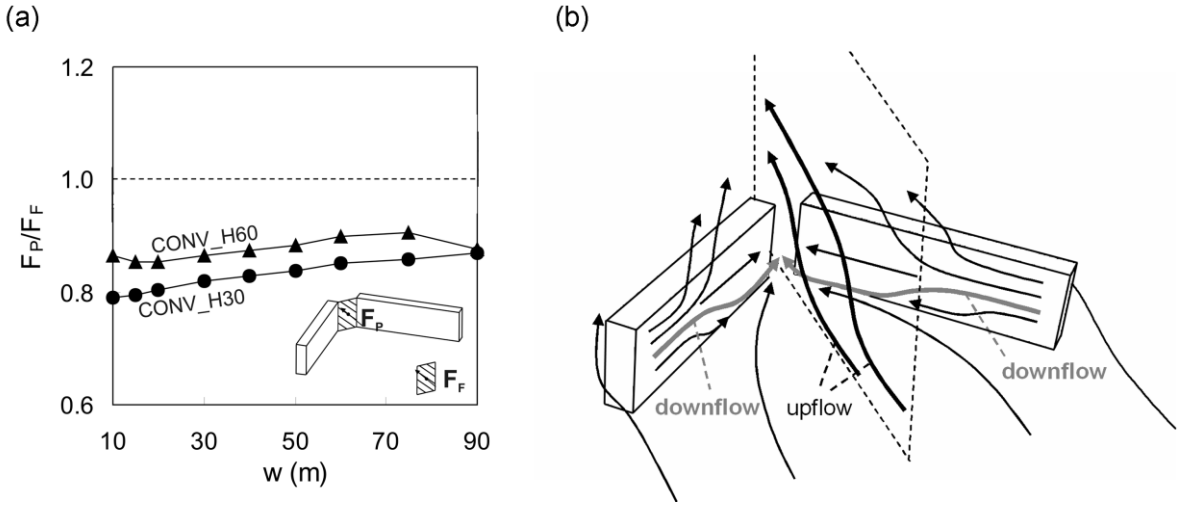

Figure 2: Illustration of the wind-blocking effect for a converging arrangement of two high-rise buildings (a) Ratio of the passage flux F_P to the free-field flux F_F for buildings with height H = 30 m and H = 60 m, and for different passage widths w (from [26]). (b) Schematic representation of flow in the converging passage with H = 30 m and w = 10 m. The vertical plane cuts midway through the passage. The upflow due to the wind-blocking effect is responsible for the fact that the ratio F_P/F_F is smaller than 1 (from ([26]).

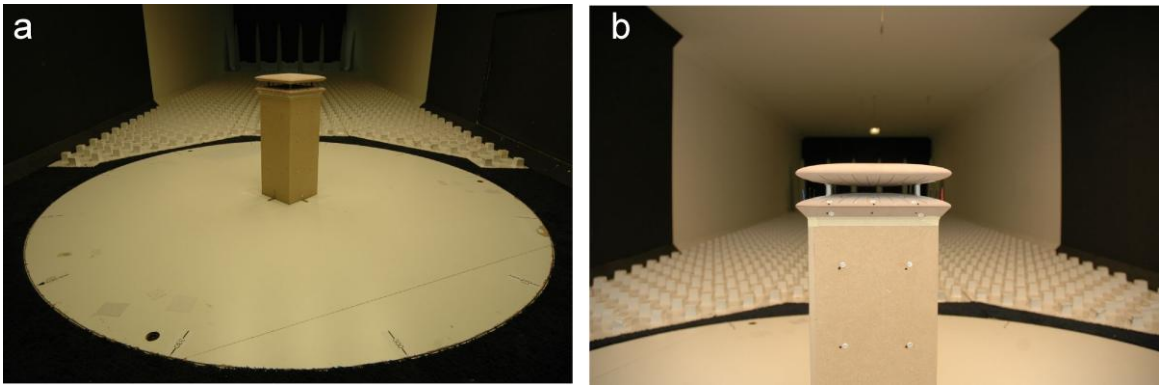

Figure 3: Pictures of the reduced-scale building model with Ventec roof in the closed-circuit ABL wind tunnel at Peutz BV. (a) View of the upstream domain with building model positioned in the middle of the turntable for wind direction of 45°. (b) Close-up view of the building model with Ventec roof.

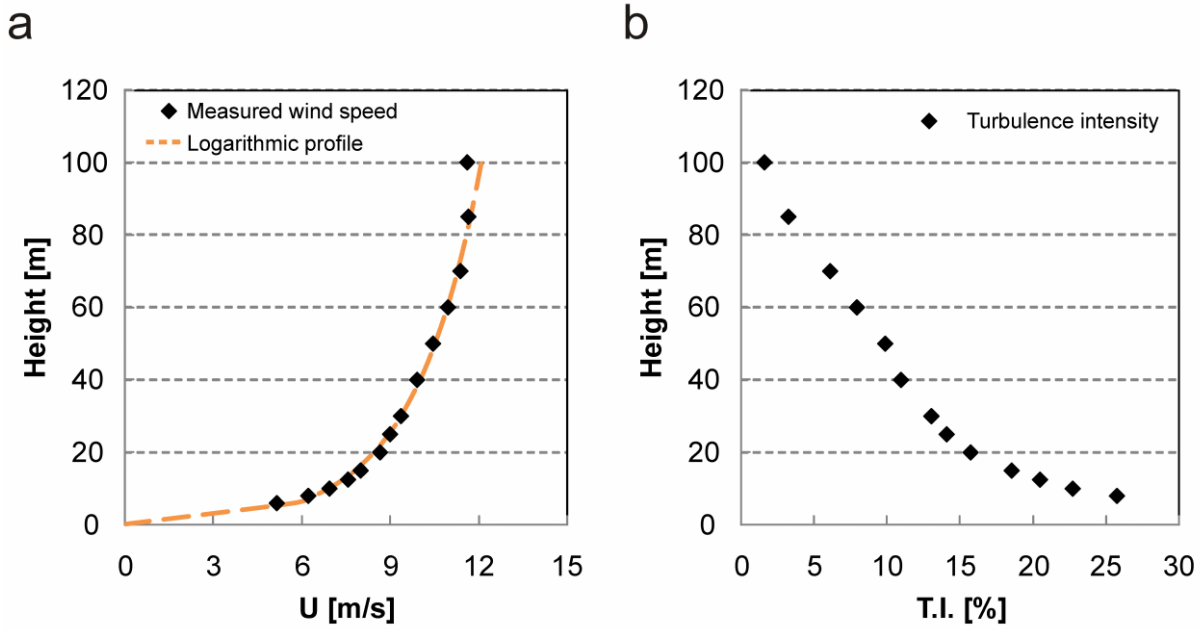

Figure 4: (a) Measured approach-flow mean wind speed profile along a vertical line at the upstream edge of the turntable (full-scale dimensions; log law profile with u* = 0.956 m/s and y_0 = 0.5 m). (b) Measured turbulence intensity T.I. along the same vertical line (full-scale dimensions).

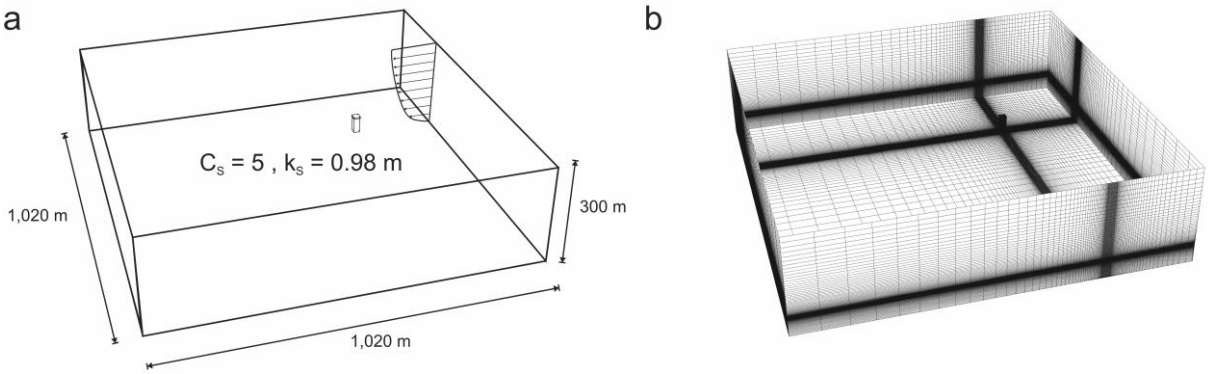

Figure 5: (a) Perspective view of the building in its computational domain (full-scale dimensions and parameter values). (b) View of the computational grid at the building and some of the domain surfaces.

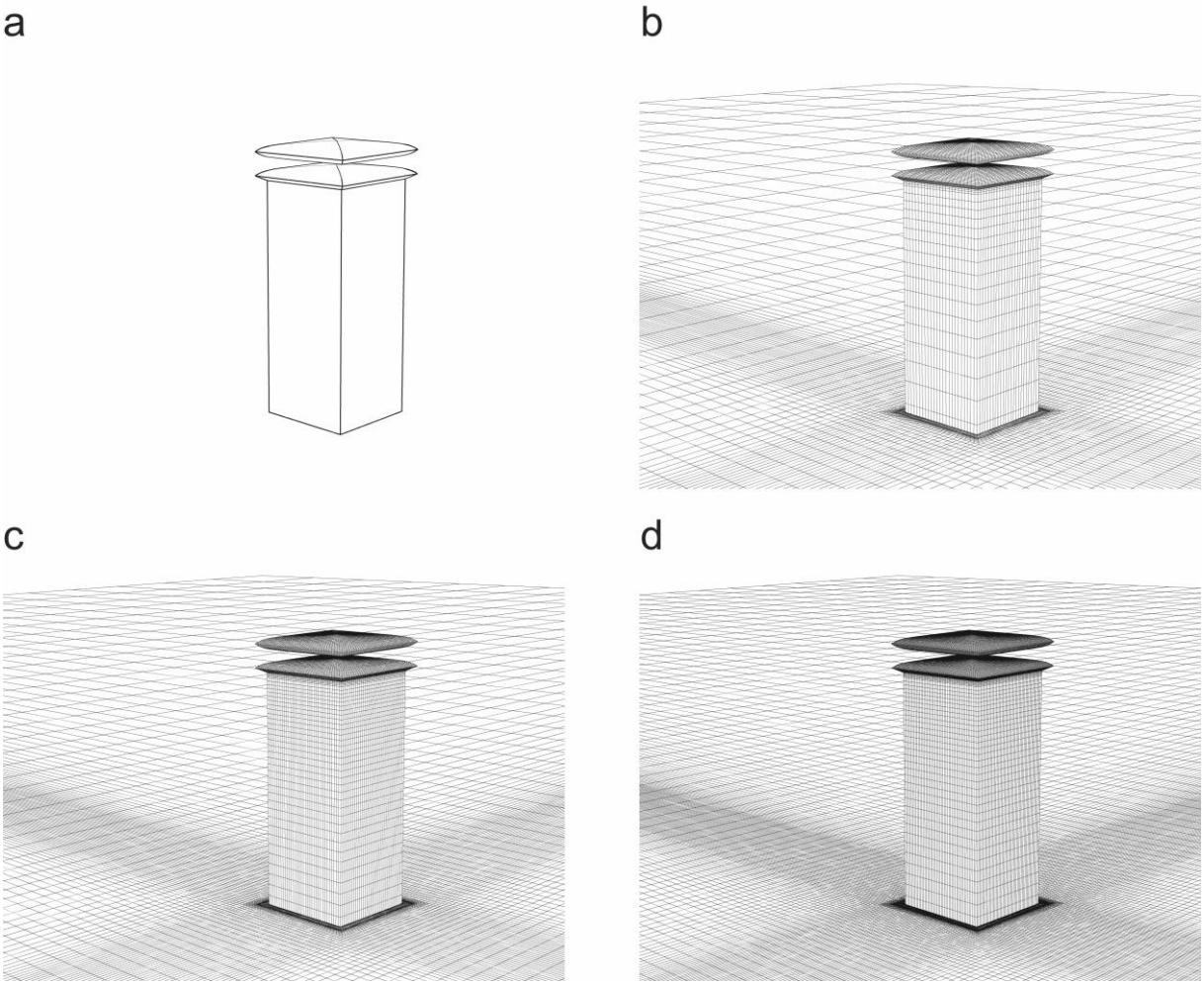

Figure 6. Geometry and perspective view of computational grids for configuration with c = 1. (a) Geometry. (b-d) Computational grids used for the grid-sensitivity analysis: (b) coarse grid (549,380 cells); (c) middle grid (2,041,268 cells); (d) fine grid (4,364,688 cells).

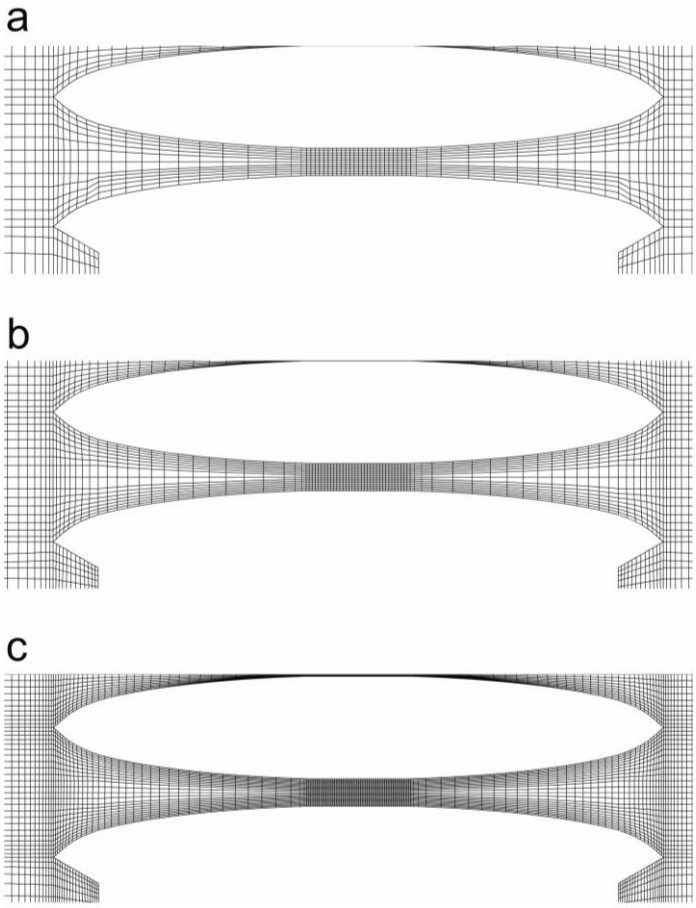

Figure 7. Computational grids in the vertical cross-section of the roof contraction for configuration with c = 1. (a) coarse grid (549,380 cells); (b) middle grid (2,041,268 cells); (c) fine grid (4,364,688 cells).

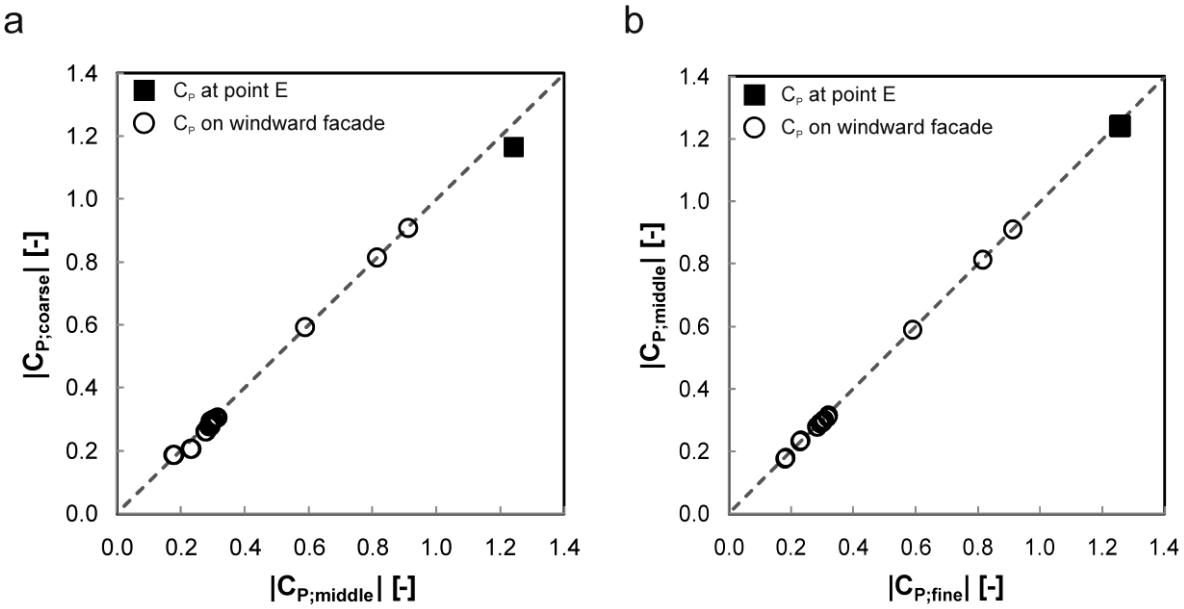

Figure 8. Grid-sensitivity analysis: comparison of pressure coefficients on windward facade and at position E in roof contraction with c = 1 m for different grids: (a) coarse grid versus middle grid and (b) middle grid versus fine grid.

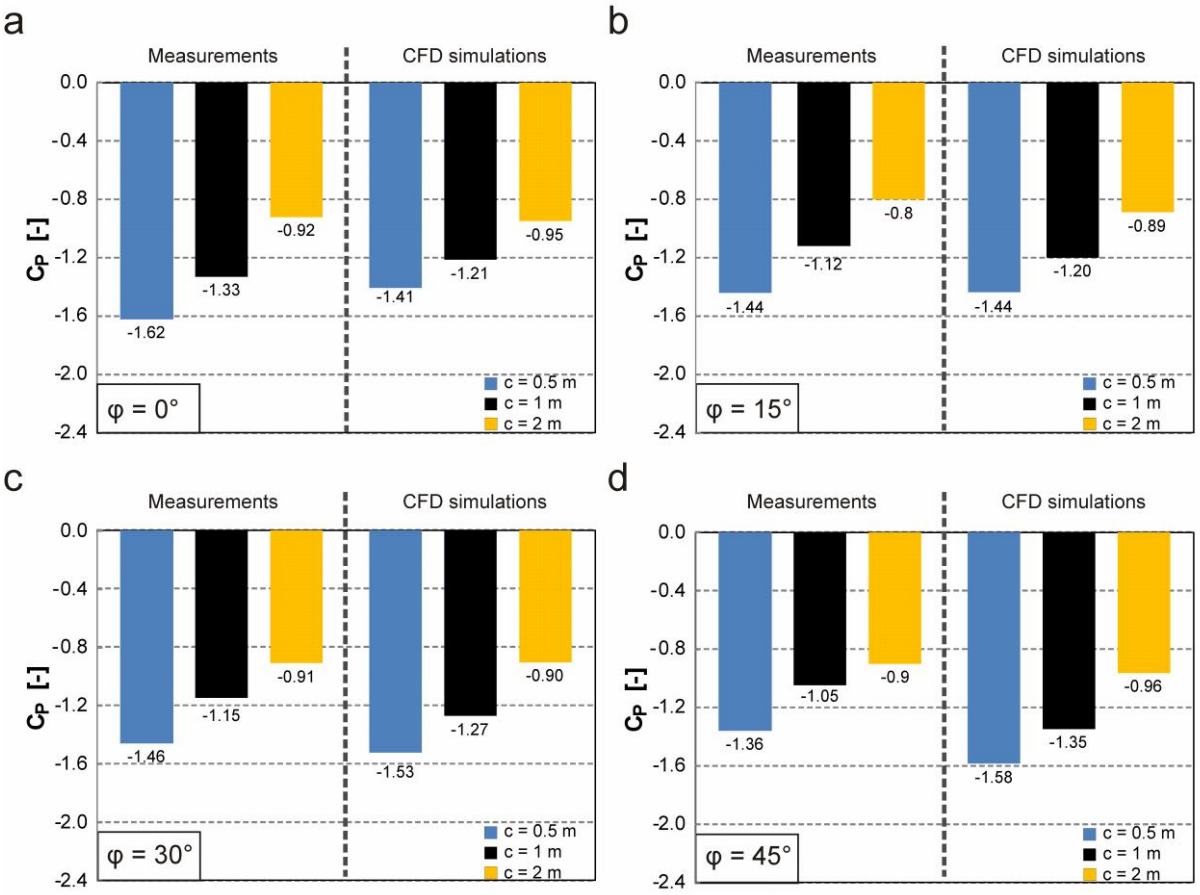

Figure 9. Experimental validation: comparison between measurements and CFD simulation results of pressure coefficients at position E for three contraction heights (c = 0.5 m, c = 1 m and c = 2 m) and four wind directions. (a) φ = 0°; (b) φ = 15°; (c) φ = 30°; (d) φ = 45°.

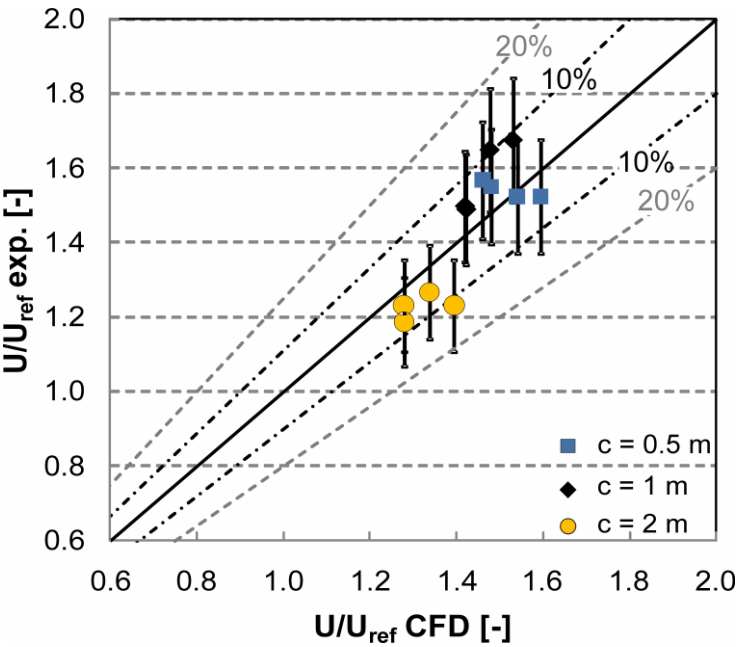

Figure 10. Experimental validation: comparison between measurements (exp.) and CFD simulation results of velocity ratio U/U_{ref} at mid-height in the centre of the roof contraction for three contraction heights (c = 0.5 m, c = 1 m and c = 2 m) and four wind directions (φ = 0°; 15°; 30°; 45°). The error bars represent the measuring accuracy of ±10%.

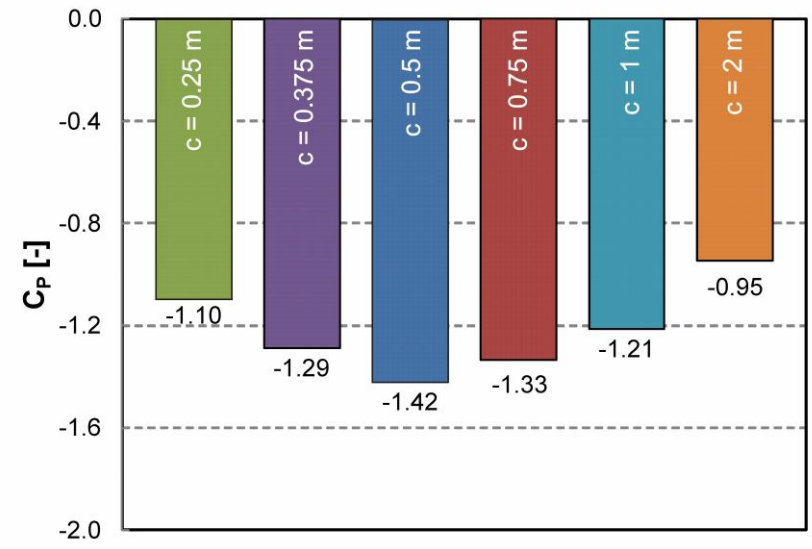

Figure 11. Optimisation results: mean pressure coefficients C_P at position E for wind direction $\varphi = 0°$ and for six different values of the contraction height c. The largest negative pressure is obtained for c = 0.5 m.

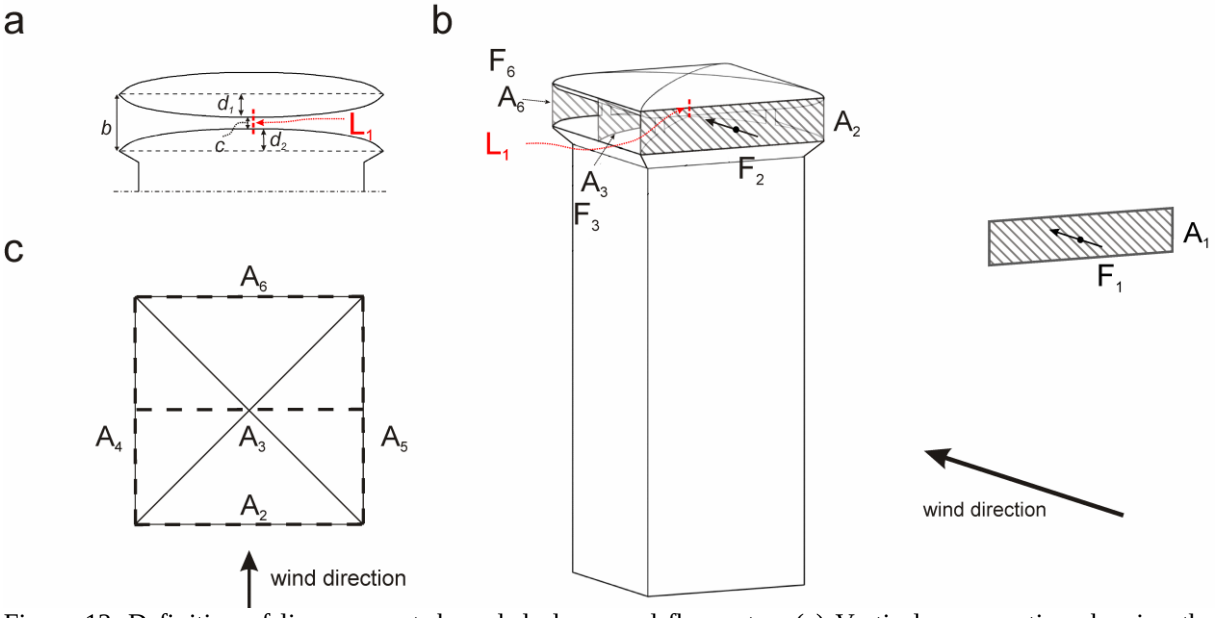

Figure 12. Definition of line segment, bounded planes and flow rates: (a) Vertical cross-section showing the vertical line segment L in the middle of the contraction. (b) Indication of the fee-field plane A_1 and the roof vertical bounded planes A_2, A_3 and A_6 and the vertical line segment L. (c) Top view of roof with indication of the roof vertical planes A_2 to A_6.

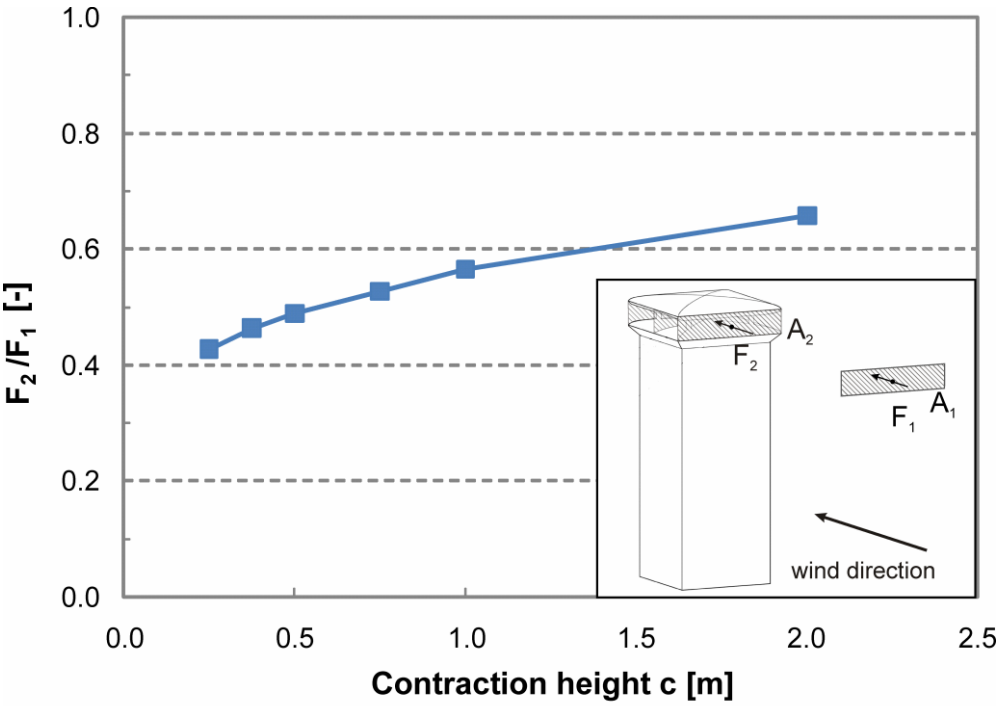

Figure 13. Ratio of flow rate F_2 (through inlet plane A_2) to flow rate F_1 (through free-field plane A_1) as a function of the contraction height c.

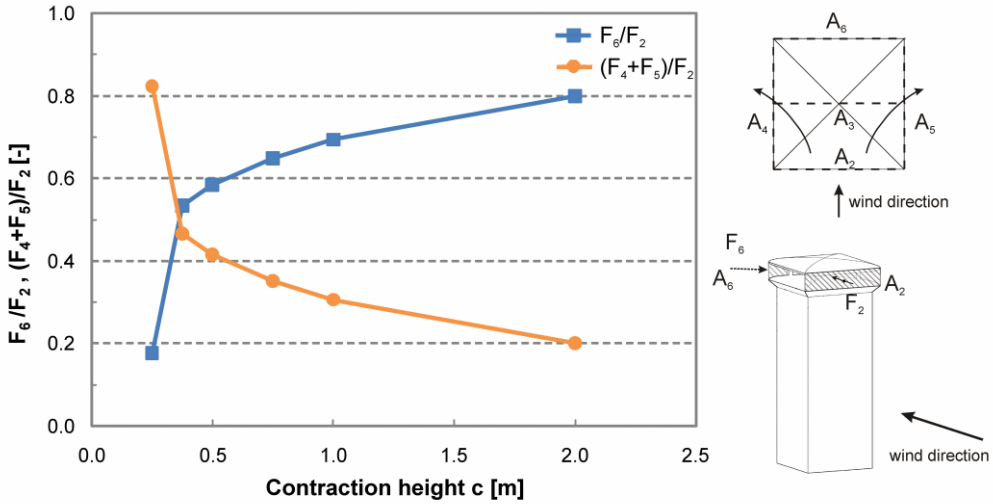

Figure 14. Ratio of F_6 (through roof outlet plane) to F_2 (through roof inlet plane) as function of the contraction height c and ratio of flow rates F_4+F_5 (through roof side planes) to flow rate F_2. The sum of the two curves is equal to one.

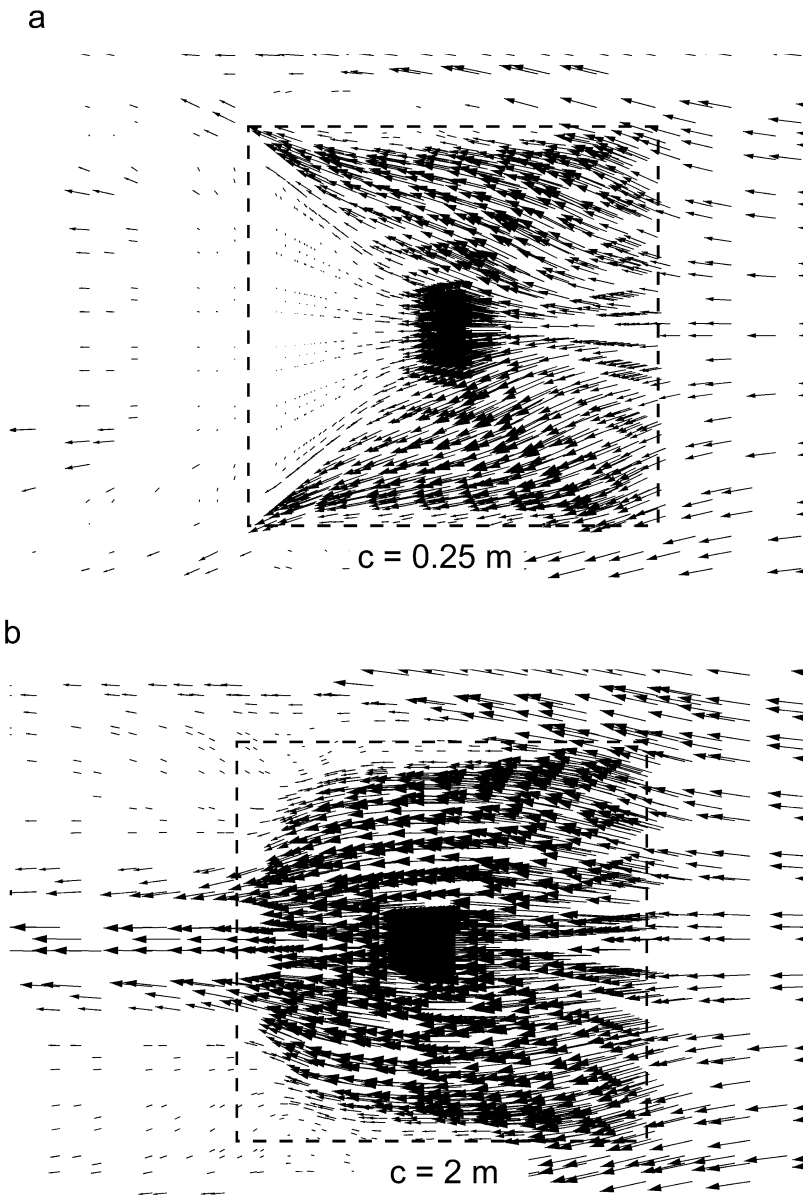

Figure 15. Velocity vectors in a horizontal plane in the middle of the roof contraction for φ = 0° and for (a) c = 0.25 m and (b) c = 2 m, illustrating the presence of a strong wind-blocking effect for lower c-values.

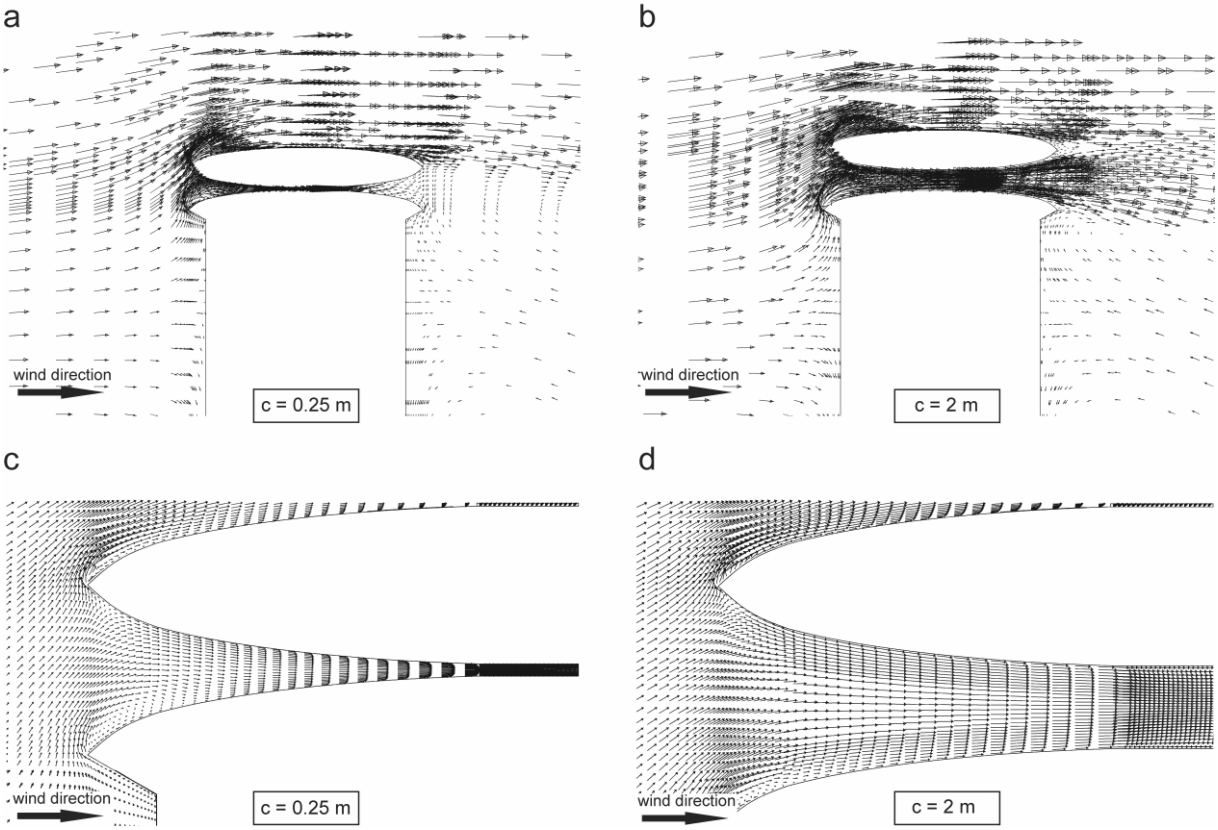

Figure 16. Velocity vectors in the vertical centre plane for φ = 0°, illustrating the presence of a strong wind-blocking effect for lower c-values; (a) c = 0.25 m; (b) c = 2 m; (c) c = 0.25 m; (d) c = 2 m.

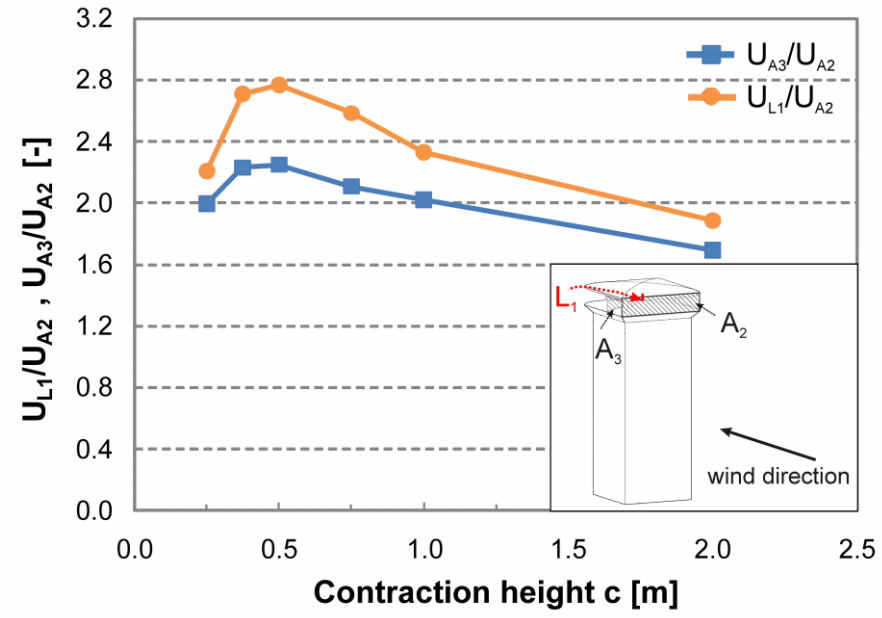

Figure 17. Average velocity ratios as function of the contraction height c: average velocity U_{A3} through plane A_3 to average velocity U_{A2} through A_2, and average velocity U_{L1} along line segment L_1 to U_{A2}. The figure shows the acceleration of the flow due to the roof contraction. The highest acceleration is present for c = 0.5 m; both smaller and larger contraction heights result in smaller flow accelerations.

van Hooff T, Blocken B, Aanen L, Bronsema B. 2012. Numerical analysis of the performance of a venturi-shaped roof for natural ventilation: influence of building width. ***Journal of Wind Engineering and Industrial Aerodynamics*** *104-106: 419-427.*

Numerical analysis of the performance of a venturi-shaped roof for natural ventilation: influence of building width

T. van Hooff * [a,b], B. Blocken [a], L. Aanen [c] , B. Bronsema [d]

(a) Building Physics and Services, Eindhoven University of Technology, P.O. box 513, 5600 MB Eindhoven, the Netherlands
(b) Division of Building Physics, Department of Civil Engineering, Katholieke Universiteit Leuven, Kasteelpark Arenberg 40, P.O. Box 2447, 3001 Leuven, Belgium
(c) Peutz BV, P.O. box 66, 6585 ZH, Mook, The Netherlands
(d) Faculty of Architecture – Department of Climate Design, Delft University of Technology, Prof. Boerhaaveweg 37, 2251 HX Voorschoten, The Netherlands

Graphical abstract

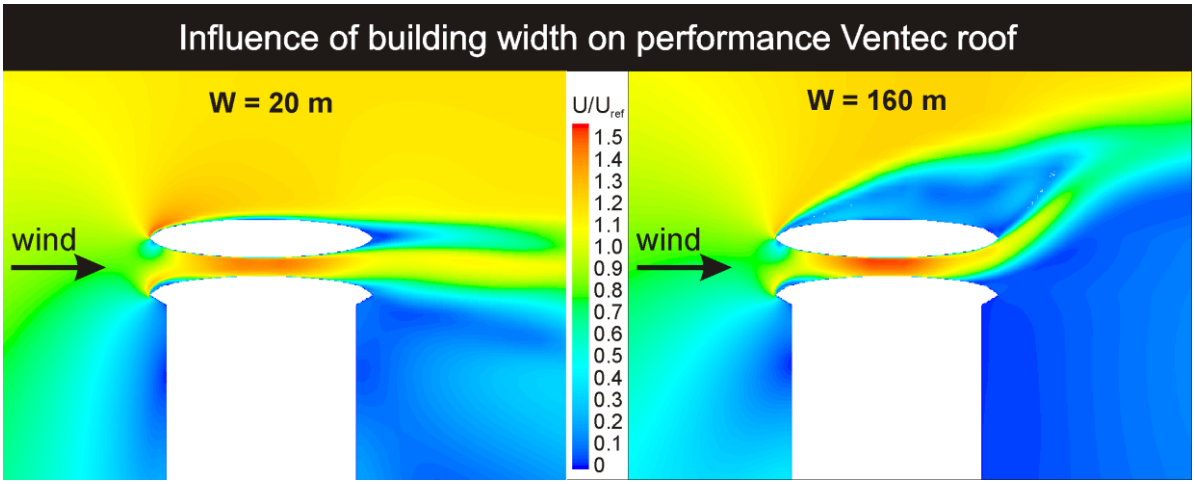

Highlights

- Venturi-shaped roof can improve natural ventilation potential of buildings
- Building geometry influences roof performance
- 3D steady RANS study of influence of building width on roof performance
- Five building widths tested: 20, 40, 80, 120, 160 m
- Increasing building width leads to increased performance due to changed static pressure fields

* **Corresponding author**: Twan van Hooff, Building Physics and Services, Eindhoven University of Technology, P.O.Box 513, 5600 MB Eindhoven, the Netherlands. Tel.: +31 (0)40 247 5877, Fax +31 (0)40 243 8595
E-mail address: t.a.j.v.hooff@tue.nl

van Hooff T, Blocken B, Aanen L, Bronsema B. 2012. Numerical analysis of the performance of a venturi-shaped roof for natural ventilation: influence of building width. ***Journal of Wind Engineering and Industrial Aerodynamics*** *104-106: 419-427.*

Numerical analysis of the performance of a venturi-shaped roof for natural ventilation: influence of building width

T. van Hooff * [a,b], B. Blocken [a], L. Aanen [c] , B. Bronsema [d]

(a) Building Physics and Services, Eindhoven University of Technology, P.O. box 513, 5600 MB Eindhoven, the Netherlands
(b) Division of Building Physics, Department of Civil Engineering, Katholieke Universiteit Leuven, Kasteelpark Arenberg 40, P.O. Box 2447, 3001 Leuven, Belgium
(c) Peutz BV, P.O. box 66, 6585 ZH, Mook, The Netherlands
(d) Faculty of Architecture – Department of Climate Design, Delft University of Technology, Prof. Boerhaaveweg 37, 2251 HX Voorschoten, The Netherlands

Abstract

A numerical analysis with Computational Fluid Dynamics (CFD) is performed to investigate the influence of building width on the performance of a venturi-shaped roof (called Ventec roof) for natural ventilation. The specific roof configuration is intended to create an underpressure in the narrowest roof section (contraction) which can be used to partly or completely drive the natural ventilation of the building zones. In previous studies, the influence of the roof configuration on its performance was analysed in detail, however these studies were all performed for a fixed building geometry, i.e. a tower building with floor plan 20 x 20 m² and a height of 50 m. It is important to analyse the performance of the Ventec roof for different building widths. Therefore, the present paper presents CFD simulations for building (and roof) widths of 20, 40, 80, 120 and 160 m. The 3D steady Reynolds-averaged Navier-Stokes (RANS) approach with the Renormalization Group (RNG) k-ε model is used. The simulations are based on grid-sensitivity analysis and on validation by comparison with wind tunnel experiments. The simulations show that the aerodynamic performance of the roof in terms of the underpressure in the contraction improves with 31% when the building width is increased from 20 m to 40 m, while further increasing the building width only provides relatively small additional improvements. The increased performance with increasing building width is attributed to the larger overpressure upstream of the building and to the larger underpressure and larger size (height) of the wake behind the building.

Keywords: Computational Fluid Dynamics (CFD); building dimensions; natural ventilation; venturi-effect; buildings; airflow

1. Introduction

Natural ventilation or hybrid natural-mechanical ventilation of buildings can be used to provide a comfortable and healthy indoor environment with reduced energy consumption. Natural ventilation is based on either wind-induced pressure differences or thermally-induced pressure differences, or – most often – a combination of both (Linden 1999, Hunt and Linden 1999, Li and Delsante 2001, Larsen and Heiselberg 2008, Chen 2009, van Hooff and Blocken 2010, Bronsema 2010). The potential for natural ventilation can be significantly enhanced by the design of the building. Because the highest wind speeds are often present at building roof revel, in particular the roof geometry can be employed to enhance natural ventilation. This reasoning has driven the design of a specific venturi-shaped roof by Bronsema in the framework of the research project "Earth, Wind & Fire – Air-conditioning powered by Nature" (Bronsema 2010) (Fig. 1). This roof is called the Ventec roof. It consists of a disk-shaped roof construction that is positioned at a certain height above the actual building, creating a contraction that is expected to provide significant underpressures due to the so-called Venturi-effect. The underpressure can be used to partly or completely drive the natural ventilation of the building zones. For this purpose, a vertical channel (not shown in Fig. 1) is provided in the centre of the building, which connects point E of the roof contraction with the building zones at each floor.

* **Corresponding author**: Twan van Hooff, Building Physics and Services, Eindhoven University of Technology, P.O.Box 513, 5600 MB Eindhoven, the Netherlands. Tel.: +31 (0)40 247 5877, Fax +31 (0)40 243 8595
E-mail address: t.a.j.v.hooff@tue.nl

In a previous paper (van Hooff et al. 2011), the present authors provided a first analysis of the aerodynamic performance of this roof design by CFD and wind tunnel experiments. At this stage, it was found that adding vertical guiding vanes in the roof contraction actually did not improve but cancelled the effect of the contraction. Additional research (Blocken et al. 2011) indicated that due to the guiding vanes, the flow resistance through the contraction became too large and that therefore the oncoming wind would flow over and around the roof and the building, rather than being forced to flow between and along the guiding vanes in the contraction. This phenomenon was called the "wind-blocking effect" in earlier studies (Blocken et al. 2007a, 2008a, 2008b). To further optimize the roof performance, the venturi-effect and the wind-blocking effect were analysed in detail as a function of the roof contraction height and the contraction ratio (Blocken et al. 2011). However, these studies were all performed for a fixed building geometry, i.e. a tower building with floor plan 20 x 20 m² and a height of 50 m. It is not clear how the building geometry influences the performance of the roof, therefore it is important to analyse the performance of the Ventec roof for different building widths.

In the present study, 3D steady Reynolds-averaged Navier-Stokes (RANS) CFD with the Renormalization Group (RNG) k-ε model is used to investigate the influence of the building width on the performance of the roof, in terms of the underpressure in the contraction. Simulations are performed for building widths of 20, 40, 80, 120 and 160 m. Also the width of the roof is adjusted, to match the building width. Section 2 describes the building and roof geometry. Section 3 presents the CFD analysis for the basic configuration, including the grid-sensitivity analysis and the validation with the wind tunnel experiments. In section 4, the influence of the building width on the roof performance is analysed. Finally, sections 5 (discussion) and 6 (conclusions) conclude the paper.

2. Description of building and roof geometry

Figure 1 illustrates the basic geometry of the building with the venturi-shaped roof. The building has a rectangular (20 x 20 m²) floor plan and a height of 50 m, measured up to the edge of the roof. The Ventec roof consists of two parts. The lower part is constructed from half a "square disk" with dimensions 23.4 m x 23.4 m x 2 m (L x W x H) and it is positioned directly on top of the building, this way creating a roof overhang of 1.7 m on each side of the building, at which ventilation inlets will be placed. At a distance 'c' (contraction height) above this part of the roof a "full square disk" is positioned with dimensions 23.4 m x 23.4 m x 4 m (L x W x H), resulting in a nozzle-shaped roof entrance from all four sides of the building. This part can be supported by a set of slender vertical columns. In the present study, the inlet height b = 6 m and the contraction height c = 2 m. The additional building and roof configurations are generated by applying a geometrical scaling factor to the building and roof width. The scaling factors are 2, 4, 6 and 8, yielding building widths W = 40 m, 80 m, 120 m and 160 m, respectively.

The position of main interest inside the roof contraction is the point in the bottom centre of the roof, indicated with the letter E (from "exhaust") in Figure 1a and b. In this study, the exhaust is considered to be closed and the surface pressure at this position, as well as at the entire roof surface, will be evaluated. All simulations are conducted for an isolated building, i.e. without surrounding buildings. Therefore, all differences in wind speed and surface pressures between the different geometries are only due to changes in the width of the building and the roof.

3. Analysis of roof performance for the basic geometry

3.1. Wind tunnel measurements

Wind tunnel measurements were performed to validate the CFD simulations. A reduced-scale model (1:100) of the basic geometry (building width W = 20 m) was tested in the closed-circuit atmospheric boundary layer (ABL) wind tunnel at Peutz BV in Mook, the Netherlands. The dimensions of the wind tunnel test section are 3.2 x 1.8 m^2 (width x height), resulting in a blockage ratio of about 2%. The surface pressure was measured at position E (Fig. 1) with a HCLA12X5EB amplified differential pressure sensor from Sensortechnics. The wind speed in the roof contraction was measured in the centre of the contraction, at mid-height, using a NTC resistor element. The NTCs are operated with a constant current and are calibrated by Peutz by determining the relationship between wind speed and temperature (and corresponding resistance) of each individual probe. The probes are not direction-sensitive and due to the relatively long reaction time of the probes, only average wind speeds can be measured, with an accuracy of ±10%. Approach-flow vertical profiles of mean wind speed U and turbulence intensity I_u are measured at the edge of the turntable using hot-wire anemometers and are presented in Figure 2. The measured wind speed profile can be described by a logarithmic law with a friction velocity u^* = 0.956 m/s and an aerodynamic roughness length y_0 = 0.005 m (full scale: y_0 = 0.5 m). The incident reference wind speed at roof height (full scale: 50 m; reduced scale: 0.5 m) U_{ref} is 10.5 m/s. Measurements are made for

four wind directions: φ = 0°, 15°, 30° and 45°, taking into account the symmetry of the building and the venturi-shaped roof.

3.2. Computational geometry and grid

The computational domain has (full-scale) dimensions L x B x H = 1020 m x 1020 m x 300 m (Fig. 3a). This domain shape allows modelling different wind directions (0° to 45°). The distance from the inlet, the lateral boundaries and the top boundary is at least 5H away from the building, with H the building height (= 50 m) (Franke et al. 2004, 2007, Tominaga et al. 2008). Franke et al. (2004) recommend a maximal blockage ratio of 3% for buildings with a width that is much larger than the height. The blockage ratio for the case with W = 160 m is 0.3%, which is far below the recommended maximum. The flow field upstream of the building was checked to ensure a proper flow development in this region. The outlet is positioned at a distance of 15H to allow full flow development behind the building. A high-resolution computational grid was constructed based on a grid-sensitivity analysis (see Fig. 3b and Fig. 4). The grid-sensitivity analysis is reported in (van Hooff et al. 2011) and (Blocken et al. 2011). The grid has at least 10 cells between each two adjacent surfaces as requested by the best practice guidelines by Franke et al. (2007) and Tominaga et al. (2008). The grid was generated using the grid generation technique presented by van Hooff and Blocken (2010), by which the geometry and the grid are created simultaneously by a series of extrusion operations. Note that the grids do not contain any pyramidal or tetrahedral cells. A high grid resolution is applied in the proximity of the roof in view of the expected large flow gradients (Fig. 4). The grid has a total of 2,375,016 cells and the y^+ values in the roof contraction are around 2,000.

3.3. Boundary conditions

At the inlet of the domain the measured approach-flow mean wind speed profile is imposed. Turbulent kinetic energy k is calculated from the turbulence intensity I_u using $k = 0.5(I_u.U)^2$. The turbulence dissipation rate $\varepsilon = (u^*)^3/\kappa(y+y_0)$, where y is the height coordinate, κ the von Karman constant (κ = 0.42) and u* the friction velocity related to the logarithmic mean wind speed profile. At the ground and building surfaces, the standard wall functions by Launder and Spalding (1974) are used with the sand-grain based roughness modification by Cebeci and Bradshaw (1977). For the ground surface, the parameters k_S and C_S, to be used in Fluent (Fluent Inc. 2006) should be selected to represent the rough fetch upstream of the building model. Therefore, k_S and C_S have to be determined using their appropriate consistency relationship with y_0. This relationship was derived by Blocken et al. (2007b) for Fluent and CFX. For Fluent 6, up to at least version 6.3, it is given by $k_S = 9.793y_0/C_S$. The combination k_S = 0.98 m and C_S = 5 is selected. The building surfaces are assumed to be smooth (k_S = 0 m and C_S = 0.5). Zero static pressure is imposed at the outlet of the domain and the top of the domain is modelled as a slip wall (zero normal velocity and zero normal gradients of all variables).

3.4. Solver settings

The 3D steady RANS equations are solved in combination with the RNG k-ε turbulence model (Yakhot et al. 1992) using Fluent 6.3.26. The RNG k-ε turbulence model was chosen because of its good performance in predicting the surface pressures on the windward building facades and in the roof opening in the previous study (van Hooff et al. 2011) and because of its superior performance in an earlier study by Evola and Popov (2006). Pressure-velocity coupling is taken care of by the SIMPLE algorithm, pressure interpolation is standard and second-order discretization schemes are used for both the convection terms and the viscous terms of the governing equations. Convergence has been monitored carefully and the iterations have been terminated when all scaled residuals showed no further reduction with increasing number of iterations. At this stage, the scaled residuals (Fluent Inc. 2006) were: 10^{-4} for continuity, 10^{-7} for momentum, 10^{-6} for turbulent kinetic energy and 10^{-4} for turbulence dissipation rate.

3.5. Results and validation

Figure 5 compares the results from the wind tunnel measurements and the results from the CFD simulations. Figure 5a shows the pressure coefficients C_p at point E, which are defined as $C_p = (P-P_0)/(0.5\rho U_{ref}^2)$, where P is the local static pressure, P_0 the reference static pressure, ρ the air density and U_{ref} the approach-flow wind speed at building height(= 50 m). Fig. 5b provides a similar comparison for the dimensionless velocity magnitude (U/U_{ref}) at mid-height in the centre of the roof contraction. Note that in this ratio, U is the magnitude of the 3D velocity vector. Figure 5 shows that the aerodynamic performance of the roof is almost independent of the wind direction φ. The differences in measured and simulated values of the pressure coefficients C_P and the dimensionless velocity magnitudes U/U_{ref} between the four wind directions φ are in general less than 10%, with

no clear tendency towards an optimal wind direction. In general a good agreement is obtained, where the CFD results are within 10%-15% of the measurements. Based on this validation study, the influence of building width is investigated in the next section.

4. Analysis of roof performance for different building widths

4.1. Computational settings and parameters

The geometry and the grid for the different building widths are obtained by applying a linear scaling factor along the width of the building. The resulting geometries are shown in Fig. 6. The resulting computational grids are illustrated in Fig. 7. The boundary conditions and solver settings are identical to those outlined in the previous section. However, simulations are only performed for one wind direction, i.e. perpendicular to the wide facade of the building ($\varphi = 0°$).

4.2. Results

Fig. 8a displays the pressure coefficient C_p at point E as a function of the building width W. When W increases from 20 m to 40 m, the C_p value improves (i.e. decreases) with about 31% to a value of -1.24. Further increasing W leads to additional, but smaller improvements, down to C_p = -1.38 for W = 160 m. Fig. 8b shows the corresponding dimensionless velocity magnitude (U/U_{ref}) at mid-height in the centre of the roof contraction. Fig. 9 displays the same parameter U/U_{ref} in the vertical centre plane through the building. As W increases, so does the area of low wind speed (stagnation zone) upstream of the building. In addition, also the size (height) of the wake behind the building increases. These observations and their effect on the flow through the roof are more clearly shown in Fig. 10. It appears that the increase of the stagnation zone in front of the building and the increase of the size of the wake and the underpressure value in the wake are responsible for the increase in underpressure at point E and therefore for the improved performance of the roof with increasing building width. Note that the velocity contours in the wake of the building and above the roof of the building do not show a clear trend with increasing width; the direction of the jet that exits the venture-shaped roof as well as the shape of the recirculation zone above the roof vary with building width. The absence of a clear trend in the flow pattern in these regions is the result of a minor oscillatory convergence that was observed for the simulations, which was also reported by Ramponi and Blocken (2012) for a different study. The oscillatory convergence was caused by oscillatory behaviour of the flow pattern in the wake of the building and above the building; slightly different flow patterns were present in these regions depending on the number of iterations before the simulation was terminated. However, these oscillations primarily affected the aforementioned two regions. By monitoring the velocity and pressure inside the roof contraction it was determined that the influence of the oscillatory convergence on the studied parameters inside the roof was negligible; the velocity fluctuations and pressure fluctuations were within 1% and 2% of the mean value, respectively.

Figs. 11a-d show the ratio U/U_{ref} and the static pressure P along a horizontal line through the roof contraction, as shown in Fig. 11e. In Figs. 11a-d, the dashed vertical lines mark the positions of the edges of the roof. Figure 11 clearly shows that the increasing building width W leads to a decrease of the wind speed and to an increase of the overpressure upstream of the roof. The increasing building width W also leads to a decrease (more negative value) of the underpressure directly downstream of the roof (see Fig. 11d). As a result, the flow through the roof is enhanced and the absolute value of the underpressure is increased.

Although point E appears to be the optimal position for a ventilation exhaust, it is worthwhile to look at the pressure coefficient distribution on the entire lower part of the roof. Figure 12 provides additional information on possible locations of ventilation exhausts. The dashed rectangles in Figure 12 indicate the projected surface areas with low C_P values. The regions with low C_P values are defined as the surface areas with $C_P < -0.8$ for W = 20 m, and $C_P < -1.1$ for W = 40 to W = 160 m. The relative surface area ($A_{CP<-0.8}/A$; $A_{CP<-1.1}/A$) with low pressures increases with increasing W; for W = 40 m 8.2% of the building area has a C_P value lower than -1.1, while for W = 160 m this percentage is 13.4%. The area with low C_P values for W = 20 m is 11.8%, but please note that the limit for this building width was set to $C_P < -0.8$ due to the lower C_P values, as presented in Figure 8. For W = 20 m, there is not any point in which the underpressure decreases below -1.1. The depth (streamwise direction) of the low-pressure areas varies only slightly with W: from 29.3% of the entire building depth (= 20 m) for W = 40 m to 33.3% for W = 160 m. The width of the low-pressure areas shows larger variations, ranging from 28% to 40.1% for W = 40 m and W = 160 m, respectively. For W = 20 m, the depth of the low-pressure area is 37.3%, whereas the width is 31.8%. Therefore, the differences between the low-pressure areas can be largely attributed to the increase in width (lateral direction) of the low-pressure area with increasing W.

5. Discussion

The evaluation of the aerodynamic performance of the roof has been mainly conducted based on the value of the pressure coefficient at point E. However, the simulations showed that large pressure gradients are present in the roof contraction. Point E was chosen because of its position in the centre of the contraction, and because it corresponded to the location of the point measurement in the wind tunnel model. A future study on the aerodynamic performance of the roof will include modelling the exhaust flow rate through the vertical channel, and that enters the roof contraction due to the generated underpressure.

The present study only evaluated the influence of building width for wind direction perpendicular to the wide facade of the building. Further research will focus on oblique wind directions, and on the influence of building height and of the approach-flow wind conditions on the performance of the roof.

6. Summary and conclusions

This paper has presented a numerical analysis with CFD to investigate the influence of building width on the performance of a venturi-shaped roof for natural ventilation. In previous studies, the influence of the roof configuration on its performance was analysed in detail, however these studies were all performed for a fixed building geometry, i.e. a tower building with a floor plan of 20 x 20 m² and a height of 50 m. It was important to analyse the performance of the roof for different building widths. Therefore, the present paper has presented CFD simulations for building (and roof) widths of 20, 40, 80, 120 and 160 m. The 3D steady Reynolds-averaged Navier-Stokes (RANS) approach with the Renormalization Group (RNG) k-ε model were used. The simulations were based on grid-sensitivity analysis and on validation by comparison with wind tunnel experiments. The simulations showed that the aerodynamic performance of the roof in terms of the underpressure in the contraction improved with about 31% when the building width is increased from 20 m to 40 m, while further increasing the building width only provided small additional improvements. The increased performance with increasing building width is attributed to the larger overpressure upstream of the building and to the larger underpressure and larger size (height) of the wake behind the building. The area of the roof which has the potential to contain a ventilation exhaust slightly increases with increasing W; for W = 40 m 9.2% of the roof surface area of the building has a C_P value lower than -1.1, while for W = 160 m 13.2% of the area has a C_P value which is lower than -1.1.

References

Blocken, B., Carmeliet, J., Stathopoulos, T., 2007a. CFD evaluation of the wind speed conditions in passages between buildings – effect of wall-function roughness modifications on the atmospheric boundary layer flow. J. Wind Eng. Ind. Aerodyn. 95(9-11), 941-962.

Blocken, B., Stathopoulos, T., Carmeliet, J., 2007b. CFD simulation of the atmospheric boundary layer: wall function problems. Atmos. Environ. 41(2), 238-252.

Blocken, B., Stathopoulos, T., Carmeliet, J., 2008a. Wind environmental conditions in passages between two long narrow perpendicular buildings. J. Aerospace Eng.–ASCE 21(4), 280-287.

Blocken, B., Stathopoulos, T., Carmeliet, J., 2008b. A numerical study on the existence of the Venturi-effect in passages between perpendicular buildings. J. Eng. Mech.-ASCE 134(12), 1021-1028.

Blocken, B., van Hooff, T., Aanen, L., Bronsema, B., 2011. Computational analysis of the performance of a venturi-shaped roof for natural ventilation: venturi-effect versus wind-blocking effect. Comput. Fluids 48(1), 202-213.

Bronsema, B., 2010. Earth, Wind & Fire – Air-conditioning powered by nature. 10th REHVA World Congress CLIMA 2010, 9-12 May, Antalya, Turkey.

Cebeci, T., Bradshaw, P., 1977. Momentum transfer in boundary layers, Hemisphere Publishing Corporation.

Chen, Q., 2009. Ventilation performance prediction for buildings: A method overview and recent applications. Build. Environ. 44(4), 848-858.

Evola, G., Popov, V., 2006. Computational analysis of wind driven natural ventilation in buildings. Energy Build 38(5), 491-501.

Fluent Inc. Fluent 6.3. User's Guide. Fluent Inc., Lebanon; 2006.

Franke, J., Hirsch, C., Jensen, A.G., Krüs, H.W., Schatzmann, M., Westbury, P.S., Miles, S.D., Wisse, J.A., Wright, N.G., 2004. Recommendations on the use of CFD in wind engineering. In: van Beeck, J.P.A.J. (Ed.), COST Action C14, Impact of Wind and Storm on City Life Built Environment, Proceedings of the International Conference on Urban Wind Engineering and Building Aerodynamics. Von Karman Institute, Sint-Genesius-Rode, Belgium, 5–7 May 2004.

Franke, J., Hellsten, A., Schlünzen, H., Carissimo, B. (Eds.). 2007. Best practice guideline for the CFD simulation of flows in the urban environment. COST Office Brussels.

Hunt, G.R., Linden, P.F., 1999. The fluid mechanics of natural ventilation - displacement ventilation by buoyancy-driven flows assisted by wind. Build. Environ. 34(6), 707-720.
Larsen, T.S., Heiselberg, P., 2008. Single-sided natural ventilation driven by wind pressure and temperature difference. Energy Build. 40(6), 1031-1040.
Launder, B.E., Spalding, D.B., 1974. The numerical computation of turbulent flows. Comput. Method Appl. M 3, 269-289.
Li ,Y.G., Delsante, A., 2001. Natural ventilation induced by combined wind and thermal forces. Build. Environ. 36(1), 59-71.
Linden, P.F., 1999. The fluid mechanics of natural ventilation. Annu. Rev. Fluid Mech. 31, 201-238.
Ramponi, R., Blocken, B., 2012. CFD simulation of cross-ventilation for a generic isolated building: Impact of computational parameters. Build. Environ. 53: 34-48..
Tominaga, Y., Mochida, A., Yoshie, R., Kataoka, H., Nozu, T., Yoshikawa, M., Shirasawa, T., 2008. AIJ guidelines for practical applications of CFD to pedestrian wind environment around buildings. J. Wind Eng. Ind. Aerodyn. 96(10-11), 1749-1761.
van Hooff, T., Blocken, B., Aanen, L., Bronsema, B., 2011. A venturi-shaped roof for wind-induced natural ventilation of buildings: wind tunnel and CFD evaluation of different design configurations. Build. Environ. 46(9), 1797-1807.
van Hooff, T., Blocken, B., 2010. Coupled urban wind flow and indoor natural ventilation modelling on a high-resolution grid: A case study for the Amsterdam ArenA stadium. Environ. Modell. Softw. 25(1), 51-65.
Yakhot, V., Orszag, S.A., Thangam, S., Gatski, T.B., Speziale, C.G., 1992. Development of turbulence models for shear flows by a double expansion technique. Phys. Fluids A4, 1510-1520.

FIGURES

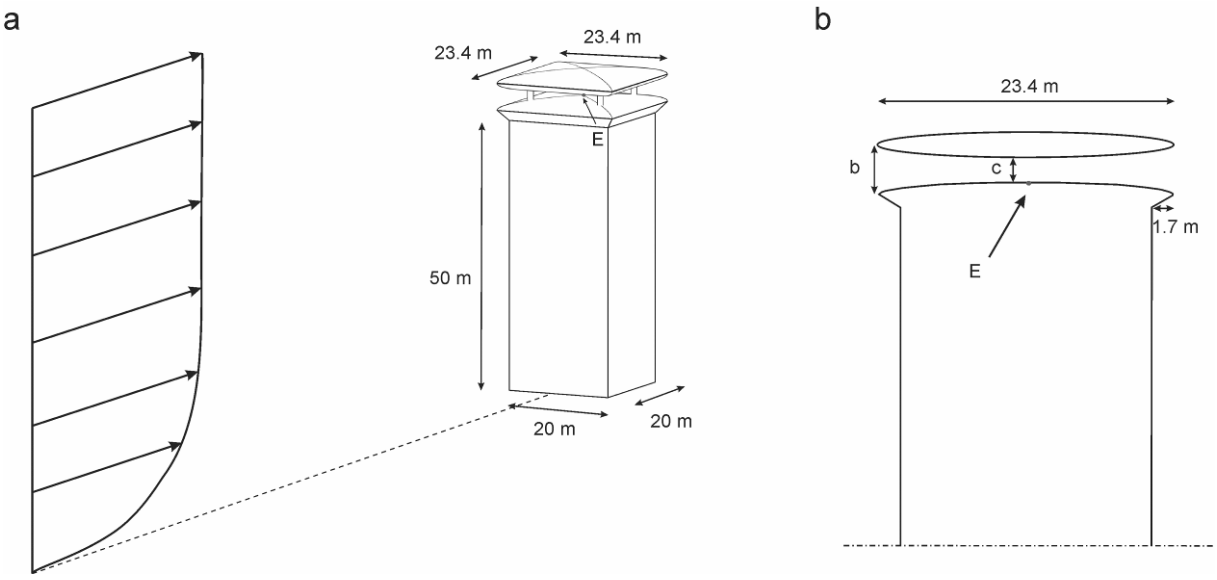

Fig. 1: (a) Perspective view of the basic (20 x 20 m²) building geometry with venturi-shaped roof (Ventec roof) and main dimensions. (b) Vertical cross-section of the building and Ventec roof with indication of position E where the surface pressure is evaluated. In the present study: b = 6 m and c = 2 m.

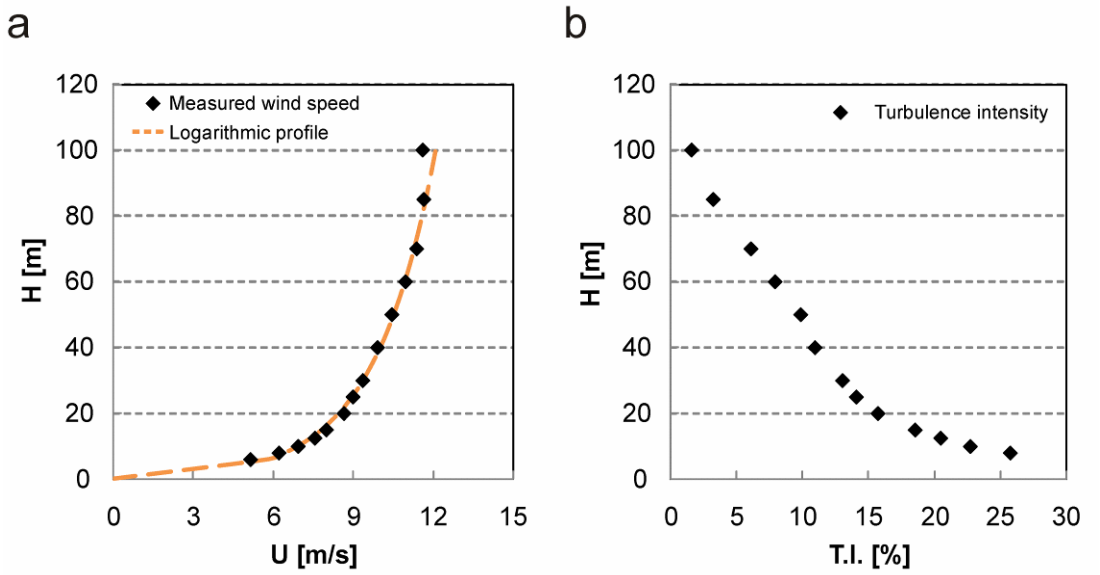

Fig. 2: (a) Measured approach-flow mean wind speed profile along a vertical line at the upstream edge of the turntable (full-scale dimensions; log law profile with u* = 0.956 m/s and y_0 = 0.5 m). (b) Measured turbulence intensity T.I. along the same vertical line (full-scale dimensions).

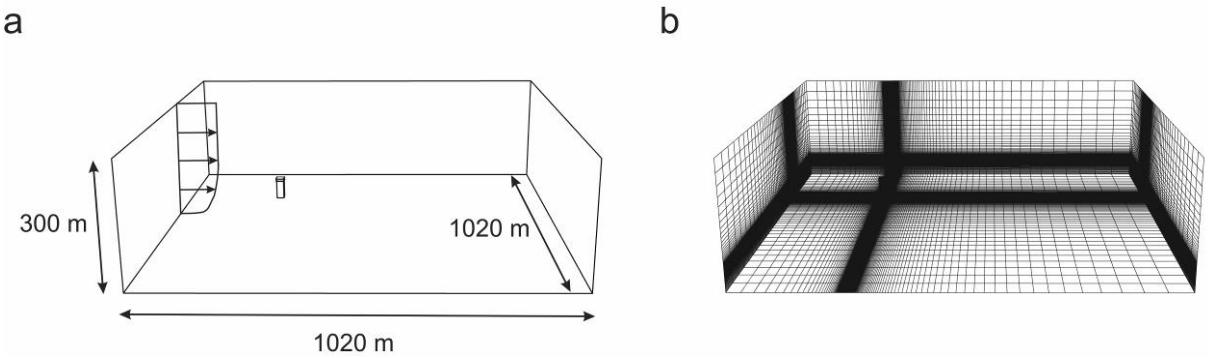

Fig. 3: (a) View of the building in its computational domain (full-scale dimensions). (b) Perspective view of the computational grid at some of the domain surfaces. Total number of cells is 2,375,016.

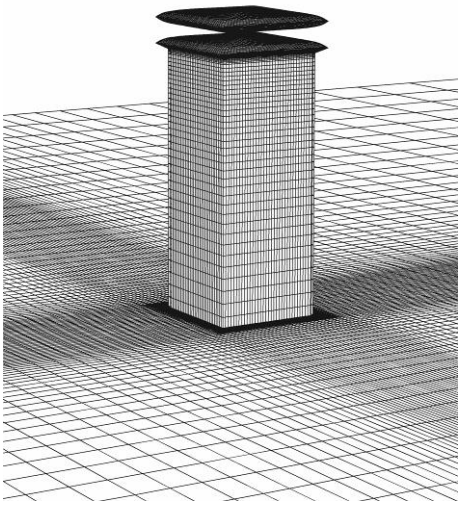

Fig.4: Perspective view of computational grid on the building and ground surfaces. Total number of cells is 2,375,016.

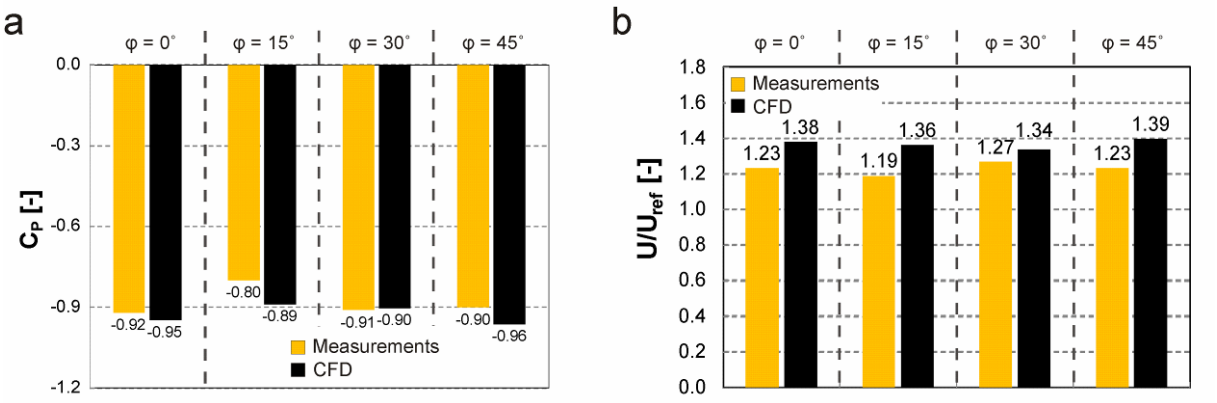

Fig. 5: Comparison of wind tunnel measurements and CFD simulation results for four wind directions (φ = 0°, φ = 15°, φ = 30°, φ = 45°). (a) Pressure coefficient C_P at point E. (b) Dimensionless velocity magnitude U/U_{ref} at mid-height in the centre of the roof contraction. U_{ref} is the approach-flow wind speed at building height (50 m).

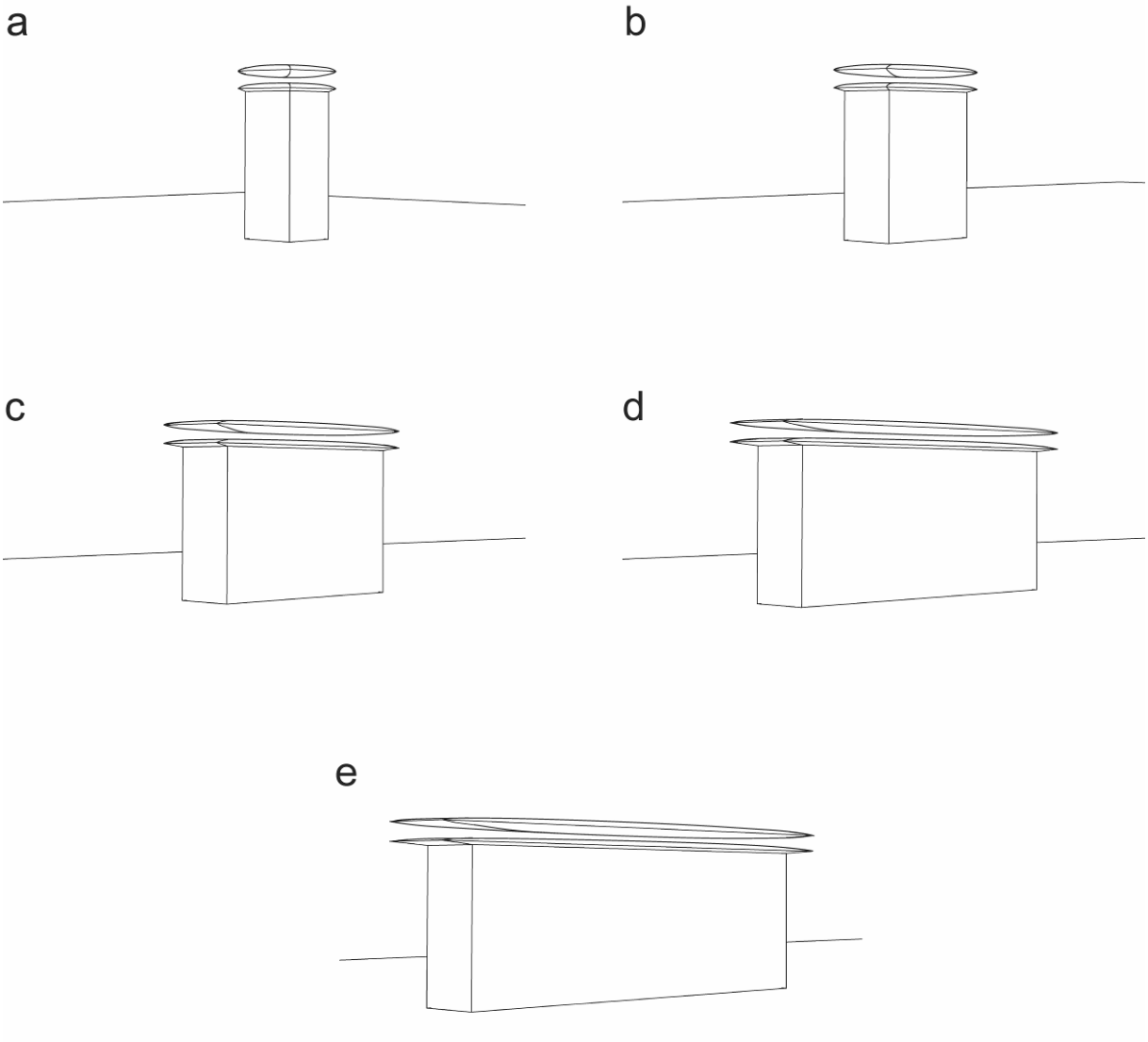

Fig. 6: Five different building and roof geometries: (a) W = 20 m; (b) W = 40 m; (c) W = 80 m; (d) W = 120 m; (e) W = 160 m. The configurations are tested for wind perpendicular to the wide facade.

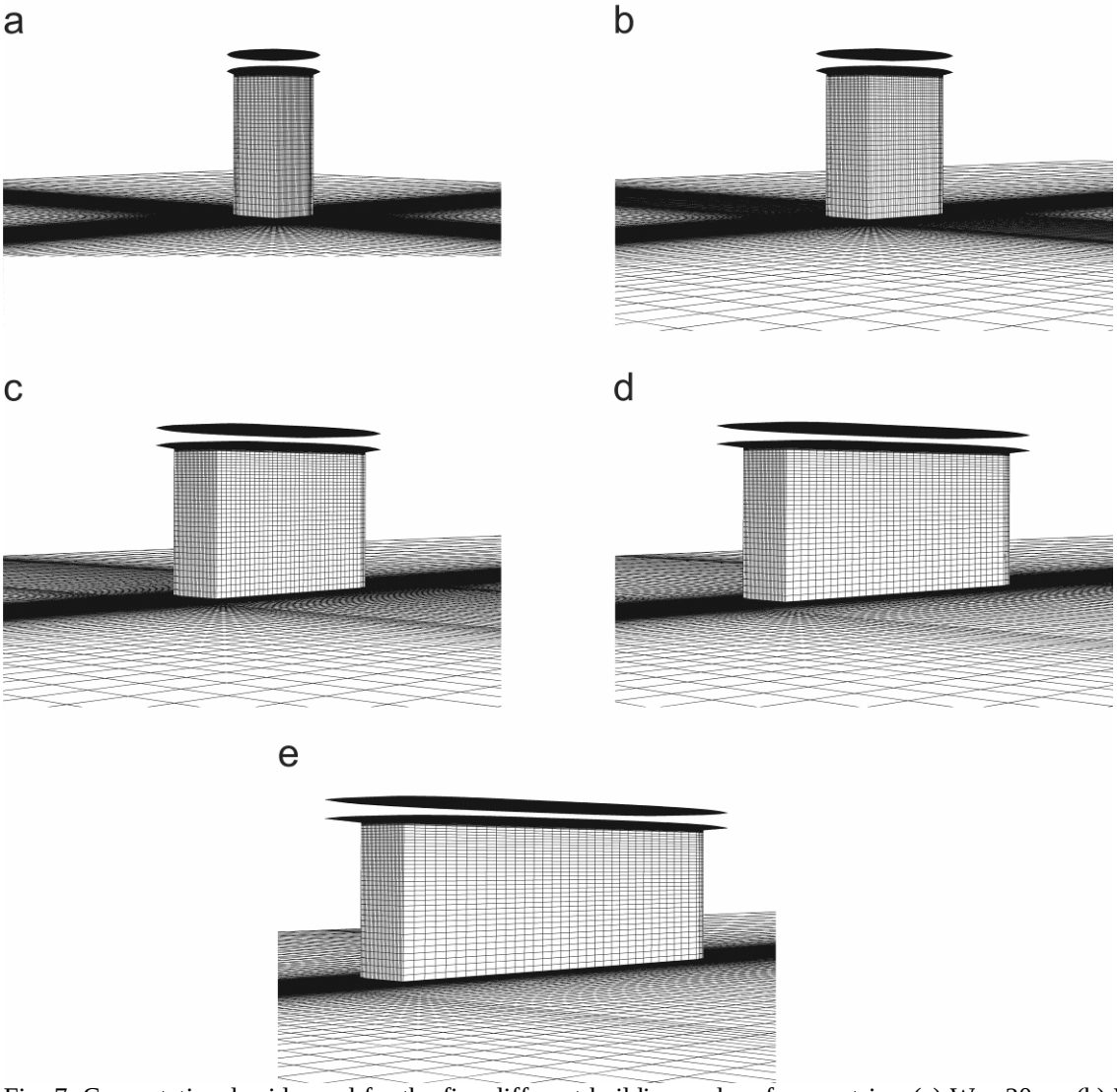

Fig. 7: Computational grids used for the five different building and roof geometries. (a) W = 20 m; (b) W = 40 m; (c) W = 80 m; (d) W = 120 m; (e) W = 160 m. All grids consist of 2,375,016 cells.

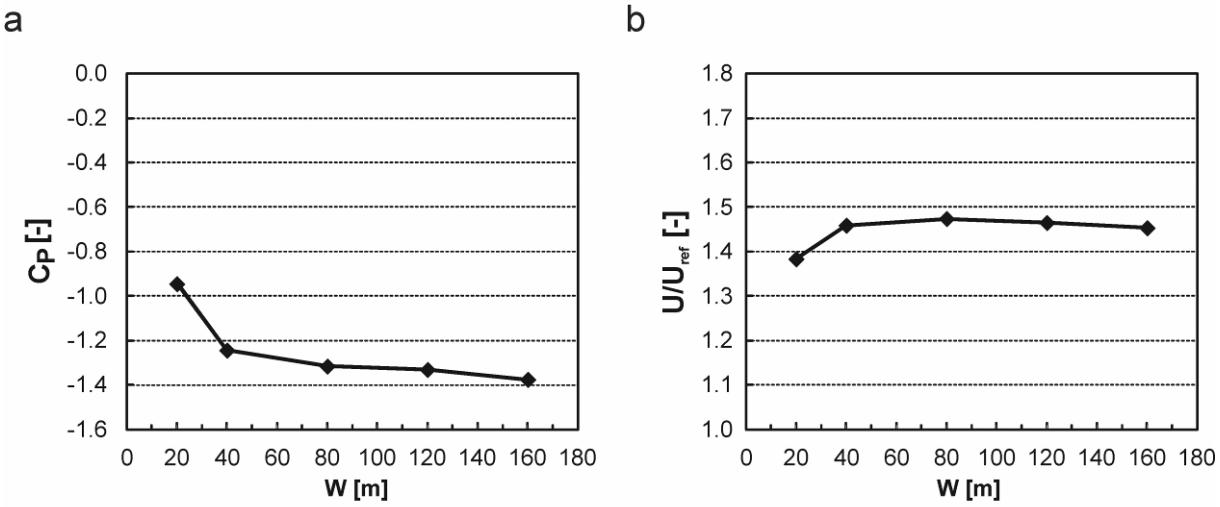

Fig. 8: (a) Wind pressure coefficient C_P at point E as a function of building width, for wind perpendicular to the wide facade. (b) Dimensionless velocity magnitude (U/U_{ref}) at mid-height in the centre of the roof contraction as a function of building width, for wind perpendicular to the wide facade. U_{ref} is the approach-flow wind speed at building height (50 m).

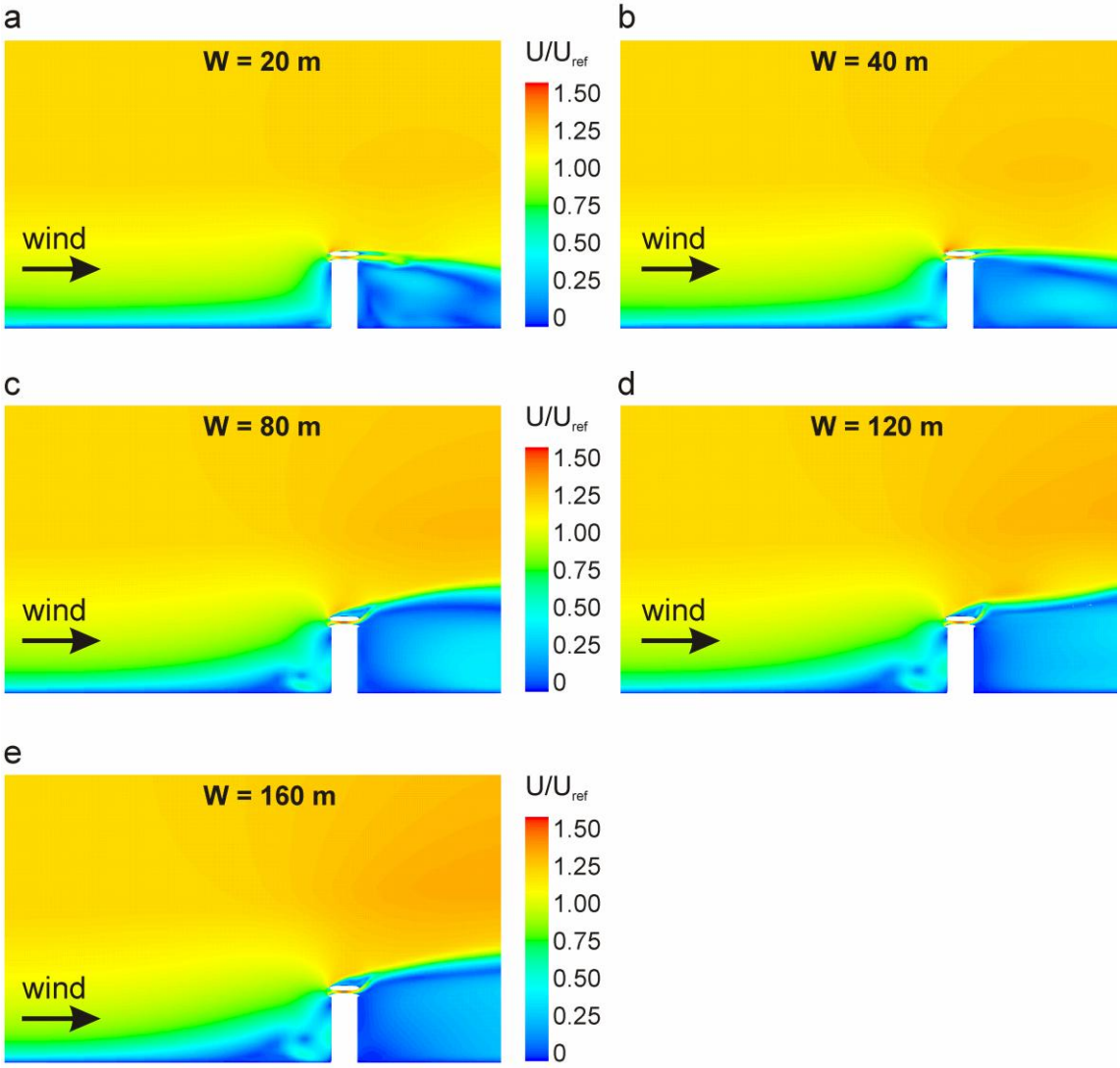

Fig. 9: Contours of dimensionless velocity magnitude (U/U_{ref}) in the vertical centre plane through the building, for wind perpendicular to the wide facade. (a) W = 20 m; (b) W = 40 m; (c) W = 80 m; (d) W = 120 m; (e) W = 160 m. U_{ref} is the approach-flow wind speed at building height (50 m).

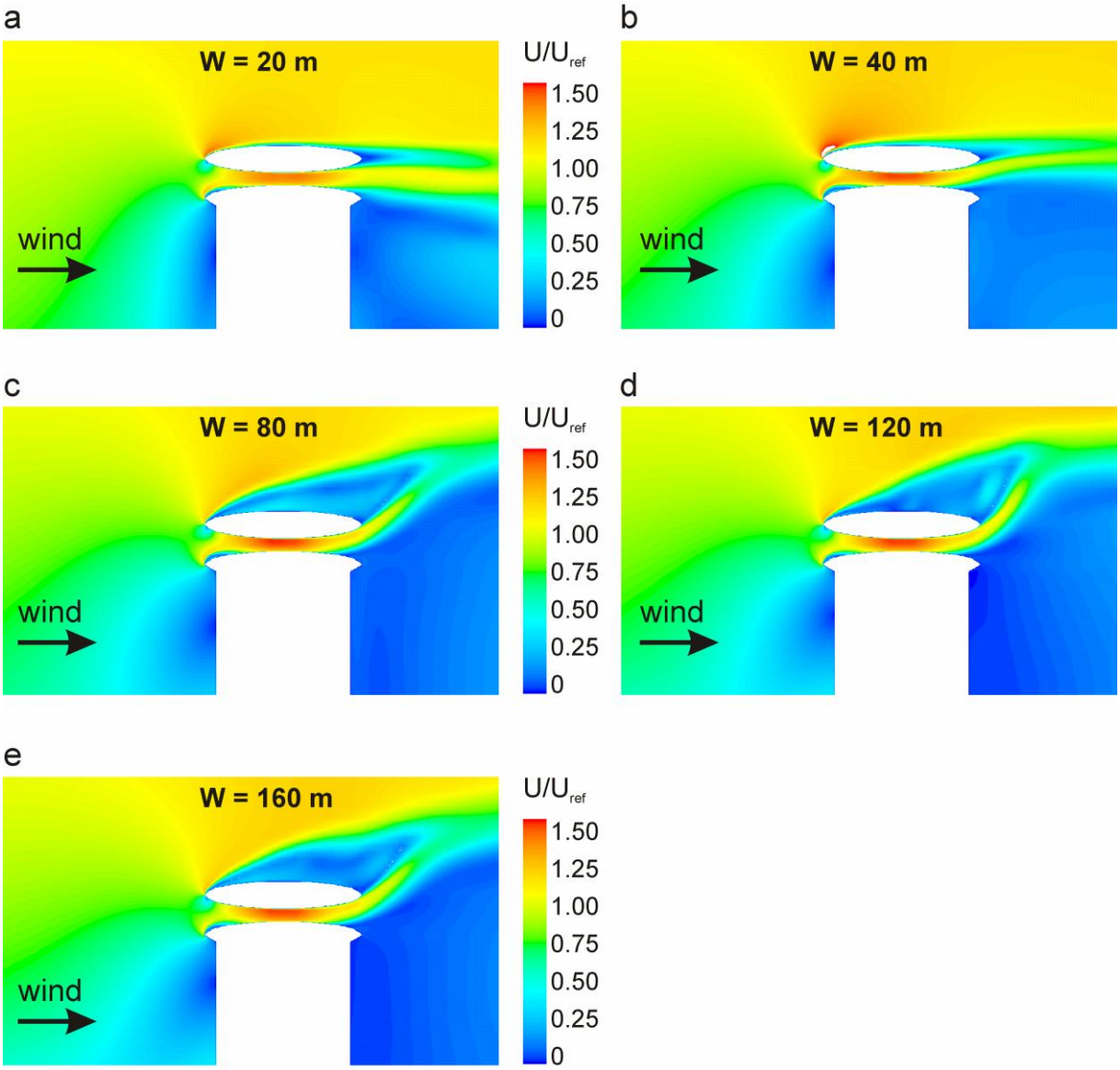

Fig. 10: Enlarged view of contours of dimensionless velocity magnitude (U/U_{ref}) in the vertical centre plane through the building, for wind perpendicular to the wide facade. (a) W = 20 m; (b) W = 40 m; (c) W = 80 m; (d) W = 120 m; (e) W = 160 m. U_{ref} is the approach-flow wind speed at building height (50 m).

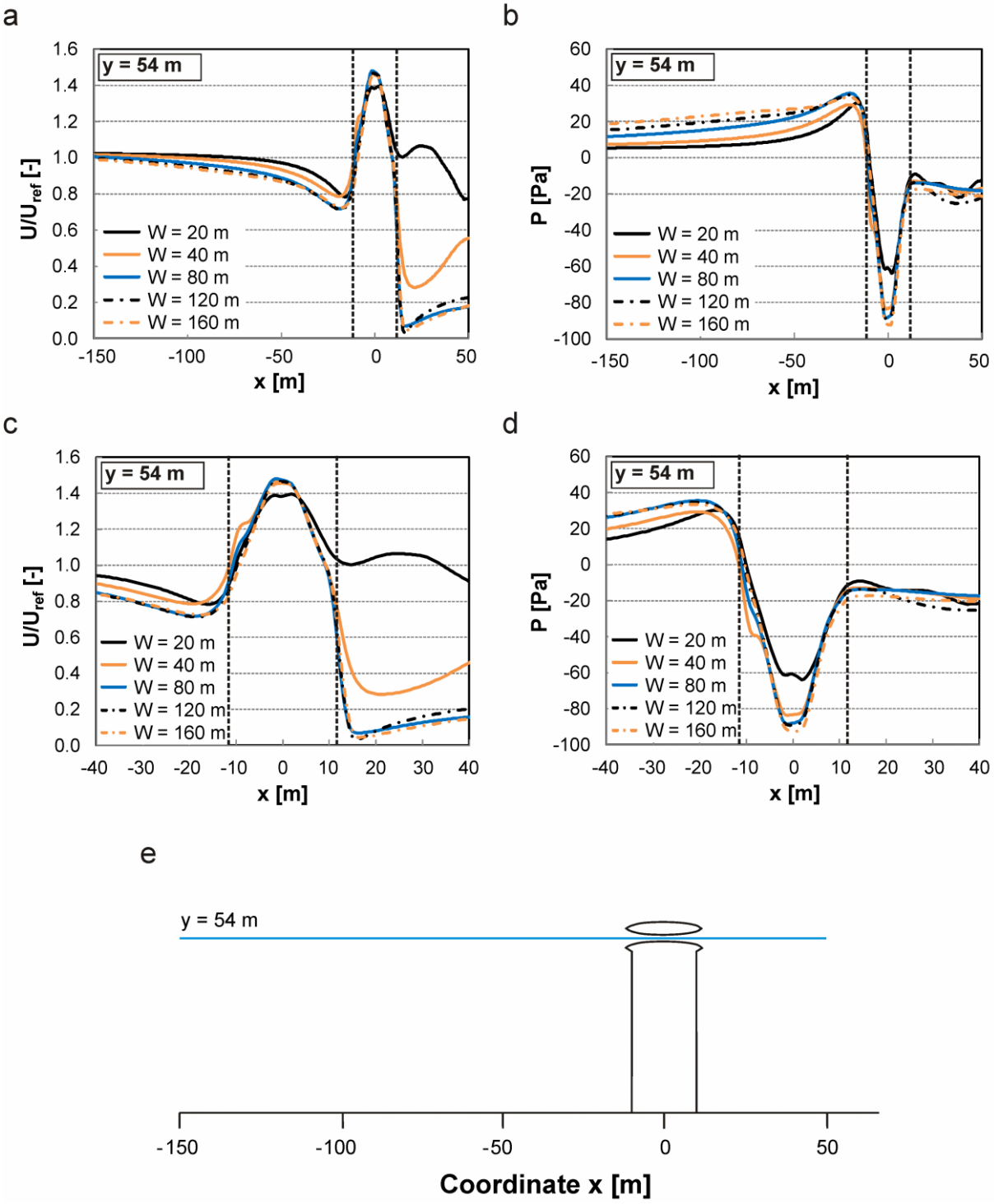

Fig. 11: (a,c) Profiles of dimensionless velocity magnitude (U/U_{ref}) upstream and downstream of the building as a function of building width W, along the plotting line indicated in figure (e). (b,d) Static pressure profiles along the same line. The dashed vertical lines mark the positions of the edges of the roof. (e) Location of the plotting line in the vertical centre plane through the building.

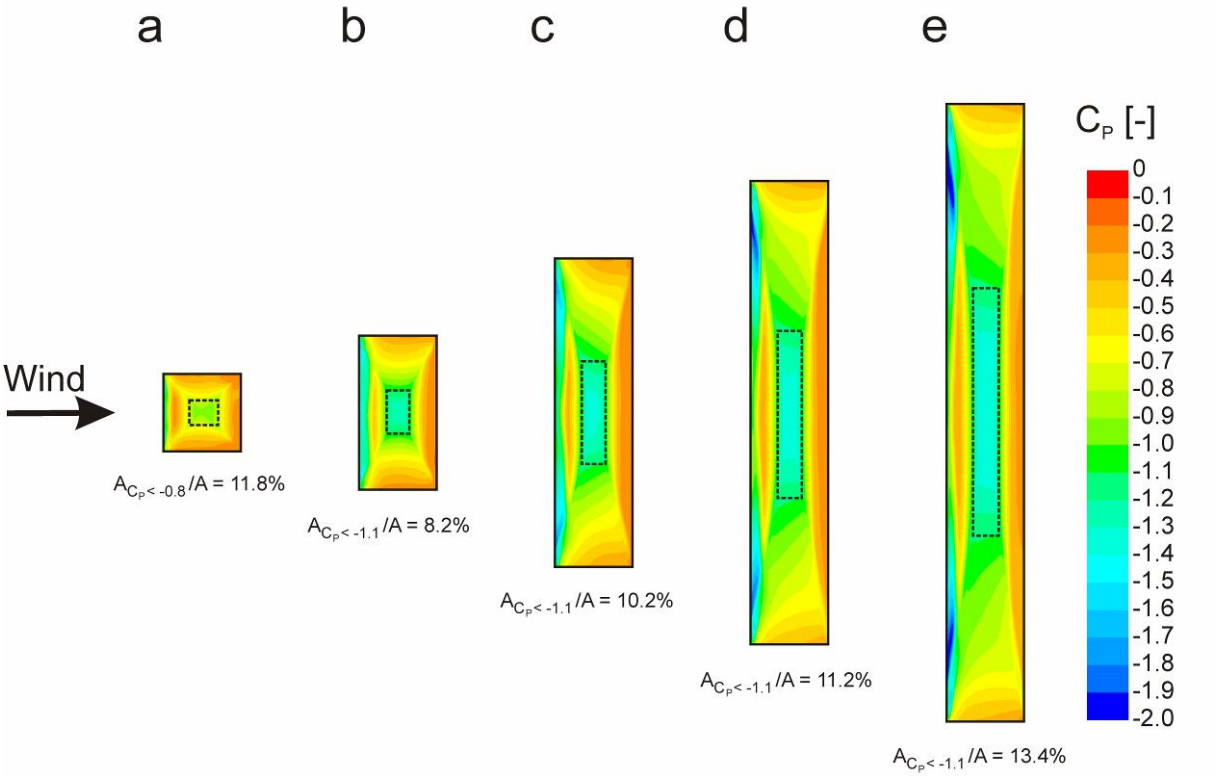

Fig. 12: Contours of the pressure coefficient C_P at the surface of the lower part of the roof. (a) W = 20 m; (b) W = 40 m; (c) W = 80 m; (d) W = 120 m; (e) W = 160 m.